# In-situ analysis of particles in contact under ambient conditions

Technische und Makromolekulare Chemie

Universität Paderborn

Zur Erlangung des Grades

Doktor der Naturwissenschaften

Dissertation vorgelegt von

Boray Barış Torun, M.Sc.

Genehmigte Fassung

Gutachter: Prof. Dr.-Ing. Guido Grundmeier

Prof. Dr.-Ing. Hans-Joachim Schmid

*The principle of science, the definition almost, is the following: The test of all knowledge is experiment. Experiment is the sole judge of scientific 'truth'.*

Richard Feynman [1]

## Acknowledgements

A thesis, however small it might be, is never the work of just but one individual. Although there were many more involved than I could mention at this point without making this chapter a thesis of its own, I still would like to thank a few individuals who contributed in a profound way.

First of all, I would like to thank Prof. Dr. Grundmeier for his supervising, guidance and many interesting discussions we had. I greatly thank him for entrusting me with this exciting and challenging project as well as for facilitating my research in any possible way.

Special thanks go also out to Prof. Dr. Thomas Kühne (University of Paderborn) for his profound contribution to the evaluation of the IR data and Prof. Dr. Hans-Joachim Schmid for the fruitful collaboration within the DFG priority project "Partikel im Kontakt" as well as for agreeing to be the second referee of this thesis.

In addition, I want to thank Dr. Ignacio Giner for his enormous help with many of the experiments presented in this study and the great effort he put into the revision of this manuscript.

I also want to thank Dr. Berkem Özkaya for the many times we talked, had fun together in the lab or simply tried to solve a *general* problem. However, I mostly thank him for becoming something found only very rarely: a true friend.

Moreover, I also thank my parents Nilgün Torun and Yenal Torun. If not for them and their constant love and support, I would have not made it to the point I am now. They supported me throughout the years enabling my studies and encouraging me to improve myself.

Last but not least I want to thank Sabrina Müller for brightening me up when I was frustrated from experiments gone wrong and for being my steady anchor during all this years of study, labor and challenge. If not for her I would have never been able to write this thesis.

## Table of content

# 1. Abstract

During the past decade nanoparticles attracted a great deal of attention and found many applications in various fields ranging from pigments and antibacterial agents to highly effective catalysts. In this context, the handling and processing of nanoparticle powders play an important role. In contrast to macroscopic particles, nanoparticle flow properties are manly governed by the particle-particle interactions. The forces determining these interactions strongly vary not only with the material properties but also with surface chemical composition as well as the environmental conditions. Hence, a fundamental understanding of the processes and forces involved plays a key role for the prediction of nanoparticle powder behavior.

In the presented study two main questions are in focus:

1. What is the role of water adsorbate layers in nanoparticle ensembles and how does the complex water structure impact the inter-particle forces as a function of humidity?
2. What influence does the surface chemistry of nanoparticles have on the inter-particle forces and can these interactions be altered via chemical modification?

In this work, the water adsorption and capillary bridge formation within defined layers of $SiO_2$ and $TiO_2$ nanoparticles were studied by means of a novel in-situ analytical setup allowing for combined quartz crystal microbalance measurements with dissipation analysis (QCM-D) and Fourier transform infrared reflection absorption spectroscopy (FT-IRRAS). On the one hand, the QCM-D gave insights on both mass change ($\Delta f$) and changes in the contact mechanics, indicated by dissipation changes ($\Delta\Gamma$), whereas on the other hand FT-IRRAS allowed for the characterization of the adsorbed water structure. Employing peak deconvolution to the OH-signal, “ice-like” and “liquid-like” water structures could be clearly identified. Moreover, the presence of different water species was successfully attributed to changes in the particle layer mechanics.

In addition to the combined QCM-D / FT-IRRAS experiments, a new experimental setup has been established to perform AFM based force spectroscopy under controlled atmospheric conditions. Mentioned method was employed for a detailed in-situ study of the complex interplay between UV-light, humidity and surface adsorbate species towards the surface chemistry and contact forces of $TiO_2$ nanoparticles

# 2. Introduction

## 2.1. Motivation

In the past few years, nanoparticles have attracted a great deal of interest in science as well as in industrial application. However, the actual history of nanosized materials dates back hundreds of years. Although it is safe to assume that during this period, mankind was not aware of the materials special nature. It was found that artisans used metallic nanoparticles to color the glazing of pottery [2]. Using empirical developed methods, they were able to prepare noble metal nanoparticles embedded in an inorganic glass like matrix.

As a result of the lack of appropriate analytical technique to study such fine materials, it was not until the early 1970's that the first fundamental studies of nanoparticles could be performed. As by definition, particles in the range of $1 \cdot 10^{-9}$ m to $1 \cdot 10^{-7}$ m are named nanosized. However, the definition is often extended to particles with a size up to $5 \cdot 10^{-7}$ m. The reason for the high popularity of these particles in various filed originates from their extraordinary properties when compared to the corresponding bulk materials. For example, gold nanoparticle suspensions exhibit different colors as a function or particle size (Figure 1) [3,4], morphology (nanospheres, nanorods) [5,6] or complex structure for more sophisticated core shell particles [7-9].

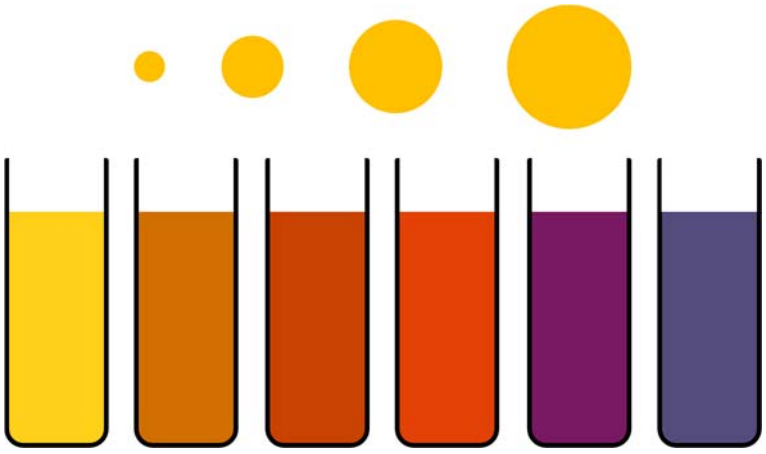

*Figure 1: Schematic of the influence of gold nanoparticle size on corresponding suspension color.*

In addition to the often found unexpected light absorption behavior, other physical properties such as the melting point, conductivity or mechanical properties, can deviate drastically from that of the corresponding bulk material. In general, the special characteristics of these small particles stem from their extraordinary high surface to volume ratio in contrast to macroscopic particles. Although, equation (2.1) shows that for a particle with spherical geometry, the actual particle surface (A) to volume (V) ratio scales linearly with the radius (r), it has to kept in mind that the number of atoms on the surface versus the number of atoms located in the bulk does not.

$$\frac{A_{sphere}}{V_{sphere}} = \frac{4\pi r^2}{\frac{4}{3}\pi r^3} = \frac{3}{r} \tag{2.1}$$

The reason for that is the discrete nature of the nanoparticle building blocks as depicted in Figure 2.

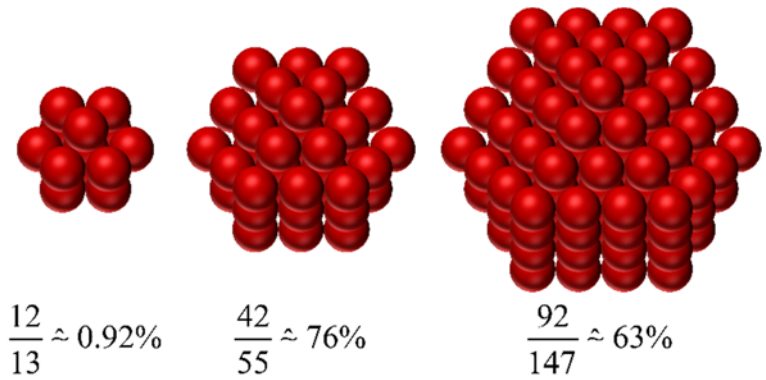


*Figure 2: Evolution of surface-to-volume ratio with the fraction of surface atoms given in % for particles consisting of an increasing number of atoms.*

Since the first systematic studies in the 70's, investigations on nanoparticle systems have come a long way resulting in a much better understanding of these materials. As a consequence, nanoparticles found thousands of applications in industrial products. In this context silver nanoparticles are a very prominent example for their antibacterial [10-12], antifungal [13] and antiviral [14] properties. Hence, these particles found a wide array of applications ranging from the incorporation in common textile materials for the prevention of unwanted odors (preventing bacteria buildup) [15], over to the addition of silver nanoparticles in polymer materials used for the production of hospital furniture helping against the spreading of pathogenic organisms [16]. However, the application of nanoparticles in general is by far not limited to health related topics. In the field of energy conversion, $TiO_2$ nanoparticles have been found to act as potent dyes improving the overall efficiency of light collecting solar panels [17-20]. Moreover, in chemical industry, nanoparticles are being applied as powerful and easy recoverable catalysts [21-23] for chemical synthesis.

In the context of the multifarious fields of application, the handling and processing of nanoparticle material, and especially its flow properties, play a key role. However, in contrast to ensembles of larger particles, the behavior of nanoparticle powders mostly depends on the inter-particle forces which again are mainly governed by the surface chemical composition and the surface morphology. In addition, environmental factors like the presence of humidity can also greatly affect the inter-particle forces, altering the powders behavior.

## 2.2. Structure of this thesis

Since the complex interplay between environmental factors (humidity), surface chemistry and particle ensemble behavior is of outmost interest for many applications, two main questions were in focus within the scope of this thesis:

1. What is the role of water adsorbate layers in nanoparticle ensembles and how does the complex water structure impact the inter-particle forces as a function of humidity?
2. What influence does the surface chemistry of nanoparticles have on the inter-particle forces and can these interactions be altered via chemical modification?

For addressing these questions, two novel experimental approaches facilitating detailed investigations on $SiO_2$ and $TiO_2$ nanoparticles under ambient conditions were developed which represent the core of this thesis:

1. An in-situ analytical setup allowing for combined measurement of quartz crystal microbalance with dissipation analysis (QCM-D) and Fourier transform infrared reflection absorption spectroscopy (FT-IRRAS).
2. An AFM based force spectroscopy experiment under controlled atmospheric conditions allowing for the direct probing of particle contact forces under UV-light irradiation.

Details regarding these new setups and corresponding results are presented in chapter 4 (combined QCM-D / FT-IR) and chapter 5 (AFM based force spectroscopy). All details regarding the sample preparation, substrate pretreatments necessary for these experiments and parameters of the analytical devices used are consolidated in chapter 3.

Additionally, in order to provide the reader with a general overview, the subsequent sections will discuss the preparation and structure of nanoparticles (chapter 2.3), surface chemistry and interfacial processes on $SiO_2$ and $TiO_2$ surfaces (chapter 2.4) and two common models for particle contact forces (chapter 2.5) in great detail. Moreover, chapter 2.6 will provide a brief summary of the fundamentals behind the main analytical methods and discuss them in the context of investigations on particle systems.

## 2.3. Oxide nanoparticles

### 2.3.1. Preparation of oxide nanoparticles

As mentioned in section 2.1, the first nanoparticles employed by mankind were prepared by empirically derived methods without an actual knowledge of the processes leading to the formation of nanoscale objects. Today, mostly two distinct approaches for the preparation of nanoscale particles are discussed, namely the bottom-up and the top-down approach (Figure 3). The latter covers all processes where larger aggregates are continuously broken up in to smaller fraction whereas the first approach encompasses all methods where particles are "grown" starting with small nuclei.

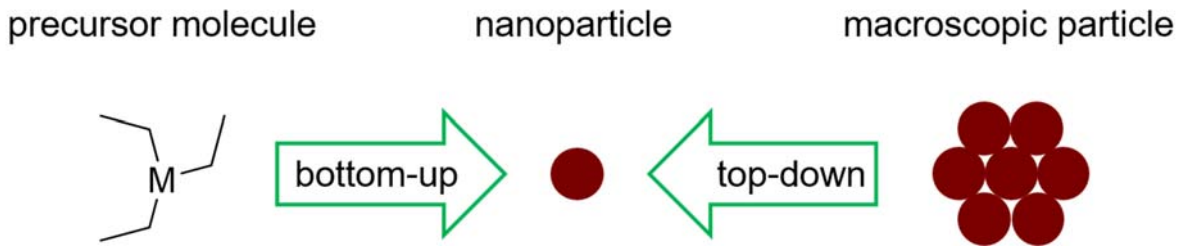


*Figure 3: Schematic of the bottom-up and top-down approach. The structure on the left is just a placeholder for any arbitrary precursor molecule.*

In the case of a top-down approach, macroscopic material is typically grinded until the desired particle size is achieved. Although this method is commonly applied in industrial applications, it bears numerous disadvantages. In particular, particles prepared by this method are very often contaminated with species originating from the machinery needed for the grinding. Moreover, due to the nature of the process, an enormous amount of energy is being dissipated in the material often leading to unwanted chemical reactions and degradation of the powder. In addition, the products often feature a very broad size distribution and only very poorly defined particle morphologies. However, grinding processes are easily scalable and rather cheap in terms of cost efficiency. Therefore, they are widely applied when the surface chemistry as well as the morphology of the particles play an inferior role. Typical examples for this sort of requirements are pigment materials like $TiO_2$ commonly used for paints.

In recent time, various methods have been developed using the bottom-up approach. Typical examples for this are the preparation via solvent based sol-gel routes or occasionally solvent free flame pyrolysis. Both methods are commonly applied for the preparation of metal oxide particles and both utilize the subsequent growth of nanoparticles from adequate precursor materials [24-29].

For the preparation via sol-gel route, a precursor is dissolved in an organic solvent. Typically, a surfactant which facilitates the formation of small active micelles and stabilizes the particle nucleation is added to the mixture. In a second step, a reactive species (most often water) is added slowly starting a crosslinking reaction of the precursor molecules. Once the reaction is finished the particles can be extracted from the liquid phase. Particle size can be influenced by means of controlling the reaction speed and time. In general, slower crosslinking reactions (low temperature, small amount of crosslinking agent) lead to larger particles. A very prominent example for this particular method are the Stöber silica particles [28] depicted in Figure 4-D.

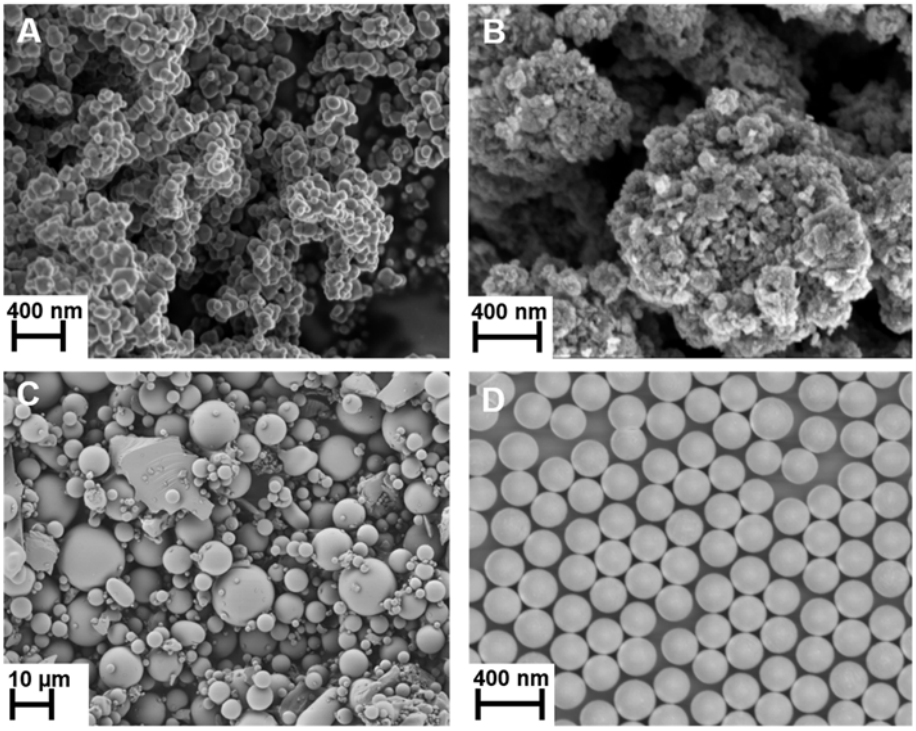


*Figure 4: FE-SEM images of various particles. The larger particles in (B) are derived from sol-gel based primary particles in (A) via a sintering process. Glass particles prepared via casting of hot glass melt in water (C). $SiO_2$ nanoparticle prepared via Stöber silica route from sol-gel synthesis.*

In the case of particle preparation via flame pyrolysis reaction, typically a gas carrying the desired metal element precursor is burned in a torch resulting in the full oxidation and

immediate growth of particles in the hot flame. The generated, particle containing smoke is subsequently collected. Following this approach, $TiO_2$ particles are prepared by the combustion of titanium (IV) isopropoxide (TTIP). In order to avoid any contamination with carbon based species, an oxyhydrogen based torch is preferred over a conventional fossil fuel based flame. During the last decade this rather simple concept has been elaborated to the point where so called hot-wall reactors allow for much more control of the growing and sintering process after the actual combustion of the precursor material [30,31]. Thereby, parameters like particle size, degree of crystallinity and crystal phase can be influenced during the process to yield particles with desired properties.

### 2.3.2. Structure of oxide nanoparticles

As mentioned in section 2.1, the physical structure (e.g. morphology, shape, size) of nanoparticles plays a key role for their properties. Moreover, the chemical structure is of high importance for many applications. Typically, physical properties mostly depend on the preparation method and the corresponding conditions during the particle synthesis. Hence they cannot be tuned afterwards without a significant amount of effort. In contrast to that, the chemical structure of the particles, despite also being greatly affected by the conditions during synthesis, can often still be tuned by various methods after the particles have been synthetized.

Focusing on the physical structure first, it is widely accepted that the amount of control over the particle morphology is typically found to be much greater using a bottom-up strategy rather than a top-down approach. The reason for that can be identified in the highly complex nature of the processes employed for breaking up larger particles into nanoscale objects. Typical examples for these processes are the milling of oxide materials. Since the resulting material often features a very broad size distribution, these processes typically employ additional steps like sieving methods for the preparation particles with smaller dispersity. However, the shape of the resulting particles is often still poorly defined and very heterogeneous. Nevertheless, these processes are still widely employed in many industrial applications despite their obvious disadvantages with regard to the amount of control over the resulting particle structure. Hence, the development of more elaborate top-down approaches resulting in particles with highly defined properties has attracted much interest in the past few years. Two examples for the preparation of nanoparticles with low dispersity via top-down

strategy are given by Yang et al. (laser assisted method for the preparation of colloidal PbS quantum dots) [32] and Wang et al. (emulsification of metal melts under shear stress) [33]. In both cases prepared nanoparticles featured a spherical geometry similar to that for particles formed via classical sol-gel based synthesis. In fact, in the case of particles with defined morphology, nanospheres represent the most common and experimentally easiest accessible type. However, more sophisticated preparation strategies for core shell nanoparticles [34,35], nano cubes [36,37] and nanowires [38] are also reported in the literature.

In addition to the vast number of different nanoparticle morphologies experimentally accessible, the chemical structure can also be determined using different starting materials. From a chemical perspective, most nanoparticles commonly found can be assigned to one of four groups:

1. Metal nanoparticles like Au, Ag, Co, Fe, Ni
2. Oxide nanoparticles like $SiO_2$, $TiO_2$, CuO
3. Organic nanoparticles made from polymers
4. Other composite nanoparticles like ZnS, CdSe

However, it has to be noted that a clear categorization can sometimes be problematic as most metal nanoparticles for instance feature a metal oxide hull due to their high reactivity. Hence mentioned categories should only serve as a rough guide. Besides the chemical composition of the nanoparticle bulk, more elaborate techniques also allow for the doping of nanoparticles with a desired amount of hetero atoms in order to modify particle properties such as the catalytic activity [39].

Post processing techniques can greatly alter the chemical structure of particles. E.g. high temperature annealing can be employed to trigger crosslinking reaction in sol-gel based oxide nanoparticles leading to a shrinkage of particle size. Moreover, thermal treatments can also initiate crystallization processes facilitating the preparation of nanoparticles with desired crystalline phase.

In the context of this thesis, $SiO_2$ and $TiO_2$ nanoparticle systems were in focus. As both systems are commonly prepared via sol-gel based synthesis, particles used typically featured a spherical geometry with a narrow size distribution. Both structural characteristics rendered these

particles ideal model systems for fundamental studies as they facilitated the preparation of defined particle layers. In addition to the physical properties, the chemical structure of both materials played also a key role and will therefore be discussed in the subsequent chapters 2.4.1 and 2.4.2, respectively.

## 2.4. Surface chemistry and interfacial processes on oxide nanoparticles

### 2.4.1. Surface chemistry of $SiO_2$

Silicon dioxide is found to exhibit a great number of structures. Besides the many different amorphous species natively found in the nature, also multiple different crystalline structures are known of which α-quartz represents the most important. In fact, α-quartz is the second most common oxide species found on earth. In its pure state, every Si atom is surrounded by four oxide atoms in a tetrahedral fashion. Contrary to that, each oxygen atom is bound to two Si atoms. Due to the high covalent characteristic of these bonds, $SiO_2$ is found to be relatively hard when compared do other materials.

The interface chemistry of $SiO_2$ has been a field of ongoing research for many decades. In general, the two species identified on a silica surface are siloxanes (Figure 5-A) and silanols (Figure 5-B) [40,41]. For the latter, two main origins are commonly discussed in the literature. First, silanol groups are formed as a result of an incomplete condensation reaction during the process of silica preparation. Second, water molecules can rehydroxylate a surface siloxane species effectively turning it to a silanol group [40]. Moreover, detailed FT-IR [42] studies revealed the presence of multiple silanol species with different structures as depicted in Figure 5.

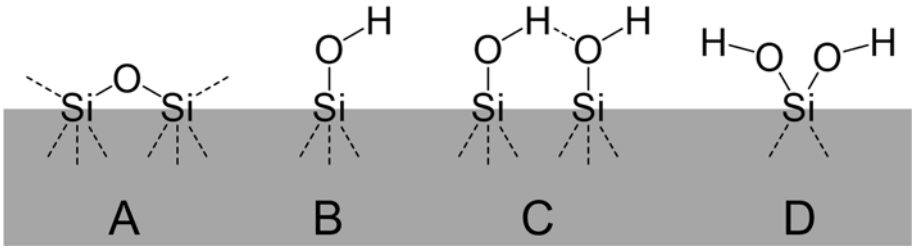


*Figure 5: Schematic of the four different surface species commonly found on silica surfaces. The surface siloxane (A) can be rehydroxylated by water molecules resulting in two isolated silanol groups (B) or either one vicinal (C) or germinal silanol (D) respectively.*

In this context, typically three distinct silanol structures are discussed among which the isolated silanols (Figure 5-B) feature the simplest structure. Isolated silanols consist of a silicon atom with three bonds to bulk bound oxygen atoms and one OH group facing away from the surface. In case two isolated silanols are located close enough they can form a hydrogen bond leading to the so called vicinal silanols (Figure 5-C). In addition to the schematic representation of this type, as depicted in Figure 5-C vicinal silanols can form longer chains consisting of multiple silanol groups. The last type of silanol groups commonly discussed are

the so called germinal silanols. Contrary to the previous two, the silicone atom features only two bonds to bulk related oxygen atoms and two surface OH groups. Typically, both the vicinal and germinal silanols can easily be removed by means of thermal induced water desorption leading to a surface siloxane and possibly isolated silanols [42]. These isolated silanols however are typically much more stable towards thermal treatment and desorb at much higher temperatures [42].

The density of the surface silanols is found to play a critical role for properties such as the hydrophilicity. In general, a higher density of surface silanols leads to a more hydrophilic surface whereas a decrease (e.g. after annealing) leads to increased hydrophobicity. Moreover, the number of silanol groups directly influences the water adsorption as these groups serve as preferred adsorption sites due to the interaction via hydrogen bonds with adsorbate species. Today, the complex interplay between the density, the distribution and the structure of surface bound silanols towards the adsorption properties is still a subject to many experimental as well as theoretical studies [43-46]. Further details regarding the water adsorption on these surfaces are discussed in section 2.4.3.

### 2.4.2. Surface chemistry of $TiO_2$

Titanium dioxide is known to exhibit eleven different crystal structures. However, only three of them are stable under ambient conditions and therefore relevant for most of the applications. The first of these thee structures is rutile. In its bulk, every Ti atom is surrounded by six oxygen atoms in an octahedral fashion. In contrast to that, the oxygen atoms feature a coordination number of 3 resulting in a trigonal planar structure of Ti atoms. The other two structures are anatase and brookite which feature a more complex crystal structure and are therefore not discussed at this point.

Today, $TiO_2$ plays a critical role in a huge number of products ranging from hi-tech applications like biomedical implants (biocompatibility of $TiO_2$) and photocatalysts in solar cells over to the applications as white pigment for common paints. Since in most of these applications the surface chemistry plays a key role, this topic is still a focus of many studies and has been reviewed in great detail by Diebold [47]. In order to derive general conclusions regarding the surface chemistry and reactivity of titania surfaces, most studies focus on

rutile (110) singly crystal substrates as this surface is found to be the most stable orientation. The (110) surface contains two distinct types of Ti and O atoms as depicted in Figure 6.

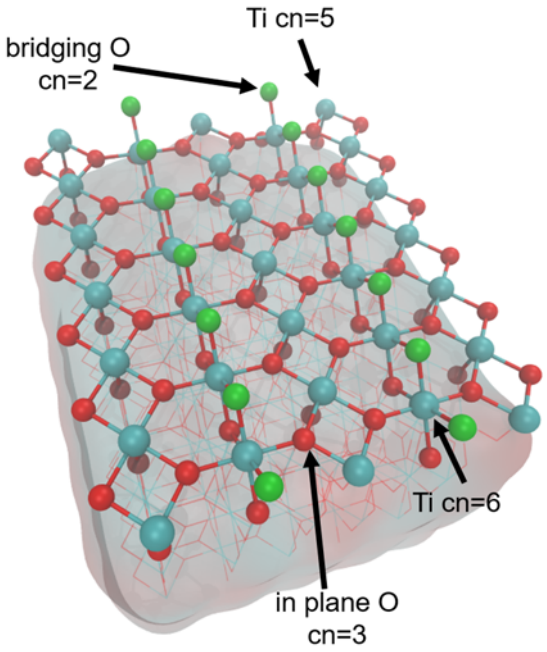


*Figure 6: Rutile (110) surface structure. Ti and O species with different coordination number (cn) are indicated by the arrows. For improved visibility the bridging oxygen atoms are depicted in green.*

Focusing on the Ti atoms, two species with a coordination number (cn) of 6 and 5 are found located along the [001] direction in an alternating fashion. The latter species features a dangling bond directed perpendicular to the surface and a formal oxidation number of 4+. With respect to the oxygen atoms, the two types commonly discussed are located in the surface plane with a coordination number of 3 as well as on top of the sixfold coordinated Ti atom. These so called bridging oxygen atoms feature a coordination number of 2 and are therefore subject to many studies as they are assumed to be easily removable and highly reactive. In fact, a recent UHV-AFM based study by Kunze, Giner, Torun and Grundmeier [48] showed that the presence of oxygen vacancies induced by $Ar^+$ ion bombardment had a tremendous impact on the adhesion force. Moreover, it was found that the defect density could be reduced by means of water dosing and subsequent annealing leading to a decreased adhesion force compared to the surface state with a high defect density. The mechanism discussed in the literature for the water induced decrease in oxygen vacancies defects is based on a dissociative adsorption leading to the formation of two surface bound hydroxyl groups in bridging position for every adsorbed water molecule [49-51]. Another key aspect of $TiO_2$ surfaces is their susceptibility towards photocatalytic processes when irradiated with UV-light. This topic will be discussed separately in section 2.4.4.

### 2.4.3. Water adsorption on $SiO_2$ and $TiO_2$ surfaces

Water is arguably one of the most important and abundant molecules on earth. It plays a critical role in almost every aspect of modern science due to its extraordinary chemical and physical characteristics. Hence, in the context of adsorbate species, water has attracted an enormous amount of interest. The vast number of publications available on the topic of the interaction of water with solid surfaces can easily overwhelm the reader. However, two reviews by Thiel and Madey [52] as well as by Henderson [53] provide an excellent overview of this topic. Therefore, only certain key aspects with relevance to this thesis will be discussed within this section.

In his review, Henderson described three fundamental scenarios for the water adsorption based on the different strength of water-water vs. water-surface interactions:

1. water-water int. > water-surface int. → cluster formation
2. water-water int. < water-surface int. → molecular water and hydrogen bonding
3. water-water int. << water-surface int. → water dissociation

In the context of this thesis and the substrates used, mostly the latter two cases are of interest as the first scenario is mostly found on noble metal surfaces. As briefly discussed in section 2.4.1, in the case of a partially silanol terminated $SiO_2$ surface, there are multiple possible adsorption structures for water molecules. E.g. water can adsorb in a dissociative fashion during the hydrolysis of a surface siloxane as depicted in Figure 7.

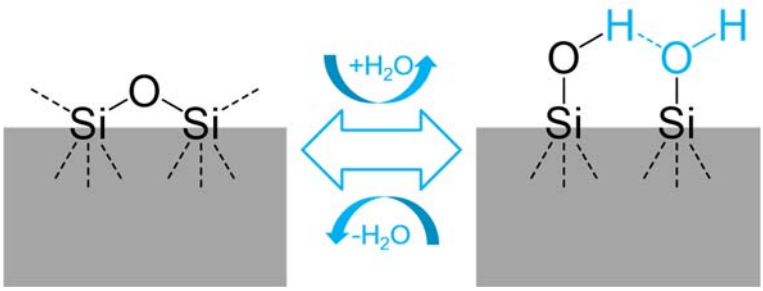


*Figure 7: Dissociative water adsorption leading to the hydrolysis of a surface siloxane with thy typical outcome of a vicinal silanol group.*

The depicted process however is typically highly reversible in its nature as a heat treatment can lead to the desorption of water resulting in the reformation of the siloxane species. In addition to the dissociative adsorption, multiple different structures of a hydrogen bond based adsorption can be found on these surfaces as presented in Figure 8.

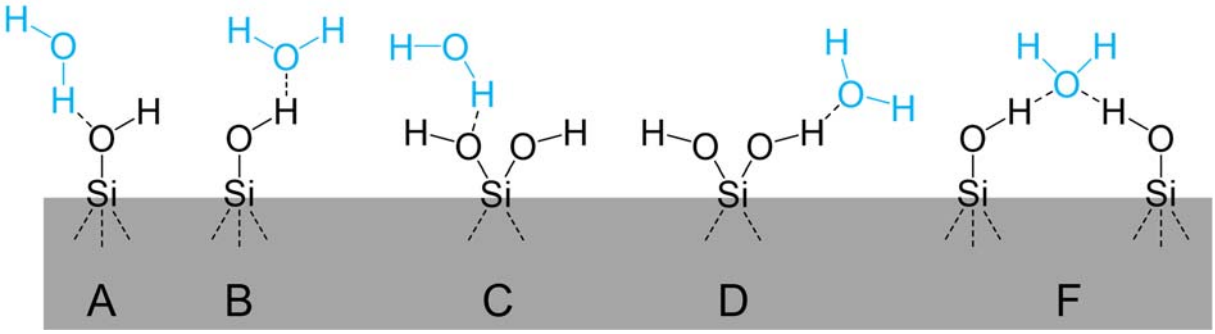


*Figure 8: Water adsorbed to different surface silanol groups.*

The simplest interaction is the hydrogen bond formation with either an isolated or germinal silanol. In both cases, the water molecule can form a bond with one of the hydrogen atoms acting as electron acceptor (Figure 8-A and C) or with the oxygen atom (Figure 8-B and D) donating one of the oxygen's lone pairs [40]. In addition to these rather trivial structures, more complex bridging types can occur as well, as depicted in Figure 8-F [40]. In this scenario, a single water molecule bridges two otherwise isolated silanol groups which featured a distance too large for a direct hydrogen bond interaction in the sense of a vicinal silanol. Of course this bridging interaction is not limited to isolated silanols but can also occur between other species as well. In addition, further hydrogen bonds between the water molecules are also possible in case the silanol density is high enough. If further water is dosed to the system, the first layer of adsorbed water can serve as an anchor for further water molecules building up a hydrogen bond network as depicted in Figure 9.

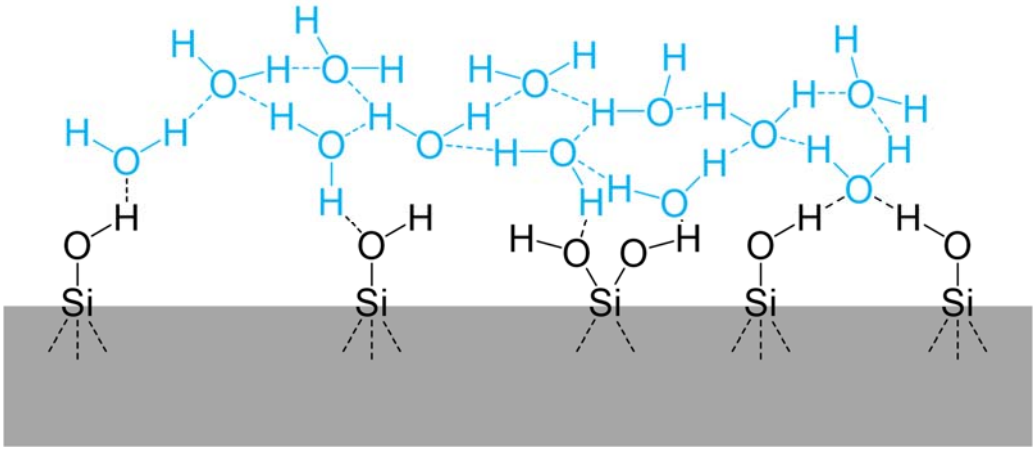

*Figure 9: Schematic of a water network on a silica surface covered with different types of silanols.*

Moreover, recent studies have indicated that the vibrational spectrum of water at interfaces is influenced by the ordering and structure of the molecules. In this context, the so called "ice-like" and "liquid-like" structures play an important role. An extensive discussion of these water structures and their vibrational spectra is presented in section 4.4.2.

In the case of a $TiO_2$ surface, the fundamental interaction based on surface hydroxyl groups is very similar to $SiO_2$. However, the origin of the surface bound hydroxyl groups is quite different. In the literature, there seems to be a general agreement that oxygen vacancy defects play a crucial role during the initial state as they influence the formation of surface hydroxyl groups in a profound way. Studies by Eplinger et al. [54] have indicated that water can bound to these defect sites in a dissociative fashion creating additional surface hydroxyls. However, as Diebold pointed out in her extensive review [47], there seems to be some disagreement regarding the conditions (e.g. temperature) under which this dissociative adsorption occurs. The general mechanism proposed for the dissociative adsorption consists of two steps: Initially a water molecule adsorbed onto an oxygen vacancy with its oxygen molecule. Subsequently a proton is transferred to a neighboring bridging oxygen. As a result, the adsorption of one water molecule generates two equivalent hydroxyl groups [55].

In addition to the influence of the oxygen vacancy defects, the fivefold coordinated $Ti^{4+}$ sites also play an important role as they facilitate the molecular adsorption of water [56]. As Henderson showed in his work, the water molecule adsorbed on the fivefold coordinated Ti sites with the hydrogen atom facing away from the surface. Furthermore, it was shown that the hydrogen bond interaction of such a water molecule is influenced by the distance between the hydrogen atom and the neighboring bridging oxygen atom. Since this distance depends on the crystal orientation, different crystals exhibited a different tendency. E.g. the distance between the Hydrogen atom of a molecular adsorbed water on a fivefold coordinated Ti site to the next bridging oxygen atom is found to be 2.8 Å for a $TiO_2$ (100) crystal and 3.2 Å for a $TiO_2$ (110) crystal [47]. Hence, in the latter case the rather long distance prevents any significant hydrogen bonding. Furthermore, Diebold states that this geometrical effect might also be the reason for the increased reactivity of oxygen vacancy sites on $TiO_2$ (110) sites with respect to water dissociation as this geometry seems to be particularly well-suited for hydrogen bond formation for water molecule adsorbed to these defects [47]. However, it has to be noted that the effects discussed in this section are still subject to ongoing research and results presented in this chapter represent only a small overview into a very complex topic.

### 2.4.4. Photocatalytic properties of $TiO_2$ surfaces and $TiO_2$ nanoparticles

UV-light induced catalysis on $TiO_2$ surfaces has been focus of extensive studies for many years and took its origin in a publication of Honda and Fujishima who famously observed the UV-light induced water cleavage on a combined $TiO_2$ / Pd anode [57]. Ever since, the application of titanium oxide as an active photo-catalyst has been brought to various fields ranging from purification of waste water to improved efficiency of solar cells [58-63].

On a fundamental basis, the photocatalytic activity of semiconducting materials is based on their special electronic structure. In contrast to metals which feature a continuum of energy states for their electrons, semiconductors exhibit a band gap (BG) between the populated valence band (VB) and the empty conduction band (CB). As a result, an electron can be excited by a photon of sufficient energy transferring it from the valence band to the conductance band as depicted in Figure 10-A. Consequently, this process leaves an electron hole in the valence band.

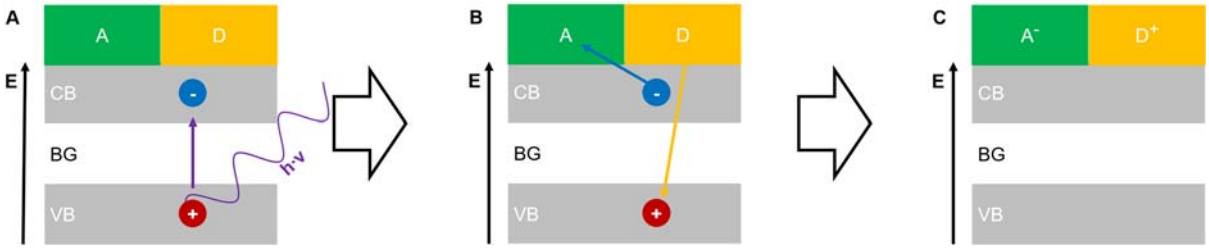


*Figure 10: Schematic of the photocatalytic process on a semiconducting material.*

Excited electrons feature a lifetime up to few nanoseconds which is long enough for various reactions. Typically, two competing processes are discussed. On the one hand, the excited electron can undergo recombination with the left vacancy (hole) either on the surface or in the volume with the only outcome of heat generation. On the other hand, the excited electron can be transferred to an electron accepting adsorbate (A) effectively reducing it. Accordingly, the created electron hole can also recombine with an electron from an adsorbed donor species (D) effectively oxidizing it.

In general, a good photocatalyst features a bad gap comparable or greater than the redox potential for the formation of reactive (typically oxygen rich) species. Although, various materials exhibit electronic prerequisites necessary to perform as good photo-catalysts, $TiO_2$ has attracted an enormous interest due to its high chemical stability, negligible toxicity and large scale availability. Comparing the two most relevant crystal phases of $TiO_2$, anatase is

found to feature a slightly larger band gap (3.2 eV) than rutile (3.0 eV) making it more active towards UV-light. However, in a recent study by Scanlon et al. [64], it was found that a mixture of both rutile and anatase exhibited certain synergistic effects resulting in a higher photocatalytic activity that each pure species on its own.

In the context of nanoparticles, photo-oxidation on titania particles plays an important role as it is commonly found that the wetting behavior of such particles can dramatically change upon irradiation due to the formation of additional surface hydroxyl groups. Hence the water adsorption and capillary bridge formation processes are influenced resulting in changed mechanical behavior of particle ensembles. Although the fundamental process of photo-oxidation has been extensively studied for many decades, it is still a topic of ongoing research. The hydrophilization of $TiO_2$ when exposed to UV-light is commonly attributed to the adsorption of water on oxygen vacancies generated by the transition of $Ti^{4+}$ to $Ti^{3+}$ species as a result of internal recombination with photon induced electron holes [65-68]. As this process is dissociative in nature, additional surface hydroxyl groups are being formed leading to the macroscopically detected increased wettability with water. In addition, Kunze, Torun, Giner and Grundmeier investigated the surface chemistry of $TiO_2$ (0001) single crystals prepared under ambient conditions [69] and influence of surface adsorbate species on nano-contact forces [48] in great detail.

## 2.5. Contact force models for inter-particle interactions

The theory of the fundamental interacting forces, which in most cases is based on electrostatic and van der Waals forces and their force-distance relationships have been reviewed in great detail by Israelachvili in his monograph on "Intermolecular and Surface Forces" [70]. However, as the presence of humidity cannot be neglected, the presence of capillary bridges plays a key role with respect to forces measured under ambient conditions. The actual measurement of interaction forces between individual microscopic particles under ambient conditions, mainly based on atomic force microscopy (AFM) methods, attracted a great deal of attention in the last few years and were extensively reviewed by Butt and Kappl [71,72]. In the subsequent two chapters, the inter-particle forces will be discussed based on van der Waals interactions (section 2.5.1) as well as due to the presence of capillary bridges (section 2.5.2).

### 2.5.1. Van der Waals interaction in particle systems

On a molecular level, the most fundamental interaction force is the so called Coulomb force which describes the interaction of two electrostatic charged objects. Although the actual size of the charged objects can vary over an enormously wide range, the same simple law holds true for the interaction of subatomic particles (interaction between electrons and nucleus) as well as for macroscopic objects (dust in an electrostatic filter):

$$F_{coulomb} = \frac{Q_A \cdot Q_B}{4\pi\varepsilon\varepsilon_0 D} \tag{2.2}$$

From equation (2.2) it can be seen that the Coulomb force solely depends on the charge of the interacting objects ($Q_A$, $Q_B$), the dielectric properties of the separating medium ($\varepsilon$,$\varepsilon_0$) and finally their distance (D). Although most molecules do not feature a permanent charge, they still exhibit an interaction force. This is due to the so called Keesom-, London-, and Debye-interactions which are all based on electrostatic interactions of unevenly charged molecules or atoms. The sum of all three contributions is commonly referred to be the so called van der Waals interaction.

If, for instance, a molecule A with a freely rotatable dipole moment is put close enough to a neutral but polarizable molecule B, molecule A may influence the electronic density of molecule B resulting in a so called induced dipole. This type of interaction is the so called Debye interaction and can be calculated by equation (2.3).

$$F_{Debye} = -\frac{6\mu^2 \cdot \alpha}{\left(4\pi\varepsilon_0\right)^2 D^7}$$
$$W_{Debye} = -\frac{\mu^2 \cdot \alpha}{\left(4\pi\varepsilon_0\right)^2 D^6} \tag{2.3}$$

In this case, as opposed to the total charge ($Q_1$ and $Q_2$) the dipole moment (μ) and the polarizability (α) have to be considered. Moreover, it is evident that the actual interaction range is much lower as the distance contributes to the equation with a power of 7 in the denominator.

In case of two freely rotatable dipoles in close proximity, both will tend to orient in such a fashion that the opposite charged sides are faceing towards each other effectively minimizing the potential energy. The resulting force is the so called Keesom interaction described by equation(2.4) which also considers the deviation from a perfect alignment as a result of thermal fluctuation. Compared to the Debye interaction, it is found that both feature the identical distance dependency.

$$F_{Keesom} = -2\frac{\mu_A^2 \cdot \mu_B^2}{\left(4\pi\varepsilon_0\right)^2 k_B T \cdot D^7}$$
$$W_{Keesom} = -\frac{\mu_A^2 \cdot \mu_B^2}{3\left(4\pi\varepsilon_0\right)^2 k_B T \cdot D^6} \tag{2.4}$$

Lastly, the so called London interactions have to be considered. These forces stem from the fluctuating charge induced by the rapid movement of the electrons in the atom hull. Therefore, at each given time every atom has an uneven distributed charge which in turn can interact with another atom in close proximity. This interaction can also be characterized with an equation looking very similar to the previous two:

$$F_{London} = -9\frac{\alpha_A^2 \cdot \alpha_B^2}{\left(4\pi\varepsilon_0\right)^2 D^7} \cdot \frac{h\nu_A\nu_B}{\nu_A + \nu_B}$$
$$W_{London} = -\frac{\alpha_A^2 \cdot \alpha_B^2}{2\left(4\pi\varepsilon_0\right)^2 D^6} \cdot \frac{h\nu_A\nu_B}{\nu_A + \nu_B} \tag{2.5}$$

In this case the interaction force is determined by the polarizability (α) and the ionization energy (hν). Moreover, this interaction obeys the same distance dependency as the other interactions.

As mentioned earlier in this section, the sum of all three contributions is commonly referred to be the van der Waals interaction which is typically found to be dominated by the London contribution. Hence, in order to simplify the otherwise rather bulky sum of equations (2.3), (2.4) and (2.5), all parameters characteristic for both interacting molecules/atoms are combined in a constant ($C_{AB}$).

$$F_{vdW} = -\frac{6C_{AB}}{D^7}$$
$$W_{vdW} = -\frac{C_{AB}}{D^6} \tag{2.6}$$

However, in the context of particle systems, it is important to note that all equation up to now did only consider individual molecules or atoms. If the interaction of two particles is to be determined the, interactions of every molecule/atom in one particle with each and every molecule/atom in the opposing particle has to be summed up to retain the total interaction force. This process has been extensively presented by Butt and Kappl [73] and is therefore not presented such great detail within this chapter. In essence, equation (2.7) can be derived describing the interaction force between two spherical objects with given radii $R_A$ and $R_B$.

$$F_{vdW} = -\frac{A_H}{6D^2} \cdot \frac{R_A \cdot R_B}{R_A + R_B}$$
$$W_{vdw} = -\frac{A_H}{6D} \cdot \frac{R_A \cdot R_B}{R_A + R_B} \tag{2.7}$$

In this context the Hamaker constant ($A_H$) is being introduced which is directly derived from the constant $C_{AB}$ mentioned earlier and the corresponding density of both materials.

$$A_H = \pi^2 \cdot C_{AB} \cdot \rho_A \cdot \rho_B \tag{2.8}$$

Most interestingly, due to the integration, the actual distance dependency was reduced considerably, resulting in a much longer effective distance for the van der Waals interaction. E.g. the effective van der Waals interactions for two perfect $SiO_2$ spheres, each with a diameter of 250 nm and dry air as separating medium can be estimated according to equation (2.7).

$$
\begin{aligned}
F_{vdW} &= -\frac{A_H}{6D^2} \cdot \frac{R_A \cdot R_B}{R_A + R_B} \\
&= -\frac{6.1 \cdot 10^{-20}\, J}{6 \cdot \left(1.7 \cdot 10^{-10}\, m\right)^2} \cdot \frac{125 \cdot 10^{-9}\, m \cdot 125 \cdot 10^{-9}\, m}{125 \cdot 10^{-9}\, m + 125 \cdot 10^{-9}\, m_B} \\
&\approx -22 \cdot 10^{-9}\, N
\end{aligned}
\tag{2.9}
$$

Using the corresponding, experimentally measured [74], Hamaker constant of the material combination $SiO_2$-Vacuum-$SiO_2$ of $61 \cdot 10^{-21}$ J and an effective distance of $1.7 \cdot 10^{-10}$ m, an attractive force of ≈-22 nN is found. As the $\varepsilon_0$ of air is very close to 1 this value calculated for vacuum as separating medium should be very close to that in air. However, it has to be kept in mind that in the case of an experiment under atmospheric conditions, the inevitable presence of humidity has a great impact on the vdW force as the corresponding Hamaker constant with water as separating medium are typically much smaller. For the mentioned example, the corresponding $A_H$ for $SiO_2$-water-$SiO_2$ is found to be $\approx 0.63 \cdot 10^{-20}$ J [75] resulting in a vdW force of only $\approx 2.3 \cdot 10^{-9}$ N. Moreover, equation (2.7) typically greatly overstates the van der Waals force when compared to experimentally derived values as small deviation from the ideal scenario can have enormous impacts on the observed force. E.g. an increase of the distance D from 1.7 Å to 3.4 Å, stemming from a certain roughness for instance, results in an $F_{vdW}$ of only $\approx 0.6 \cdot 10^{-9}$ N. Therefore, the subsequent chapter will present that in an ambient environment other contributions to the total inter-particle force have to be considered as well as they typically tend to dominate due to their lack of extraordinary high distance dependency.

### 2.5.2. Capillary forces in particle systems

In the case of an experiment with two small spheres in contact, it is typically found that the apparent contact force is much larger that the van der Waals force. The reason for this behavior are capillary bridges which form spontaneously in the presence of water in the surrounding medium. In this chapter, the analytical solution for the capillary force will be derived using the circular approximation, as the fundamental understanding of this effect is of crucial importance for the results presented in this thesis. Initially, the much simpler problem of a sphere-wall contact will be discussed as the corresponding solutions can then be easily transferred to a sphere-sphere contact in a later stage.

The fundamental effect of capillary bridge formation is based on two important principles: First the pressure inside of a liquid droplet is found to depend on both, its surface curvature ($r_1$, $r_2$) and the surface tension ($\gamma$) of the liquid. This effect was extensively investigated by both Thomas Young [76] and Pierre-Simon Laplace [77] which independently derived the same equation in 1805. Hence expression (2.10) is called the Young-Laplace equation.

$$\Delta p = \gamma \left( \frac{1}{r_1} + \frac{1}{r_2} \right) \tag{2.10}$$

Using this equation, the pressure difference between inside and outside of a liquid drop with any given two principle radii $r_1$ and $r_2$ can be calculated. In fact, this equation also plays an important role when measuring the surface tension of a liquid as many experiments for this purpose like the maximum bubble pressure method or capillary rise method are based on the measurement of the geometry or pressure of liquid drops.

The second important factor for the formation of capillary bridges is the increased vapor pressure over a curved liquid surface with respect to the corresponding smooth surface. This behavior was initially described in 1871 by Lord Kelvin [78] deriving the so called Kelvin equation (2.11). As opposed to the Young-Laplace equation, in this case also the molar volume ($V_m$) of the liquid has to be considered.

$$\ln \frac{p}{p_0} = \frac{2\gamma V_m}{rRT} \tag{2.11}$$

From equation (2.11) it might not be directly evident how this plays an important role for the capillary formation. However, using the Kelvin equation, a so called critical radius can be

derived for any given partial pressure of a liquid phase (e.g. water). According to example (2.12) for instance, assuming a relative humidity (RH) of 50% $r_{crit}$ is found to be ≈1.5 nm.

$$\begin{aligned} r_{crit} &= \frac{2\gamma V_m}{RT \cdot \ln(0.5)} \\ &= \frac{2 \cdot 72 \cdot 10^{-3} \frac{N}{m} \cdot 18 \cdot 10^{-6} \frac{m^3}{mol}}{8{,}314 \frac{J}{mol \cdot K} \cdot 294K \cdot \ln(0.5)} \\ r_{crit} &\approx -1.5 \cdot 10^{-9} m \end{aligned} \tag{2.12}$$

This value corresponds to the radius of curvature of a droplet which would be in thermodynamic equilibrium with the surrounding gas phase. In addition, it should be noted that the actual radius given by the equation is negative, indicating that curvature is directed away from the liquid towards the gas phase.

Any drop with a smaller curvature would start to grow due to condensation whereas any larger droplet would tend to shrink due to evaporation until the stable radius $r_{crit}$ is reached.

To further elucidate this behavior an example is created with a circular pore in a solid material featuring a triangular cross section as depicted in Figure 11.

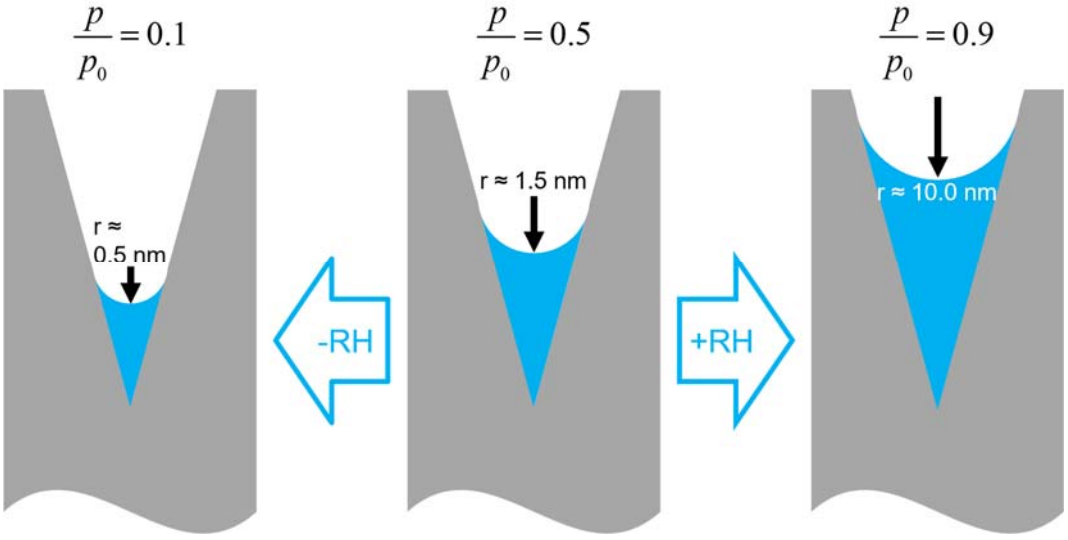


*Figure 11: Schematic of the pore condensation driven by the changed vapor pressure over a curved liquid surfaces as a function of relative humidity.*

At each given relative humidity, the pore will be filled with liquid until the critical radius of curvature given by the Kelvin equation has been reached. Further increase of the vapor pressure leads to a condensation process effectively filling the pore until the newly formed meniscus reaches a radius in thermodynamic equilibrium with the gas phase as predicted by the Kelvin equation. Moreover, the pressure difference within the liquid phase inside the pore can also be calculated using the Young-Laplace equation, resulting in a negative pressure difference due to the negative radius of curvature. Hence, it can be noted that the pressure within the liquid phase in the pore is lower than that of the surrounding gas phase.

Returning to the previously mentioned example of a sphere in contact with a plane, the contact region again can be characterized as a pore with radial geometry (Figure 12). In this scenario, the liquid will spontaneously start to condense in the contact region until it reaches a radius featuring a local vapor pressure equivalent to that of the corresponding component in the gas phase.

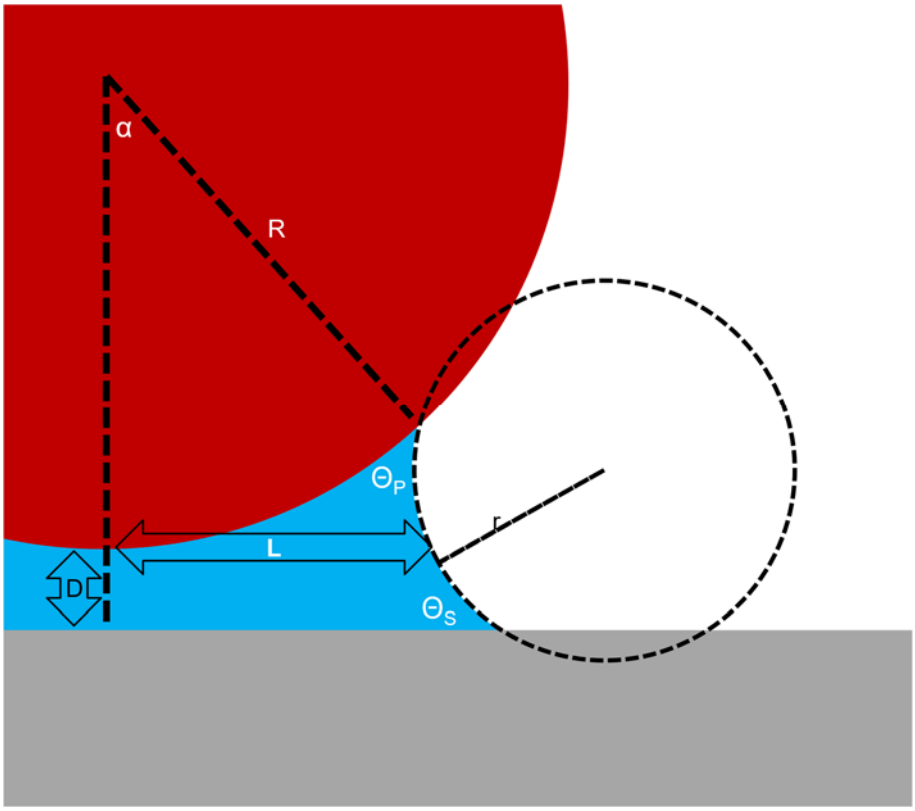


*Figure 12: Cross-sectional view of a sphere in proximity to a plane under ambient conditions with condensed liquid forming a capillary bridge. $\Theta_P$ and $\Theta_S$ indicate the contact angles on the particle and substrate, respectively. (Figure inspired from [73,79]).*

In this context, it would be important to derive an analytic expression allowing for the calculation of the attractive force as a function of parameters like the particle size, vapor pressure in the gas phase and wetting angle on both materials. Moreover, it would be desirable to also consider a finite distance between the plane and the solid in order to obtain a more general expression applicable for various scenarios.

In general, two forces contribute to the total force: on the one hand a contribution stemming from the liquids surface tension ($F_\gamma$), and on the other hand the force exerted by the Laplace pressure ($F_{\Delta p}$). Hence, expression (2.13) can be derived.

$$F_{cap} = F_\gamma - F_{\Delta p} \tag{2.13}$$

Focusing on the contribution from the surface tension, it is clear that it only depends on the length of the three phase contact line as this force by nature is only effective along it. Hence it depends on the depth (L) of the capillary, as presented in the cross section in Figure 12 leading to expression (2.14).

$$F_\gamma = 2\pi\gamma L \tag{2.14}$$

In contrast to that, the contribution of the Laplace-pressure exerts a force onto the liquids contact area instead which also depends on the cross-sectional depth L leading to equation (2.15).

$$F_{\Delta p} = \pi L^2 \Delta p \tag{2.15}$$

By combination of equation (2.10) and (2.15) equation (2.16) can be derived.

$$F_{\Delta p} = \pi\gamma L^2 \left( \frac{1}{L} + \frac{1}{r} \right) \tag{2.16}$$

Taking into account that the absolute value of r is much smaller than L, and r is negative due to the direction of curvature, it is evident that Δp will be negative too. Hence, the pressure within the liquid will be lower than that of the surrounding gas phase resulting in an overall attractive force between the particle and the plane.

In addition, it has to be noted that in both cases a simplification has been made as L equals the shortest distance between the contacts symmetry axis and the capillary meniscus. In fact, from Figure 12 it is evident that the real value of L should be slightly larger due to the curvature of the meniscus. However, as L >> r the error should be negligible.

Although, the two expressions (2.14) and (2.15) seem to be very simple, it has to be noted that the depth L itself again depends on the radius of curvature r and thus on the vapor pressure. Therefore, a substitution for L has to be derived establishing the connection of the vapor pressure and the total capillary force. Ideally, as the capillary radius r can directly be derived from the vapor pressure via the Kelvin equation, a substitution of L including the geometrical aspects of the contact (e.g. particle radius R) through r would be feasible. For this reason an opening angle (α) can be defined as depicted in Figure 12.

$$L = R\sin(\alpha) \tag{2.17}$$

Introducing equation (2.17) to equations (2.14) and (2.15) leads to expressions (2.18) and (2.19), respectively.

$$F_{\gamma} = 2\pi\gamma R\sin(\alpha) \tag{2.18}$$

$$F_{\Delta p} = \pi R^2 \sin^2(\alpha)\Delta p \tag{2.19}$$

Subsequently, component Δp in equation (2.19) can be substituted by the corresponding Young-Laplace equation (2.10) under the assumption that L>>r, leading to expression (2.20)

$$F_{\Delta p} = \pi R^2 \sin^2(\alpha)\gamma\left(\frac{1}{L}+\frac{1}{r}\right) \approx \pi R^2 \sin^2(\alpha)\gamma\left(\frac{1}{r}\right) \tag{2.20}$$

In Addition, it has to be considered that the direction of $F_{\gamma}$ is not directed vertically but orthogonal with respect to the content tangent. Hence, only a certain fraction, $F_{\gamma\parallel}$, contributes to the overall capillary force.

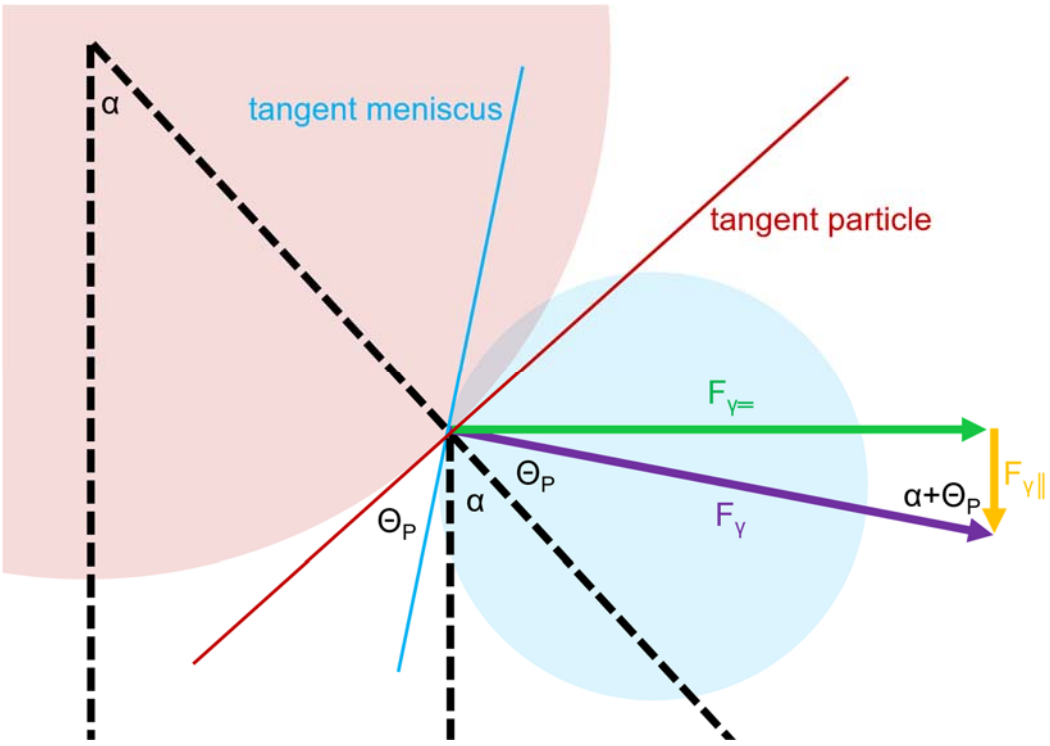


*Figure 13: Diagram for the evaluation of the effective fraction of Fγ.*

From the trigonometrical plot in Figure 13 it can be concluded that $F_{\gamma\parallel}$ can be calculated via equation (2.21) in case the contact angle $\Theta_P$ and the opening angle α are known.

$$F_{\gamma,\parallel} = \sin\left(\alpha + \Theta_1\right) \cdot F\gamma \tag{2.21}$$

Finally, equation (2.21) and (2.20) can be combined with (2.13) resulting in equation (2.22) which describes the total capillary force.

$$\begin{aligned} F_{cap} &= F_{\gamma,\parallel} - F_{\Delta p} \\ &= 2\pi\gamma R \sin\left(\alpha\right)\sin\left(\alpha + \Theta_1\right) - \pi R^2 \sin^2\left(\alpha\right)\gamma\left(\frac{1}{r}\right) \\ &= \pi\gamma R \sin\left(\alpha\right)\left[2\sin\left(\alpha + \Theta_1\right) + \sin\left(\alpha\right)R\left(\frac{1}{r}\right)\right] \end{aligned} \tag{2.22}$$

Comparing the two contributions in the square brackets it can be noted that since R>>r the term R·(1/r) will be much larger than 2 effectively dominating the bracket. Hence, it can be concluded that the force stemming from the line tension plays a minor role an can be neglected resulting in the much simpler expression (2.23).

$$F_{cap} = \pi\gamma R^2 \sin^2\left(\alpha\right)R\left(\frac{1}{r}\right) \tag{2.23}$$

Finally, a substitute for the factor $\sin^2(\alpha)$ has to be found which Butt and Kappl [79] showed in great detail. They derived in a rather lengthy process expression (2.24):

$$\sin^2(\alpha) = \frac{2r\left(\cos(\Theta_1)+\cos(\Theta_2)\right)-2D}{R_1} \tag{2.24}$$

which can be inserted to equation (2.23) resulting in the analytical solution of the capillary force (2.25).

$$F_{cap} = 2\pi\gamma R\left(\cos(\Theta_1)+\cos(\Theta_2)-\frac{D}{r}\right) \tag{2.25}$$

Equation (2.25) allows for the direct calculation of the capillary force for any given set of parameters. Exchanging the particle radius R for a reduced radius R* as depicted in Figure 14, extends the applicability of the analytical solution to particle-particle contacts.

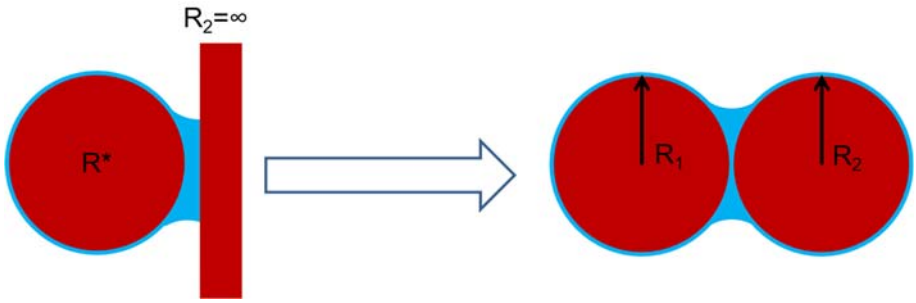


*Figure 14: Schematic for the introduction of the reduced radius R* in order to employ equation (2.25) on particle-particle contacts.*

In this context, R* is defined by equation (2.26).

$$R^* = \frac{R_1 \cdot R_2}{R_1 + R_2} \tag{2.26}$$

It should be noted that in the case of D=0 the capillary force becomes independent of r and thus from the relative humidity. Hence, in the case of a direct contact, the decrease in the capillary pressure induced by an increase in relative humidity is canceled out by the increase of covered particle area which the pressure acts on.

E.g. the effective capillary force for two $SiO_2$ spheres, each with a diameter of 250 nm and a wetting angle of 10° at a relative humidity of 50% can be estimated according to equation (2.12) and (2.25):

$$\begin{aligned} F_{cap} &= 2\pi\gamma R^* \left( \cos(\Theta_1) + \cos(\Theta_2) - \frac{D}{r} \right) \\ &= 2\pi \cdot 72 \cdot 10^{-3} \frac{N}{m} \cdot 62.5 \cdot 10^{-9} m \cdot \left( \cos(10) + \cos(10) - \frac{1.7 \cdot 10^{-10} m}{-1.5 \cdot 10^{-9} m} \right) \\ &= 58.8 \cdot 10^{-9} N \end{aligned} \tag{2.27}$$

Comparing the contribution to the pure van der Waals force calculated in the previous section according to equation (2.9), it is found that the overall contact force is dominated by the capillary interaction. This holds especially true for real samples as the van der Waals force quickly diminishes upon small increases of D.

Beside the many advantages of this rather simple solution, it also bears few limitations. In fact, equation (2.25) only holds true in case of a thermodynamic equilibrium at all times. Hence, in order to predict the energy necessary for the separation of two particle held together by a capillary force, the separation speed has to be low enough so that the meniscus is in thermodynamic equilibrium at all times. As a consequence, for most experimental approaches, this is a limiting factor as the separation often is performed under almost isochoric conditions. Therefore, the capillary radius is no longer determined by the Kelvin equation leading to deviating capillary forces from the predicted values. However, Butt and Kappl were also able to derive an analytic solution for this case [79].

Another very important limitation can be found in the particle size. Dörmann and Schmid [80] recently developed a new method for the calculation of the capillary force based on an numerical approach. They found that many of the assumptions made during the derivation of the analytical solution for the capillary force do not apply to particles in the low nm range.

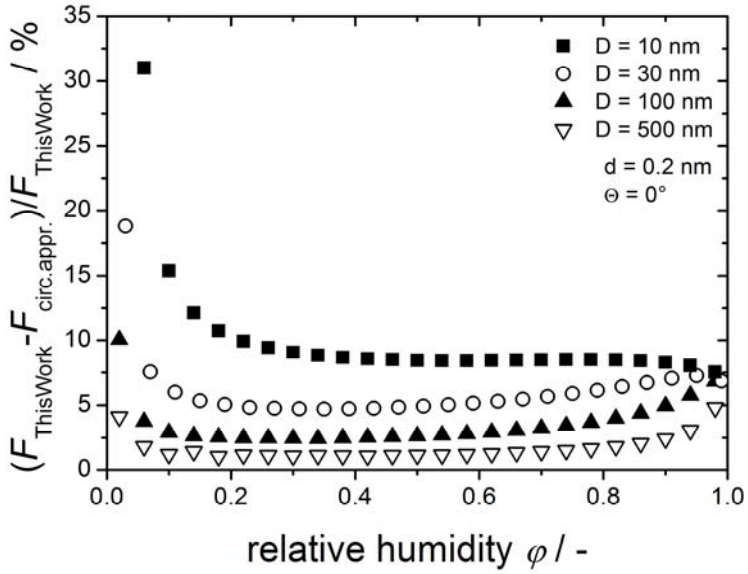


*Figure 15: Difference of the capillary force calculated by Dörmann et al. and the analytic solution plotted vs. the relative humidity. It can be seen that the analytical solution deviates especially for small particles at low relative humidity values. (Figure provided by M. Dörmann. Comparable version published in [80]).*

As presented in Figure 15, especially for small particles at low relative humidity, the circular approximation seems to lead to considerable errors for the predicted capillary force. Therefore, their proposed numerical approach should be preferred in the case of particles in the few nm range or for contacts in the ultra-low relative humidity range.

## 2.6. Fundamentals of analytical methods for particle characterization

This chapter contains a summary of the most important analytical techniques employed within the scope of this thesis. Each subsection begins with a brief summary regarding the origins of the technique followed by a detailed discussion of the fundamental principles behind the method.

### 2.6.1. Scanning electron microscopy

Scanning electron microscopy (SEM) is one of the most common techniques for the characterization surface morphologies. Its origin dates back to 1925 when Busch set the foundation for the development of modern SEMs discovering that magnetic fields could be employed for focusing electron beams in analogy to lenses used in optics. However, it was not before 1931 when Knoll and Ruska were first to publish images obtained by scanning an electron beam over a sample surface [81]. Nevertheless, as their device did not feature any high magnification capabilities, the development of the first microscope using a scanned electron beam is commonly attributed to the work of von Ardenne in 1937 who was first to use additional magnetic lenses in order to create an electron beam with ≈10 nm diameter [81]. More recently however, a new type of scanning microscopes using ultra fine beams of He ions has attracted much interest [82].

As all scanning techniques, the surface is probed line by line while collecting a characteristic signal. In the case of SEM the probe used is a thin beam of accelerated electrons with a typical diameter in the range of a few nanometers. In this context, devices employing a so called field emitter (FE) for the generation of these fine electron beams are commonly known to feature extraordinary high resolutions. These devices are typically referred as FE-SEMs.

When an accelerated electron from an incident beam hits a surface it can interact with the specimen in four different ways (Figure 16):

First, the incident electron can interact with other electrons in the specimen surface emitting them from their orbitals. These electrons however, feature a much lower kinetic energy than those of the incident beam and are therefore called secondary electrons. Although the incident beam penetrates up to a few µm deep into the sample only secondary electrons from the top few nm can reach out of the sample due to the short mean free path of electrons in solid

matter. Remaining secondary electrons from within deeper in the sample get absorbed on their way out and are therefore not detected. In fact, secondary electrons are actually responsible for the vast majority of the signal collected from the sample during imaging SEM.

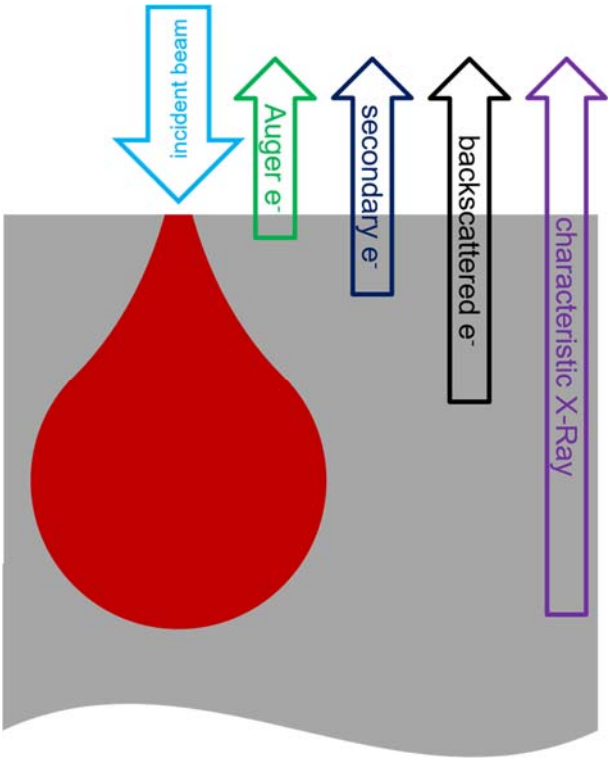


*Figure 16: Schematic of the excited volume during scanning electron microscopy with its characteristic drop shape. The four arrows indicate the different information depths accessible from the different interaction products. Typically, Auger electrons originate from the top most 1 to 2 nm of the surface whereas the secondary electrons can escape from as deep as ≈50 nm. Due to the much higher kinetic energy the backscattered electrons feature an escape depth of up to a few 100 nm. Lastly the characteristic X-rays generated by the incident beam feature the lowest surface sensitivity and can originate from the whole excited volume as they can easily penetrate through the specimen.*

Second, as opposed to the generation of secondary electrons, an incident electron can also be reflected preserving most of its kinetic energy. Therefore, so called backscattered electrons, feature a much higher mean free path within the sample resulting in a higher information depth. Some of the commercial available spectrometers can distinguish between both secondary and backscattered electrons by applying a retarding field to the detector deflecting the slower secondary electrons while letting the much faster backscattered electrons pass to the detector. This helps to get clear images on insulating samples as the much faster backscattered electrons are less affected by surface charging.

Third, in addition to the full reflection or generation of secondary electrons the incident electrons can also generate characteristic X-ray radiation which can be used for elemental analysis.

Fourth, so called Auger-electrons stemming from an intra-atomic process can be emitted from the sample surface. However, the two latter processes play a negligible role for the actual SEM imaging and are more interesting for other complimentary techniques as for instance the so called energy dispersive X-ray spectroscopy (EDX) or Auger electron spectroscopy (AES).

In the context of particle analysis SEM provides a powerful tool for the screening of particle ensembles as the sample preparation is very simple. Typical particle properties accessible by SEM analysis are the particle size and morphology. Moreover, employing statistical methods the size distribution of the particle material can be estimated. However, it has to be kept in mind that the number of particles measured for this analysis is only a small fraction of all immobilized particles and typically by orders of magnitude lower than for methods probing a volume like light scattering experiments for instance.

### 2.6.2. X-ray photoelectron spectroscopy

X-ray photoelectron spectroscopy is powerful tool for probing interfaces which had its breakthrough in the 1950s with the first high energy measurement published by Siegbahn et al. [83]. The technique is based on the photoelectric effect initially discovered by Hertz [84] in 1887. Hertz found that UV-light irradiated on metal substrates resulted in the emission of electrons from the substrate material. Nevertheless, he was not able to fully understand and explain this effect. Finally, Albert Einstein published his famous paper [85] in 1905 explaining the photoelectric effect based on the hypothesis that light consists of particles called photons, for which he earned the Nobel Prize in 1921.

During the XPS measurement the specimen is irradiated with X-ray photons of a known energy. As a result of the irradiation, electrons are emitted from the sample with a certain kinetic energy ($E_{kin}$) which depends on the binding energy of the electron in the atom shell ($E_{binding}$), the work function ($\Phi$) and most importantly the energy of the incident X-rays ($E_{X\text{-}ray}$).

$$E_{kin} = E_{X-Ray} - E_{binding} - \Phi \tag{2.28}$$

Following equation (2.28) the binding energy of the electron can be directly derived from their kinetic energy if the other parameters are known. During the actual experiment, the kinetic energy of the photoelectrons is being detected. However, as the sample is permanently irradiated, electrons with all sorts of kinetic energies are constantly emitted. Hence, they have to be filtered and subsequently detected. This is typically done by means of a kinetic filter which scans through the whole kinetic energy range to be measured, letting only electrons with a specific kinetic energy pass at any given time (Figure 17). As a result, an energy dispersive spectrum can be acquired as a function of time.

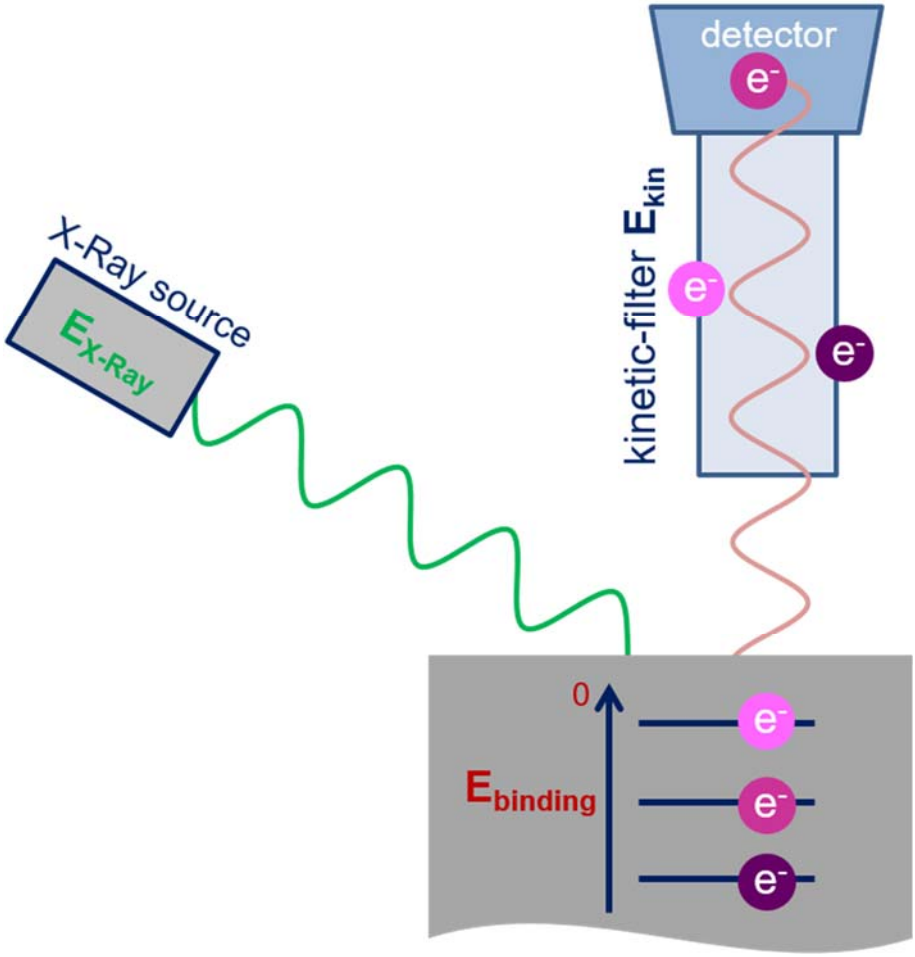


*Figure 17: Schematic of the main components for the XPS analysis. Electrons emitted by the incident X-ray are sorted by the kinetic filter based on their speed. With the given setting for the kinetic filter only electrons from the intermediate energy level can pass through the filter. More firmly bound electrons from the lower level are to slow to pass whereas weakly bound electrons from the outer level have a too high kinetic energy. By scanning the parameters of the filter the spectrum can be generated.*

From an experimental point of view, XPS has to be performed under ultra-high vacuum conditions in order to ensure a long enough mean free path for the electrons to be measured. For this reason, both the apparatus itself and the sample preparation is rather complex. To produce ultra-high vacuum conditions in the spectrometer a vast array of different pumping

systems has to be used. Moreover, the system is very sensitive towards electromagnetic filed making it necessary to shield the spectrometer from any external influence. For all this reason the experimental setup is very complex as depicted in Figure 18.

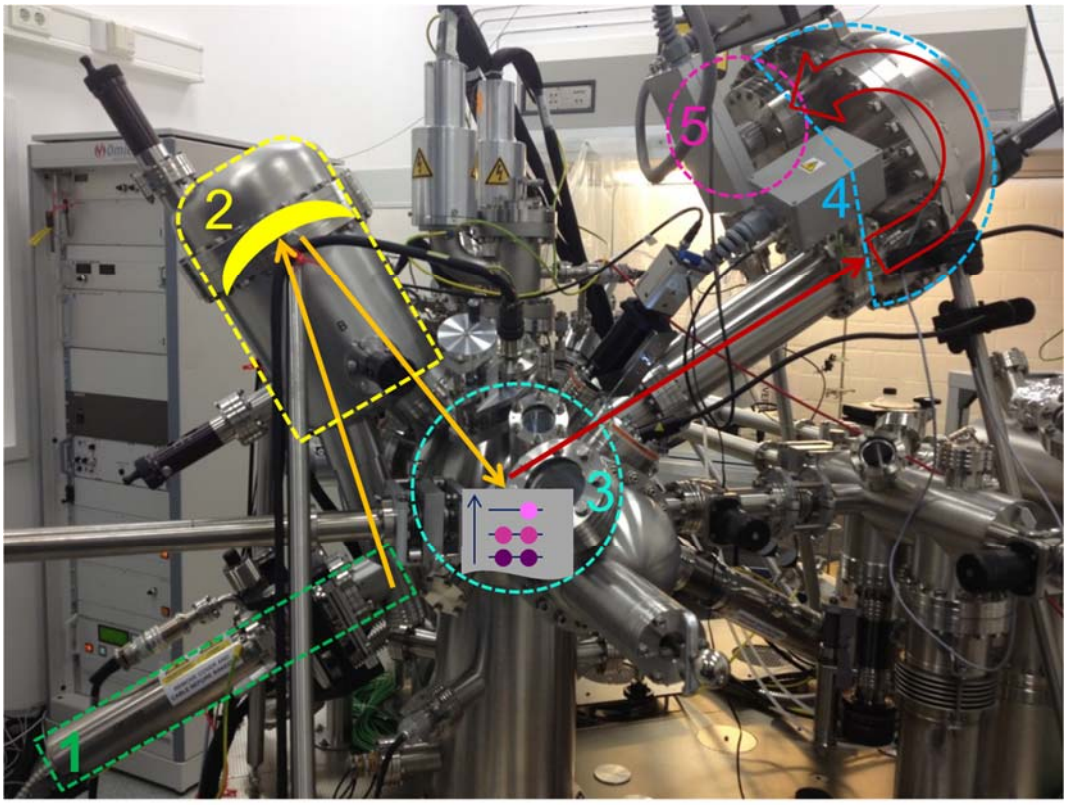


*Figure 18: Experimental setup for XPS analysis in the group of Prof. Dr. Grundmeier. System depicted has been custom build by Omicron Nanotechnology. Main components for the XPS analysis are the X-ray source (1) featuring a monochromator (2) both attached to the analysis chamber (3). Photoelectrons emitted are filter by the hemispheric analyzer (4) based on their kinetic energy before they are counted on the detector (5).*

Most interestingly the binding energy of the electrons detected is characteristic for the element type, as well as the corresponding atom orbital it originated from. However, detected peaks bear much more rich information than simply the elemental species as the apparent binding energy features a so called chemical shift as a function of the electron density at the atom. E.g. a positively charged atom tends to bind the remaining electrons more firmly to the core resulting in a slightly larger $E_{binding}$, whereas a negatively charged atom would exhibit the same effect but in an opposite direction.

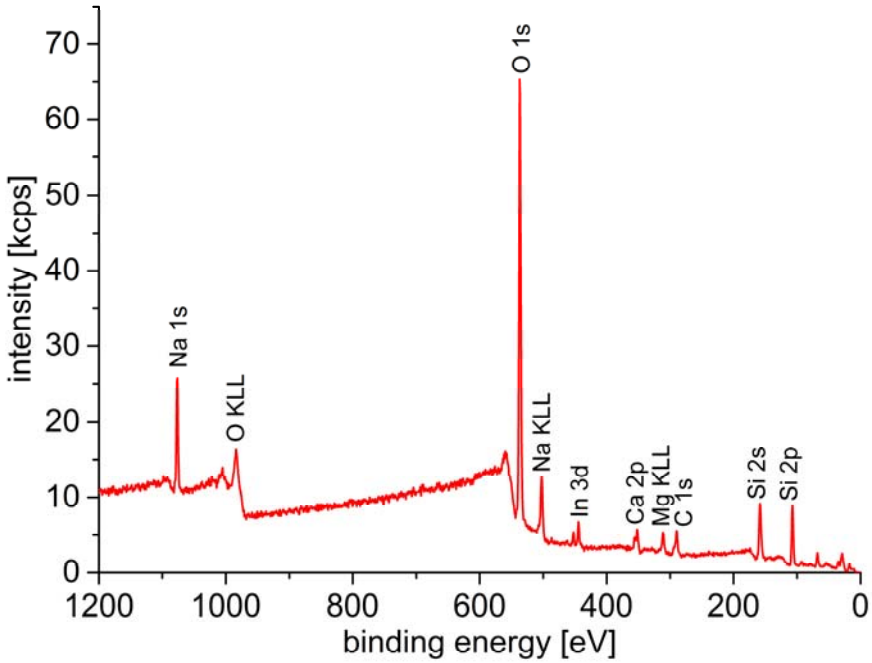


*Figure 19: Typical survey spectrum of glass particles. Spectrum presented was acquired using an Al ka source equipped with a monochromator. It can be seen that the characteristic lines are distributed among the whole spectral range with negligible overlap. Indium peaks around 444 eV originate from the matrix used to immobilize the particles as discussed in this section 3.5.2. Particles for this measurement were provided by the group of Prof. Dr. Thomas (University of Magdeburg).*

As the actual width of a peak in any given spectrum is typically in the range of a few electron Volts (eV) whereas the whole spectral range is only limited by the energy of the incident X-rays (typically 1400-3000 eV), most of the signals feature almost no overlap facilitating a detailed evaluation of the peaks (Figure 19). Using a suitable library containing reference values, it is possible to distinguish different oxidation states in the specimen with very high sensitivity by deconvolution of peaks with respect to species of the identical element featuring different oxidation states. A corresponding example of the peak-deconvolution of a C 1s peak is depicted in Figure 20.

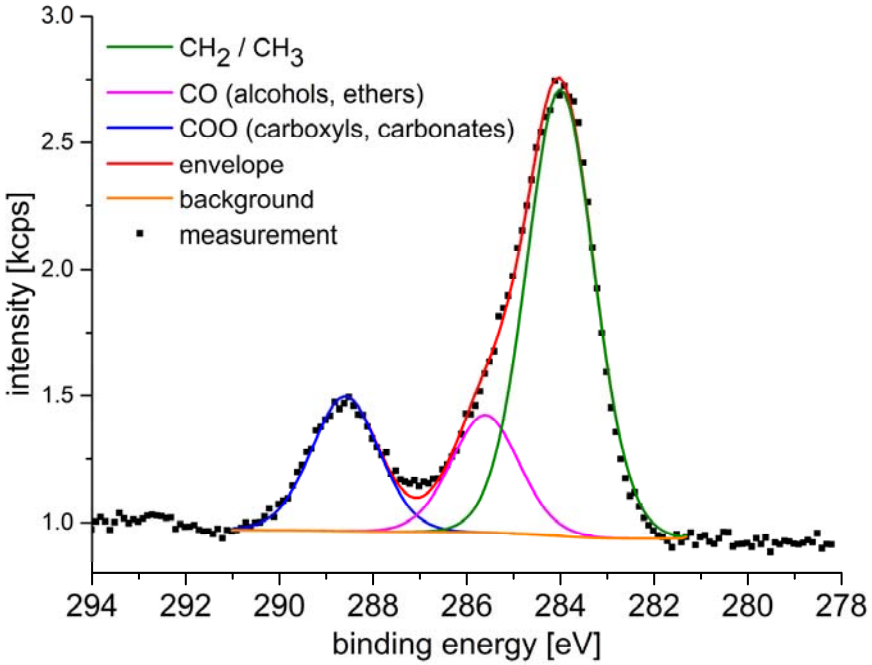


*Figure 20: Deconvolution of the carbon 1s peak from the sample presented in Figure 19 with respect to different oxidation states. Peak-fitting was performed using a peak shape consisting of a convolution of a gauss (30%) and lorentzian (70%) shape.*

Furthermore, the information depth is only in the range of a few nanometers as the escape depth of the photoelectrons is very limited due to the short mean free path in solid materials.

In the context of particle analysis, XPS provides a powerful tool for the characterization on particle surface chemistry. However, in contrast to classic XPS samples such as single crystals, metals or semiconductor substrates, the sample preparation is much more complex. Typically, conventional samples are being screwed or soldered to sample mounts in order to ensure a proper grounding for charge compensation. However, as it is hardly possible to solder an individual nanoparticle, other methods were employed. It was found that indium was a good material for particle immobilization due to its very ductile behavior. In addition, Indium was an element not present in the particles studied in this work making its peaks easily distinguishable from the particle signals. Additional details regarding the sample preparation are presented in section 3.5.2.

### 2.6.3. Fourier transform infrared spectroscopy

Infrared spectroscopy is one of the most common spectroscopic methods found in modern labs with its origin dating back to the early 19th century. In principle, this method makes use of the fact that according to Plank's equation (2.29) the light in the infrared regime features an energy comparable to that necessary for the attenuation of molecular vibrations and rotation.

$$E = h\nu = h\frac{c}{\lambda} \tag{2.29}$$

However, as the experiments presented within this work manly focus on the spectroscopy on solid objects, the detailed discussion of the attenuation of molecular rotation will be omitted within this chapter.

The simplest quantum mechanical model to describe the molecular vibration is that of the harmonic oscillator. Assuming a simple molecule consisting of only two atoms like carbon monoxide for instance, it can be described by two masses, corresponding to the atoms, connected via a spring corresponding to the covalent bond. In quantum theory this system can be described by a particle in a harmonic potential as described by equation (2.30) which gives the potential energy (U) of the system as a function of the mass (m), the spring constant (k) and the deflection (x). Moreover, as the motion is sinusoidal in nature the potential can also be expressed as a function of the angular velocity (ω).

$$U(x) = \frac{1}{2}kx^2 = \frac{1}{2}m^*\omega^2x^2 \tag{2.30}$$

Similar to the process described in section 2.5.2, a system consisting of two attached masses can be simplified to a similar system with only one reduced mass (m*) employing equation (2.26) using masses instead of radii.

Solving the time dependent Schrodinger equation for its eigenvalue gives the corresponding energy levels as described by equation (2.31) with the quantum number n ($n \in \mathbb{N}_0$).

$$E(n) = \hbar\omega\left(n + \frac{1}{2}\right) \tag{2.31}$$

In case the energy of an incident photon equals the energy difference between two energy levels with different quantum numbers, the molecule can absorb the photon at the expense of being excited to the corresponding higher level. In general, every molecule features different

modes of oscillation. The total number depends on the structure of the molecule and the number of atoms (a) it consists of. For linear molecules the number of vibrational modes is found to be 3a-5 whereas nonlinear molecules feature 3a-6 modes. In addition, the energy level transitions are also limited by special selection rules only allowing for certain transitions. As a consequence, only vibrations associated with a change in dipole moment are "IR active". In the case of a water molecule for instance, three IR active modes can be identified as depicted in Figure 21.

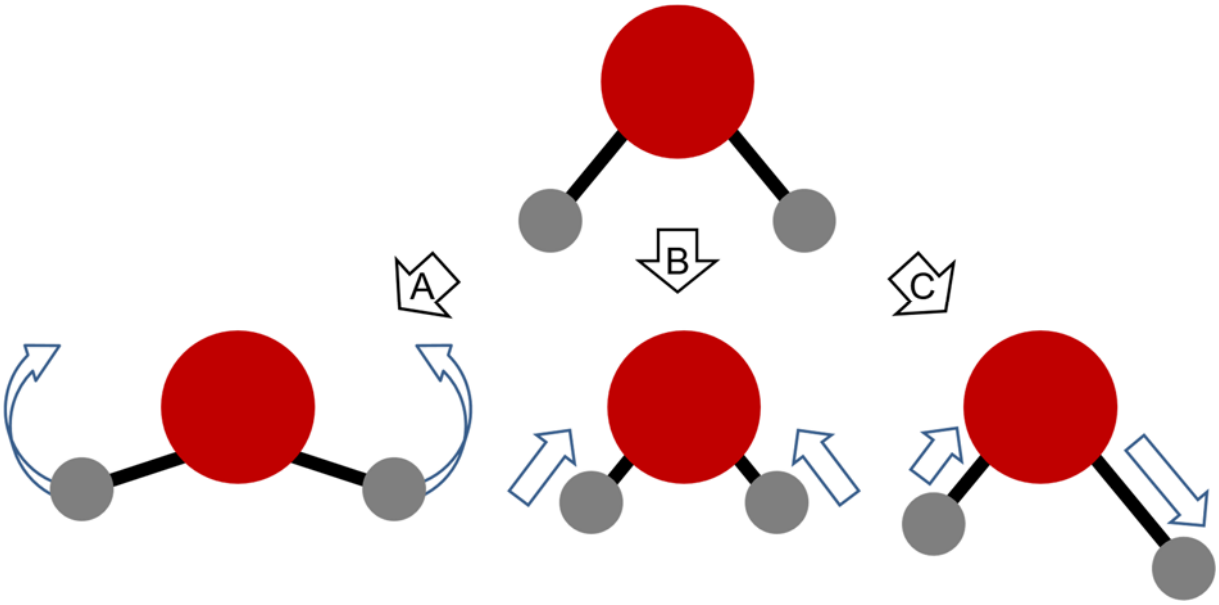


*Figure 21: Schematic of the different IR active vibrational modes of water. Depicted are the bending (A), symmetric stretching (B) and asymmetric stretching (C) mode.*

The simplest IR experiment would be the subsequent irradiation of a specimen by IR light with varying wavelength combined with a detector analyzing whether a certain wavelength is being absorbed or not. This so called energy dispersive method was very common in the early stages of this technique. Typically, either a prism or a grid was used to dismantle the incident, polychromatic IR light into different wavelengths. Today's setups however are based on a more sophisticated approach which allows for much faster measurements using a Michelson interferometer. Hence, instead of just but one wavelength at a time, an interferogram is being measured which contains the combined information of all wavelengths. Employing Fourier transform, the actual IR spectrum is then generated from the interferogram. As a consequence, the time necessary to collect one spectrum is much lower than in dispersive mode effectively allowing for the averaging of hundreds of spectra for improved signal to noise ratio within few minutes.

The amount of infrared light being absorbed by a specimen is given by the Beer-Lambert law (equation (2.32)) which correlates the absorbance (A) at any given wavelength with the specific extinction coefficient (ε) and the thickness (d) of the analyzed layer to the concentration (c) of the compound in the specimen.

$$A(\lambda) = \log\left(\frac{I}{I_0}\right) = \varepsilon_\lambda cd \tag{2.32}$$

In this context it has to be noted that IR related techniques are typically not very surface sensitive (exceptions like PM-IRRAS set aside) as the volume of material at the interface is small in contrast to the bulk volume. Therefore, it has become common practice to use difference spectra in order to emphasize surface related processes by dividing the absorbance spectrum of a specimen through a spectrum measured on a reference substrate. Figure 22 illustrates this by depicting two spectra of an identical sample. In this example, the red curved shows the single channel transmission spectrum of the specimen as measured by the detector. On the contrary, the black curve shows the corresponding absorption spectrum generated by division of the single channel spectrum through a measurement performed on a reference sample under identical conditions. It can be seen that the atmospheric water related signals around ≈1600 $cm^{-1}$ and ≈3750 $cm^{-1}$ as well as the contribution of $CH_2$ and $CH_3$ related signals around ≈2900 $cm^{-1}$ are either significantly reduced or in the latter case completely removed. This clearly indicates that all three signals are not characteristic features of the actual sample but rather stem from environmental (IR-active species in the atmosphere) or device specific origins (adsorbates on mirrors and windows). Moreover, the onset of the H-O-H deformation signal (≈1600 $cm^{-1}$) is only visible once the superimposed atmospheric water contribution has been reduced.

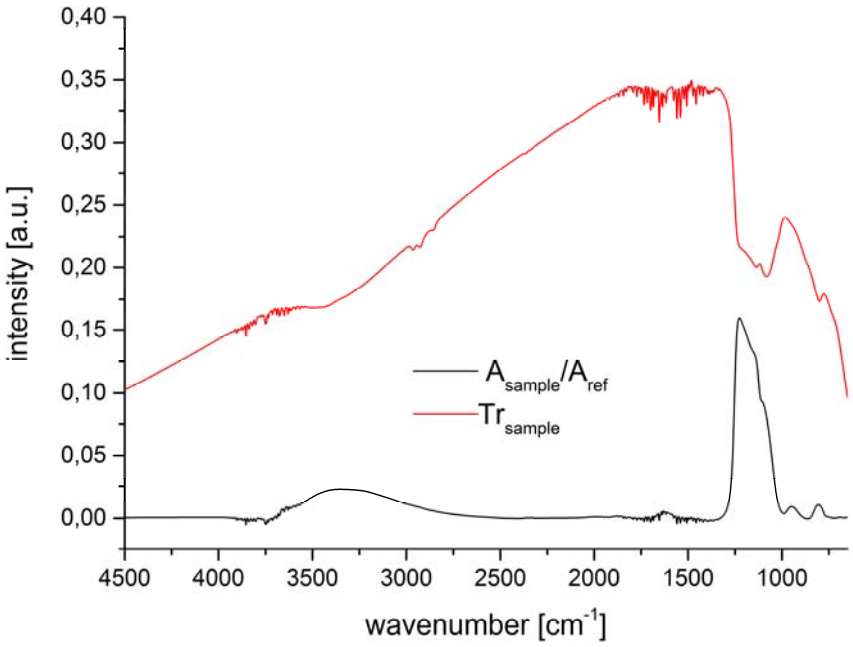


*Figure 22: FT-IR spectrum of $SiO_2$ nanoparticles at 10% relative humidity. The red curve represents the single channel transmission spectrum as measured by the detector whereas the black graph shows the identical data as a difference spectra based on the measurement of a reference sample at identical experimental conditions.*

In the context of the analysis of particles however, the transmission experiment plays only a minor role. Although, a particle specimen could be embedded in a IR-transparent matrix like KBr for transmission spectroscopy, other IR based techniques like reflectance based experiments both direct (IRRAS) and diffuse (DRIFTS) as well as attenuated total reflection IR spectroscopy (ATR-IR) are much more common (Figure 23).

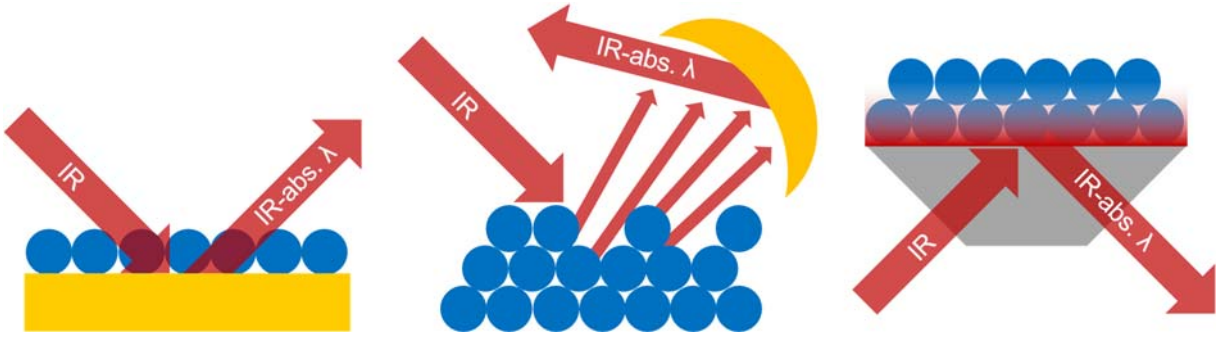


*Figure 23: Schematic of a IRRAS (left), DRIFTS (center) and ATR (right) based experiment for the analysis of particle ensembles.*

In case of IRRAS experiments, a small amount of the specimen is immobilized on a mirror material like gold or aluminum which reflects the incident IR light passing through the sample. However, the actual amount of specimen has to be chosen carefully such that no total absorption takes place. In contrast to IRRAS, DRIFTS experiments do not need any underlying mirror substrate. Instead, the diffuse reflected light is being collected by large concave mirrors with wide angle acceptance facilitating the probing of very rough surfaces.

For this reason, DRIFTS is an ideal technique for quick probing of particle powers as the sample preparation is very simple. Finally, ATR-IR utilizes the evanescence flied which emerges from the surface of a crystal in which internally an infrared beam is being totally reflected. In essence, the whole volume of this evanescence filed is being probed. However, it has to be kept in mind that the depth of this field is a function of the wavenumber. As a result, in the sense of the Beer-Lambert law, d is a function of the position within a spectrum. However, as this effect can be calculated, acquired spectra can be corrected in order to compensate this effect.

In addition, IR based techniques are especially powerful when being combined with complementary methods like Kelvin Probe microscopy [86,87] or quartz crystal microbalance analysis. The latter, rather novel approach, will be discussed in great detail in section 4.1 as this particular combination represents one of the core experiments performed for this thesis.

In the context of the investigation of humidity related systems, FT-IR-spectroscopy in reflection mode represents a well-established tool for the analysis of water adsorption on a great variety of surfaces. E.g. Asay et al. [43] investigated the evolution of the water layer structure on silicon oxide. They found that at lower relative humidity the water structure was dominated by the so called “ice-like” structure whereas for higher relative humidity values the “liquid-like” water structure was preferred. In another study reported by Giner et al. [88] the influence of a plasma modification of aluminum surfaces on the water adsorption was investigated by means of in situ PM-IRRAS combined with QCM. It was found that the amount of adsorbed water varied with the degree of surface hydroxylation. Moreover, the diffusion of water through protecting surface coatings and barrier-film properties of these layers are of crucial interest in the case of corrosion protection for engineering materials [86,89]. Liu et al. [90] studied the barrier properties of ultra-thin $SiO_x$ plasma polymer layers towards water penetration using DPM-FT-IRRAS to characterize the water uptake. In addition to the studies on water adsorption and barrier penetration, more fundamental studies have focused on the structure of water and the properties of the formed hydrogen bond-network mostly by means of FT-IR and the related Raman spectroscopy techniques. [91,92] In their comprehensive work, Chumaevskii et al. [91] investigated the shape of the Raman peak of liquid water with different salts and deconvoluted it with respect to the different conformers of water in the network. Moreover, they argued that the two bonds of the water molecule were not equal and behaved as independent oscillators.

### 2.6.4. Quartz crystal microbalance analysis

The determination of masses is one of the oldest techniques employed my mankind. However, with the rise of nanotechnology, the weighing of very small masses became increasingly important for many applications. Although, quartz crystal microbalance (QCM) analysis was not developed by a single individual, this technique is commonly attributed to the pioneering work of Sauerbrey as he realized a linear behavior between the shift of resonance frequency and attached mass. Therefore he was the first to report the use of a QCM in sensing mode [93] enabling him to determine the masses of thin films deposited on the opposing sides of a resonator.

However, as the technique is based on the piezoelectric effect, the first steps for the development of this powerful technique date back to the 1880 when Jacques and Pierre Curie reported that a pressure employed on quartz samples resulted in an electric charging [94]. Today, this effect is fully understood and explained by means of the formation of a dipole moment in every elemental cell of a crystal lattice when exposed to a uniaxial load. This behavior stems from the displacement of the otherwise superimposed centers of negative and positive charge as depicted in Figure 24.

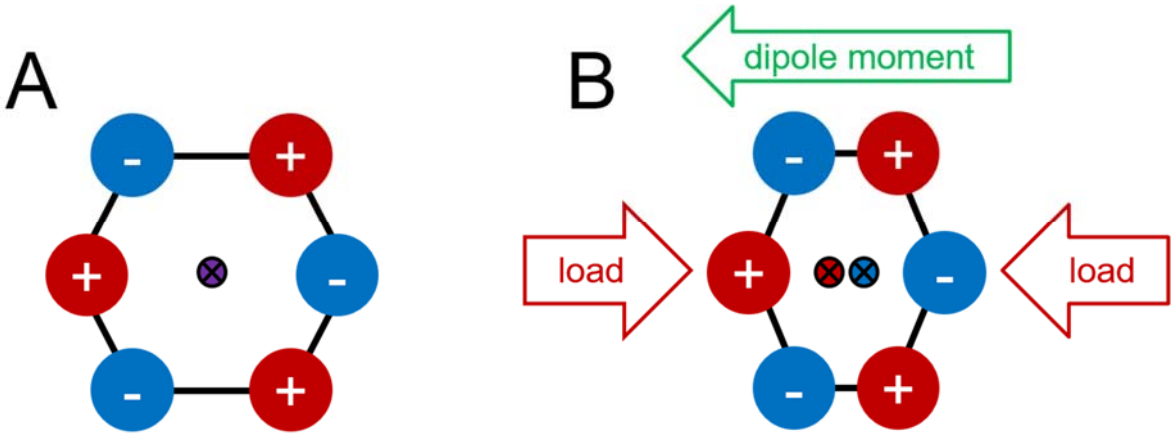


*Figure 24: Principle of the piezoelectric effect. During the relaxed state (A) the center of negative and positive charge are superimposed effectively counterbalancing themselves resulting in an overall neutral lattice. When a uniaxial force is exerted the two centers of charge move towards opposing directions resulting in a dipole moment.*

As a result, on a macroscopic scale, the sum of all elementary cell dipole moments can be measured as a charging of the deformed material. Typically, this effect is fully reversible and even an inverse piezoelectric effect can be found where the application of an electric charge to a piezoelectric material results in a corresponding mechanical deformation. In fact, the inverse piezoelectric effect is used for the QCM measurement as the crystal is attenuated by an

external alternating current employed to metal electrodes deposited on the crystals surface (Figure 25). Similar to other resonators, the quartz-crystal features a characteristic resonance frequency which changes proportional to the mass attached to the crystals surface.

*Figure 25: Photograph of the front (left) and back (right) of a typical 1 inch AT-cut QCM crystal with a resonance frequency of 5 MHz featuring a back electrode that is considerably smaller than the front electrode.*

Typically, there are three quite distinct approaches on how to drive and monitor a QCM crystal during an experiment.

In the simplest approach the crystal is driven by an oscillator circuit attached to an operational amplifier driving the crystal with its resonance frequency. Although, this setup is unparalleled when it comes to stability of the oscillation, it is very limited in the sense of information the user can obtain from the experiment as this setup allows only for the observation of one single frequency. Moreover, most setups do not allow for dissipation analysis (discussed later in this section) which often gives valuable insights in addition to the classic observation of mass changes. However, in contrast to the more sophisticated experimental setups this method is typically very simple and thus cheap.

In comparison to the previous mode of operation the resonance frequency can also be monitored by means of impedance analysis. For this, the crystal is attached to an impedance analyzer which sweeps the driving frequency through a small interval. In case of the driving frequency equaling the resonance frequency of the crystal, the actual amplitude of the crystal features a maximum. However, as the amplitude is very small it cannot be measured directly. Instead, the conductance of the crystal is being monitored which also exhibits a maximum in case of resonance conditions. The curve describing the conductance of a crystal as a function of the driving frequency is called the resonance curve (Figure 26). By employing peak fitting of the measured curve with a theoretical curve, both the resonance frequency and the so called bandwidth or half-band-half-width ($\Gamma$) are determined.

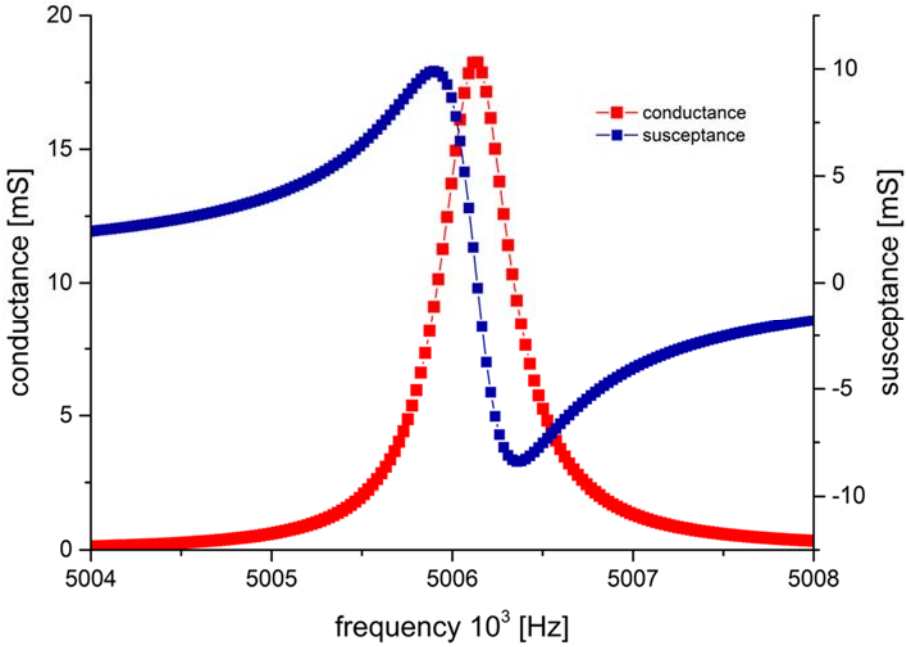


*Figure 26: Typical resonance curve of a 5 MHz crystal as depicted in Figure 25. The read curve depicts the impedance spectrum whereas the blue curve indicated the susceptance.*

In addition, the subsequent monitoring of multiple higher harmonics is possible making this method much more versatile and robust. In this context it has to be noted that different overtones feature distinct susceptibilities towards environmental factors making it desirable to monitor multiple for better reliability of the overall experiment. Moreover, the comparison of frequency shifts of different overtones throughout an experiment can provide further insides to the mechanical properties of the attached masses.

The last technique typically employed for the QCM is the so called ring-down method. This technique uses a strong pulse, featuring the resonance frequency of the quartz, to briefly excite the crystal. The actual measurement however is performed by monitoring the decay of the resonators oscillation. This free decay curve (Figure 27) is then processed via Fourier transform leading to the earlier mentioned resonance curves.

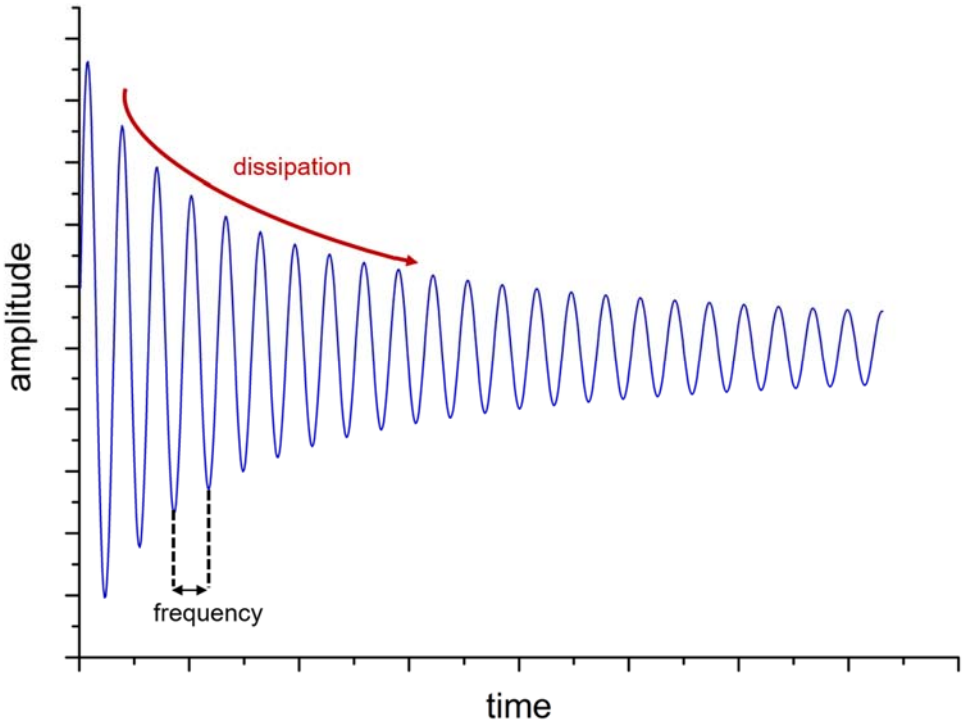


*Figure 27: Simulated ring down curve. The oscillation frequency is given by the wavelength whereas the dampening indicates the dissipation.*

When compared to the impedance based approach, this method has numerous advantages mostly stemming from the fact that it does not operate in the frequency domain but in the time domain instead. Hence, processes occurring within the timeframe comparable to the acquisition time of a single impedance spectrum are clearly observable during the ring down whereas they would render corresponding impedance spectrum unanalyzable. Moreover, much higher sampling rates are accessible as the acquisition time for a single ring-down is comparable to the bandwidth of the resonance peak which typically is much shorter than the time necessary for a single impedance spectrum. In addition, in the case of nonlinear effects induced either by the sample or by the quartz, the analysis of the time dependent change in frequency during a ring-down (chrip) can lead to the determination of these nonlinearities.

However, the impedance as well as the ring-down based techniques suffer from a worse repeatability when compared to the oscillator circuits as both do not drive the crystal permanently rather than in short intervals, resulting in small variations of the crystals temperature.

The key to the actual measurement of mass changes for all three methods is based on the linear proportionality between the resonance frequency and the change in mass. This dependency is presented in equation (2.33) and is commonly referred as the Sauerbrey equation [93].

$$\Delta f = -\frac{2 f_0^2}{A\sqrt{\mu\rho}}\Delta m \tag{2.33}$$

Typically, all fix factors like the base resonance frequency ($f_0$), the density of the resonator material ($\rho$) and the shear modulus of the resonator material ($\mu$) are combined to a constant (c) in order to simplify the everyday use during measurements.

$$\Delta m = -c \cdot \Delta f \tag{2.34}$$

In addition, as the active area (A) is not always known, the mass changes are often referred as specific mass changes in mass/area. E.g. for a typical AT-cut quartz resonator c is found to be 17.7 ng·Hz$^{-1}$·cm$^{-2}$ and 44.2 ng·Hz$^{-1}$·cm$^{-2}$ for 5 MHz and 10 MHz crystals, respectively. From this values it can be easily seen that the sensitivity of this method is around three orders of magnitude better than any conventional balance system found in modern labs which stems from the unparalleled accuracy frequencies can be measured with (typical noise <<1 Hz). As a result, it is easily possible to determine the mass of a single monolayer of organic molecules when being adsorbed to the crystal surface. For this reason, the QCM is also referred to as the quartz crystal nanobalance.

Importantly, the applicability of equation (2.33) depends on certain boundary conditions. In fact, the mass attached to the crystal has to be stiff and elastic in nature meaning that the attached mass oscillates with the exact same frequency and lateral displacement as the crystal resulting in no energy loss. Additionally, the equation is limited by the so called small mass approximation, restricting the accessible mass changes to approximately 2% of the crystals mass. Fortunately, for most applications the latter of the two limitations is of no relevance for typical experiments. On the contrary, very often the mass attached to the crystal is not fully elastic but also bears a certain inelastic load resulting in a loss of energy. This effect can be detected by suitable experimental setups in the form of the so called dissipation (D). In this context D is defined as the loss of energy per cycle divided by the total energy of the system.

In the case of an experiment using the earlier mentioned impedance analysis, the dissipation can be calculated from the resonance spectrum according to equation (2.35) as it equals the bandwidth divided by the corresponding resonance frequency.

$$D = \frac{2\Gamma}{f} \tag{2.35}$$

In contrast to that, employing the ring-down method, the dissipation is directly given by the free decay curve as presented in Figure 27. Although strictly speaking the Sauerbrey equation does not hold true for a system featuring any sort of dissipation, the energy loss itself bears valuable information on the viscosity and adhesion properties of the attached material.

Nowadays the QCM is a ubiquitous tools found in various applications ranging from the measurements of the adsorption of molecules from a gaseous or liquid phase onto a surface or the study of drug delivery mechanisms in biochemistry to a vast amount of applications in the field of material sciences. In more recent times however, QCM has frequently been employed for the study of granular systems. E.g. Johannsmann et al. studied the hysteretic behavior of the contact stiffening of particles immobilized on a resonator surface [95,96] with respect to cycles of relative humidity. Moreover, the same group [95] could follow the transition from elastic to inertial loading as predicted by the Dybwad model. [97] During their experiment, they wetted a layer of 100 µm sized spheres on a torsional resonator and measured the frequency shift and the dissipation while the sample was slowly drying. It was found that the dissipation exhibited a local maximum during the drying process, attributed to the transition from the Dybwad state (weak contact) to the Sauerbrey state (strong contact). Moreover, they explained the change in contact force as a consequence of the drying process which induced the formation of capillaries. As a result, the force between the particles and the substrate increased continuously as the sample dried resulting in the transition from elastic to inertial loading.

Focusing on the particle adsorption onto quartz crystal surfaces, Pomorska et al. [98] studied the adsorption of mesoporous $TiO_2$ nano containers modified with polyelectrolyte layers on SAM modified quartz crystals. They found an interesting effect resulting in a positive frequency shift of the resonator during the adsorption of micrometer sized objects from solution [99]. Besides the various applications of the QCM as a standalone technique, one of the main advantages however is based on the ability to employ it as a complimentary, or even, combined technique as the specific requirements for an experimental QCM setup are rather basic, rendering the implementation simple for many experimental setups.

### 2.6.5. AFM based methods for the analysis of contact forces

Whenever forces in the pico-newton (pN) or nano-newton (nN) regime have to be directly measured, atomic force microscope (AFM) based techniques have proved to be a powerful and almost unparalleled tool. The development dates back to 1980's where Binning and Rohre developed the first scanning tunneling microscope (STM) [100] and thereby set the foundation for all modern scanning probe microscopy (SPM) techniques. Unlike any other microscopy technique, during a typical SPM experiment the surface is scanned line by line using a nanoscale probe. Hence this method is not limited by any interference effects known from methods employing electromagnetic radiation to probe surfaces. As a result, experiments with atomic or even subatomic [101] resolutions are achievable.

In the case of STM, the tunnel current between a conductive tip and the specimen surface is kept constant at all times by means of vertical movement of the probe. As the tunnel current has a strong dependency of the tip surface distance, the vertical movement of the tip necessary to keep the current constant mimics the surface topography. However, it is crucial to keep in mind that this method does not directly measure the topography. In fact, a local change in sample conductivity for instance will inevitably be misinterpreted as a topographical change due to the nature of the method.

Only few years after this groundbreaking development the atomic force microscope was developed by Gerber, Binning and Quate [102]. In contrast to STM, this method does not depend on the conductivity of the specimen. For surface imaging purposes, the surface is mechanically probed by a sharp tip mounted on a cantilever (Figure 28) which is scanned over the surface.

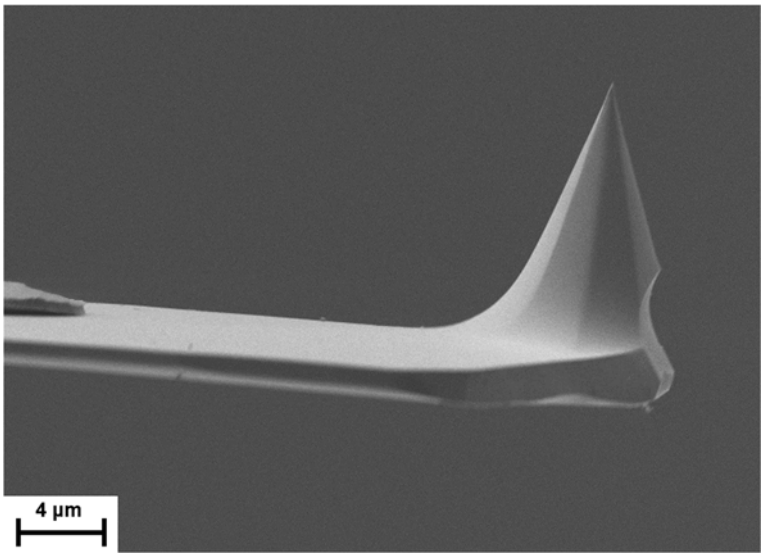


*Figure 28: FE-SEM image of a typical silicon based AFM cantilever with tip.*

As a result of the mechanical interaction between topographical features on the surface and the tip, the lever gets deflected. This defection is commonly detected by an optical method using a laser beam which is reflected from the backside of the cantilever and subsequently analyzed by a position sensitive detector (Figure 29). Most detectors employed in modern AFMs consist of four electrodes exhibiting an electric charge (U) proportional to the amount of incident light (Figure 29). Typically, the vertical ($D_{vertical}$) as well as the lateral ($D_{lateral}$) displacement is quantified according to equation (2.36) and (2.37), respectively.

$$D_{vertical} = \frac{(U_I + U_{II}) - (U_{III} + U_{IV})}{U_I + U_{II} + U_{III} + U_{IV}} \tag{2.36}$$

$$D_{horizontal} = \frac{(U_{II} + U_{IV}) - (U_I + U_{III})}{U_I + U_{II} + U_{III} + U_{IV}} \tag{2.37}$$

As the cantilever becomes deflected due to an interaction with a surface feature, the position of the reflected beam on the detector changes. In this context the vertical displacement of the laser beam is proportional to the lateral bending whereas the horizontal displacement is characteristic for the torsion of the cantilever and can be correlated to the friction between the tip and the sample. In analogy to the STM the probe is moved vertically until the topography induced deflection has been fully compensated. Hence, the amount of vertical movement can be directly correlated to the surface topography.

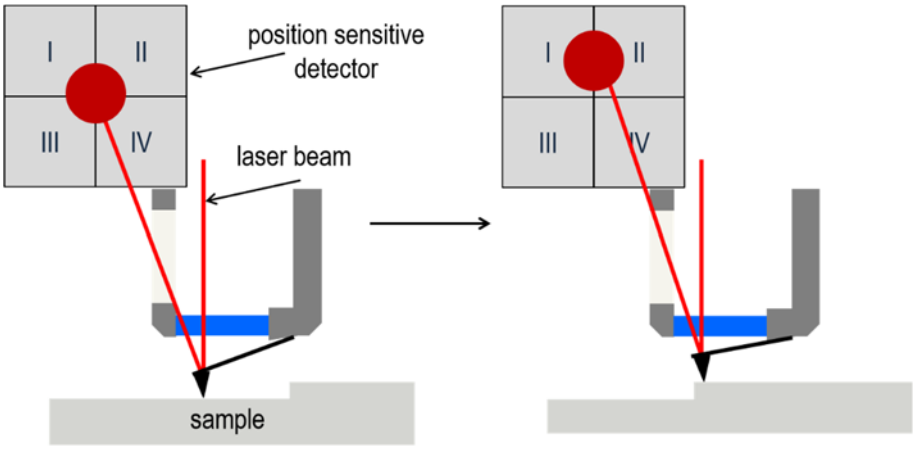


*Figure 29: Schematic of a surface topographical measurement with an AFM. As the tip interacts with the step edge the position of the reflected laser beam gets displaced. (Figure adopted from [103]).*

As the deflection is a direct consequence of a mechanical contact, the AFM does not suffer the STMs limitations mentioned earlier. For this reason, the AFM is found to be one of the very few techniques which enable the direct measurement of a sample topography on a nanometer scale.

Nowadays, the AFM is one of the most important analytical methods in surface science featuring an enormous variety of different measuring modes. Moreover, the AFM is not limited to pure imaging only. In fact, it can also be used to manipulate surfaces and molecules attached to surfaces. E.g. Torun, Özkaya and Grundmeier have shown that both AFM based nanografting and nanoshaving (Figure 30) have proved to be versatile tools for the study of formation and stability of self-assembled monolayers [104].

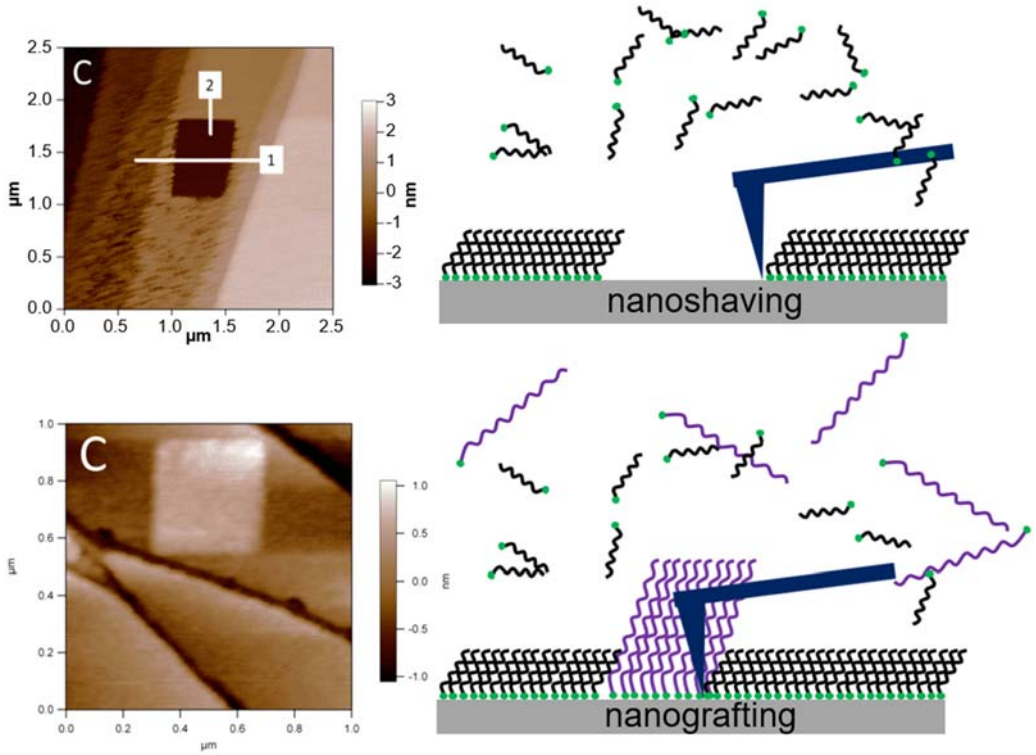


*Figure 30: Schematic of the nanografting and nanoshaving process employed for the study of SAMs by Torun, Özkaya and Grundmeier. Actual AFM footage has been adopted from [104]. The AFM topographical images show a nanoshaved patch on a hexyl-phosphonic acid (HPA) background monolayer situated on a $Al_2O_3$ (0001) single crystal surface (upper image). The lower figure shows and a nanografted patch using dodecyl-phosphonic acid on a similar substrate ($Al_2O_3$ (0001) with HPA).*

Beside the application of AFM in combination with liquid media as described above, also combined experiments using electrochemistry can be performed. E.g. Lammel, Torun and Grundmeier have employed AFM to follow the nucleation process during the metallization of carbon fiber reinforced polymers in an in-situ experiment (Figure 31) [105].

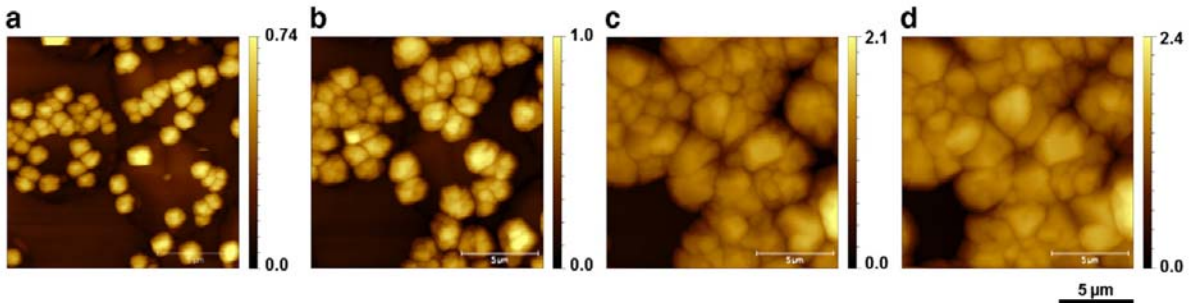


*Figure 31: AFM topographical measurements during the ongoing metallization of a carbon fiber reinforced polymer with increasing time from left to right. Picture has been adopted from [105].*

In addition to the imaging capabilities, the AFM also facilitates measurements of adhesion forces with an unparalleled local resolution. During a so called force distance experiment the probe is gradually brought into contact with the sample while the deflection of the laser is being monitored. As the tip gets close to the surface the so called snap-to contact can be

detected. This phenomenon mostly stems from the van der Waals interaction and is related to their high distance dependency. As the vdW interactions become strong enough to slightly bend the cantilever, the probe gets even closer to the sample which again results in an increase of vdW-force according to equation (2.7). As a consequence, the tip instantly "snaps" into contact with the sample (Figure 32-B).

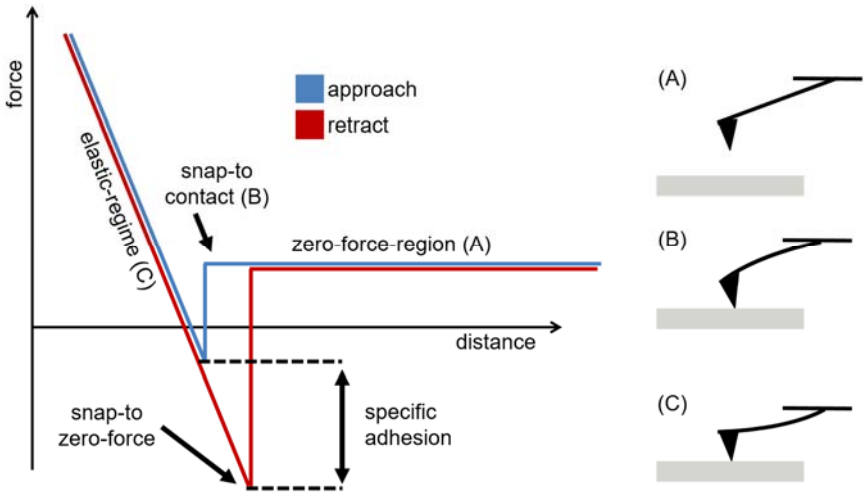


*Figure 32: Schematic of a typical curve acquired from an AFM based force distance experiment.*

Further approaching of the probe results in a linear bending of the cantilever proportional to the distance traveled by the probe according to Hook's law. When retracting the probe, a similar effect like the snap-to contact can be observed. Although, the cantilever is retracted past the point where it initially jumped to contact, it still remains on the surface. This is due to the specific adhesion force which holds the tip on the surface until the cantilevers spring force surpasses it and the cantilever jumps back to the zero-force regime. From the distance between the snap-to contact and snap-to zero-force the specific adhesion can be calculated. This technique has been further elaborated to the point where probes modified with long polymers featuring functional groups are used to probe specific interaction on different interfaces [106].

During a typical experiment multiple force distance curves are collected and evaluated for better statistical reliability. Most often, recorded data is presented either in the form of a histogram or boxplot (Figure 33). In both cases, all recorded force curves are analyzed with respect to the adhesion force. In the case of the histogram, these adhesion force values are sorted into smaller groups (bins) with each representing a certain force interval. Finally, the number of curves in each bin is plotted versus the mean force of the bin resulting in a histogram as presented in Figure 33.

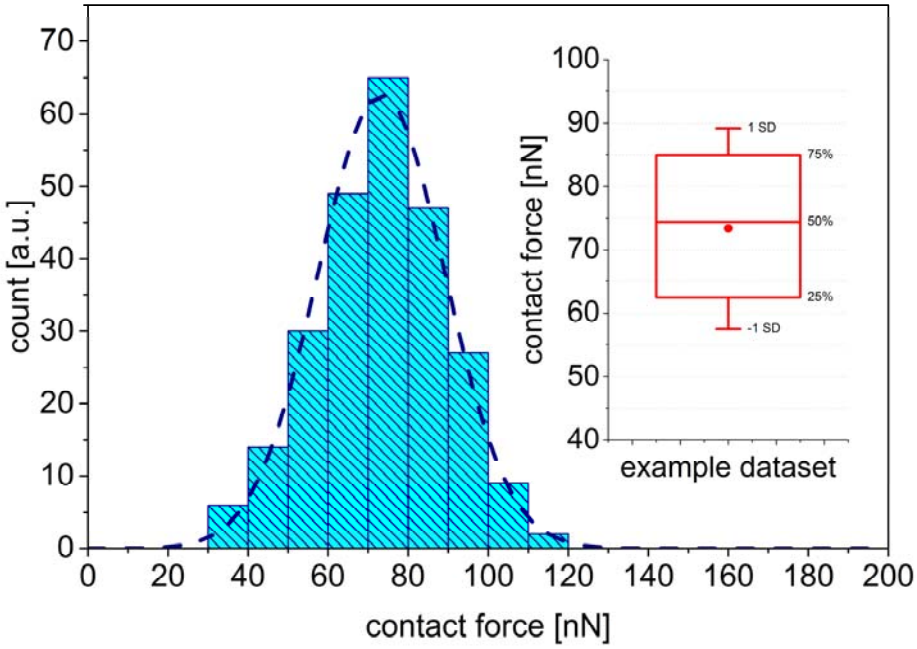


*Figure 33: Example for two typical presentations of AFM based force distance data. The main plot shows a contact force histogram. The small insert represents the corresponding boxplot.*

In the second type, all measured forces are initially sorted by their value. Subsequently this sequence is divided into four groups each containing 25% of the dataset. The box drawn covers the second and third groups representing the middle 50% of all force values measured. In addition, a horizontal line within the box represents the median value whereas the dot indicates the mean value. Moreover, the values laying within the standard deviation (SD) are indicated by the corresponding whiskers.

In the context of nanoparticles, force distance based techniques can be employed to directly measure particle surface interactions as the tip sample contact can be tuned to resemble a single particle wall contact as described in section 2.5. Moreover, due to the versatility of the AFM, studies under ambient condition can be performed as Kappl has recently presented [72]. Aside of these fundamental studies focusing on single particle contacts more recently Salameh and Mädler have shown that the AFM proofs to be valuable tool for the study of complex particle contacts with many particles involved [107] utilizing a combined SEM-AFM setup.

# 3. Experimental section

Chapter 3 contains a comprehensive summary of all sample preparation procedures employed within the scope of this thesis. Hence, both chapter 4 (QCM-D / FT-IR experiments) and chapter 5 (in-situ AFM based experiments) will refer back to procedures and treatments mentioned within this section. As a result, the structure of this chapter might not be evident when studied independently but should rather be read within the context of chapter 4 and 5.

The first two subsections of this chapter deal with the synthesis of $TiO_2$ nanoparticle (3.1) and experimental methods for the deposition of defined nanoparticle layers (3.2), respectively. In addition, section 3.3 will give an overview of the substrate pretreatment procedures, followed by section 3.4 presenting methods for the modification of particle surface chemistry. Finally section 3.5 provides a summary of the specific analytical devices and corresponding experimental parameters used within the scope of this thesis. Moreover, the procedures for the sample preparation in the context of each analytical methode are presented.

## 3.1. Synthesis of $TiO_2$ nanoparticles

$TiO_2$ nanospheres were prepared using a bottom-up approach. A reaction route via sol-gel synthesis, very similar to the method proposed by Tanaka et al. [29], was employed. Methanol and acetonitrile used as reaction solvent were of analytical grade and freshly dried prior to the reaction using a laboratory scale solvent dryer (Model: MB SPS-800, mBraun Intergas-Systeme GmbH, Garchingen, Germany). Titanium (IV) isopropoxide (TTIP) and Dodecyl-amine (DDA) were obtained from Sigma-Aldrich (Sigma-Adrich Chemie GmbH, Taufkirchen, Germany) and used without further purification. Ultra-pure water with a typical

conductivity of 0.055 µS $cm^{-1}$ was obtained from a water purification system (Model: Ultraclear TWF, SG Wasseraufbereitung, Barsbuettel, Germany).

Briefly, a solvent mixture of methanol (12 ml) and acetonitrile (3 ml) with water (30 µl) as hydrolyzing agent was prepared. In addition, DDA (28 mg) was dissolved acting as surface active species facilitating the formation of monodisperse spheres. Finally, the TTIP precursor (100 µl) was added to the solution for hydrolyzation and subsequent condensation reaction. It was found that the reaction mixture turned opaque about 30-60 seconds after the addition of TTIP indicating the initial formation of colloidal titania particles. The solution was stirred for 10-14 h. Received particle suspension was subsequently centrifuged (3000 rpm for 15 minutes) yielding a colorless solid. Further purification of the particle powder was performed by means of repetitive (min. 4x) dissolution of the solid material in fresh methanol followed by centrifugation effectively washing off remaining reaction residues. Finally, received particles were dried at for 2 h at 60 °C under ambient atmosphere. Particle size and morphology characterization was performed by means of FE-SEM imaging.

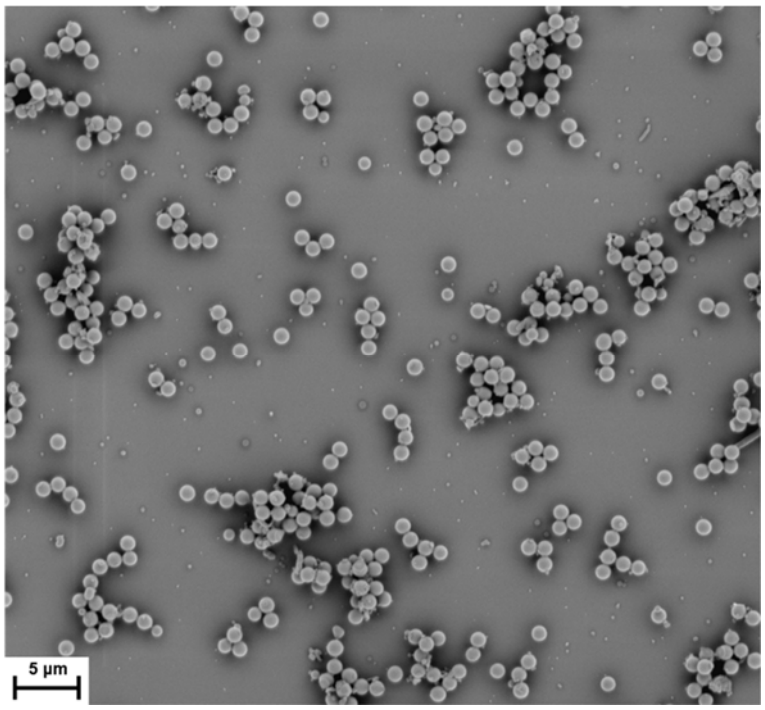


*Figure 34: FE-SEM image of titania particles after preparation and purification. Particles have been immobilized on a silicon wafer substrate.*

It was found that as prepared particles featured a typical diameter of ≈930 ±50 nm and a very narrow size distribution (Figure 34). Moreover, FE-SEM indicated the presence of mostly individual spheres leading to the conclusion that only a small fraction of the spheres merged during the hydrolysis forming multi-sphere aggregates. In order to trigger the transition from the as received amorphous to crystalline phase, particles were annealed at 400 °C for 5 h [29].

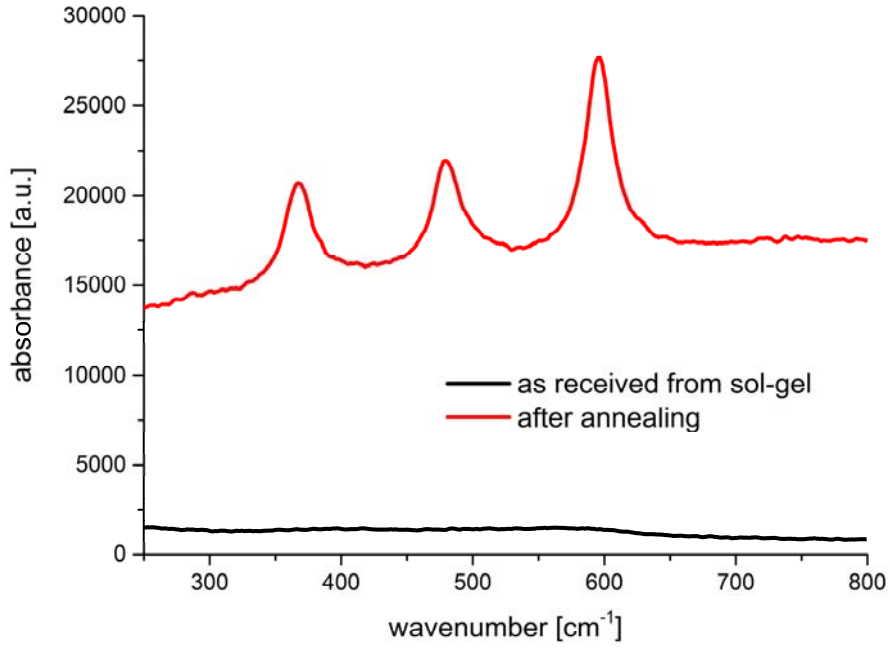


*Figure 35: Raman spectra of the as received and annealed $TiO_2$ particles prepared via sol-gel route. The three peaks in the red spectrum are characteristic for the anatase crystalline phase of $TiO_2$ [108].*

After the heat treatment, particles were in the anatase crystalline phase as indicated by the corresponding characteristic peaks in the Raman spectrum presented in Figure 35. Subsequently SEM analysis was performed in order to analyze the particles for thermally induced changes. It was found that aside of a minor shrinkage of the particle size due to a thermally induced crosslinking reaction, the particle morphology (fraction of agglomerates and polydispersity) was mostly unchanged after the annealing.

## 3.2. Techniques for the preparation of particle layers

### 3.2.1. Deposition of nanoparticles via sedimentation

The simplest technique employed for the deposition of nanoparticles on substrate surfaces was by mere sedimentation of the particles. However, for this process to work, the adhesion between the particle and the substrate was of outmost importance. As most often gold terminated substrates were used for their good performance as IR-mirrors, their very low adhesion properties had to be compensated. In the case of $SiO_2$ nanoparticles for instance, the substrate surfaces were covered with a thin $SiO_2$ film via PE-CVD first before particles were deposited. The different pretreatment processes for the substrates are described in great detail in section 3.3.

For the particle deposition, 100 µl of the nanoparticle suspension (50 $mg \cdot ml^{-1}$) was diluted in 50 ml ultra-pure water together with 16.5 µl of 37% hydrochloric acid followed by subsequent sonification for 15 minutes. At the resulting pH of about 2 the dispersion was no longer stable due to the high amount of ions in the liquid shielding the surface charge. Therefore, in the sense of DLVO theory, a sedimentation process started. Substrates were immersed in the nanoparticle suspension for 24 hours allowing the particles to sediment on the surface. However, as defined layers were desirable and this process yielded multilayers by nature, additional treatments were necessary to remove the excess particles. Substrates were carefully removed from the solution and dipped into ultra-pure water with an adjusted pH of 2 in order to remove excess particles. Finally, while holding the substrates upright, the sample was dried in a gentle stream of nitrogen starting from the upper side slowly moving the drying front down the sample. This procedure typically yielded a sample with 0.8 to 1.7 monolayers of particles, mostly in a hexagonal close packing as indicated by FE-SEM analysis (corresponding SEM data is presented in chapter 4.3.2 Figure 55 and Figure 56). Furthermore, all samples were also checked for contaminations by means of XPS.

### 3.2.2. Deposition of nanoparticles via electrophoresis

In the case of experiments where the conditioning of the substrate for increased particle adhesion was not possible, alternative techniques for the deposition had to be employed as the mere deposition via sedimentation typically did not yield the desired coverage on gold substrates. For this reason, electrophoretic deposition was employed for nanoparticle film deposition on gold covered silicon wafer or quartz crystal substrates. The experimental conditions regarding solvent, particle concentration and potential applied were carefully chosen for optimal particle surface coverage. For a typical electrophoretic deposition, 50 mg of particles were dissolved in 25 ml of isopropanol/acetone/water (5/1/0.2 v/v ratio). Few droplets of pure nitric acid were added to facilitate the charging of the particles in solution which was crucial for the electrophoresis process. Subsequently, the solution was sonicated for 10 minutes prior to use. Electrodes used as cathode and anode were immersed into the particle suspension at a fixed distance of 1 cm (Figure 36-A). The optimal deposition voltage was found to be 25 V. During the electrophoretic deposition the particle suspension was continuously stirred in order to avoid diffusion controlled effects. After 15 minutes, gold electrodes were removed from the solution and carefully dried with a gentle stream of dry nitrogen and particle film morphology was subsequently analyzed by means of FE-SEM (Figure 36-B).

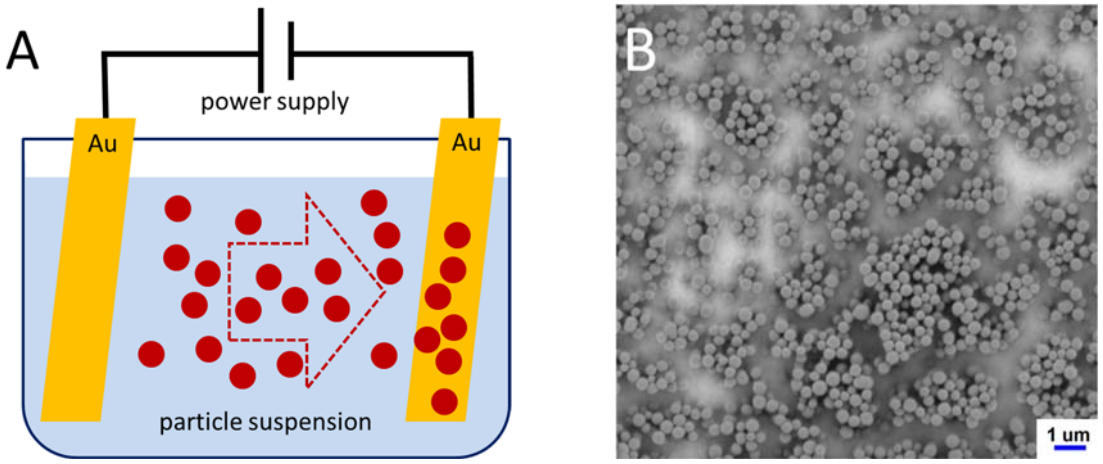


*Figure 36: Schematic of the experimental setup for the electrophoretic deposition of nanoparticles (A). FE-SEM image of a deposited layer of $TiO_2$ nanoparticles on an Au covered Si wafer substrate (B).*

It was found that the particles covered approximately 70% of the surface area. However, this process led to a considerable amount of agglomeration forming larger aggregates and partial multilayers on the surface.

### 3.2.3. Deposition of nanoparticles via template method

To achieve ultra-smooth nanoparticle ensemble surfaces, a novel preparation method was developed inspired by the Mica based template stripping commonly employed for the preparation of ultra-smooth Au substrates. The corresponding process is schematically depicted in Figure 37. Initially, drop of the nanoparticle suspension was allowed to dry overnight on an ultra-smooth Mica template stripped Au surface.

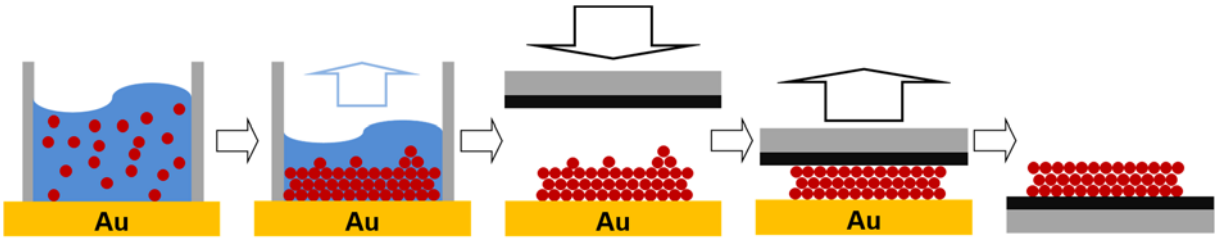


*Figure 37: Schematic process for preparation of ultra-smooth particle surfaces via template stripping method.*

Subsequently, the dry particle multilayer was covered with an adhesive substrate mounted on a metal sample holder and subsequently compressed. Peeling-off the sample holder the particles stuck to the adhesive substrate due to the low specific adhesion on the Au surface exposing the Au-particle interface.

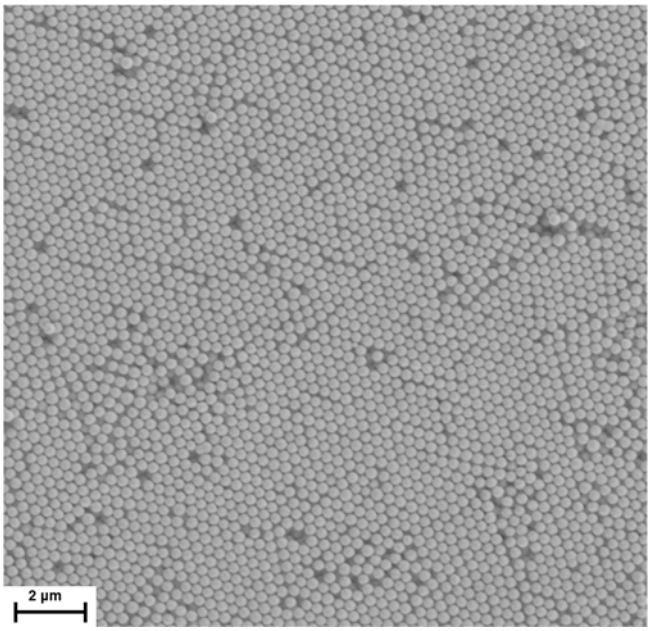


*Figure 38: FE-SEM image of peeled $SiO_2$ nanoparticle layer.*

Subsequent FE-SEM characterization (Figure 38) revealed a smooth particle interface consisting of large domains of hexagonal closest packed particles with few defects. The main advantage of this method in comparison to the other proposed techniques stemmed from its extraordinary simplicity compared to the other methods presented in this chapter.

### 3.2.4. Preparation of nanoparticle layers via Langmuir Blodgett technique

Langmuir Blodgett film technique was employed for the $TiO_2$ particle layer preparation as proposed by McNamee et al. [109]. In contrast to the methods previously discussed for $TiO_2$ particles, this technique allowed for the direct preparation of densely packed mono and multilayers (multiple up and down strokes) resulting in much more defined particle layers.

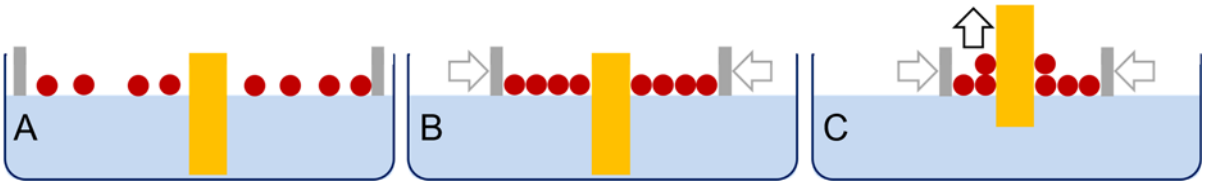


*Figure 39: Schematic of the Langmuir Blodgett technique employed for the preparation of nanoparticle layers.*

$TiO_2$ nanoparticles were dissolved in chloroform and subsequently spread onto an aqueous sub-phase with an adjusted pH of 2. Since the $TiO_2$ nanoparticles were positively charged at pH 2, they accumulated at the air/water interface (Figure 39-A). In a next step, two mobile barriers reduced the area available to the nanoparticles (Figure 39-B) compressing the two-dimensional particle layer. The packing density of the nanoparticle layer was continuously followed by means of surface pressure measurements (Wilhelmy plate) until a densely packed monolayer was formed. Finally, the previously immersed substrate was pulled out of the sub-phase transferring the particles on to it (Figure 39-C) while maintaining a constant surface pressure by continuously movement of the mobile barriers.

## 3.3. Substrate preparation

### 3.3.1. Substrate cleaning

In order to remove organic contaminations, quartz crystal and Si-wafer substrates were cleaned by means of a mixture of 1:1 of 30% aqueous $NH_3$ and 30% aqueous $H_2O_2$ (Caution: this mixture is extremely corrosive). The solution was heated to 70 °C and substrates were immersed for approximately 1 to 2 hours followed by extensive rinsing with ultra-pure water and ethanol. Finally, substrates were dried in a gentle stream of nitrogen.

### 3.3.2. Surface modification via self-assembled monolayer adsorption

Preparation of organized functional monolayers was performed via solution self-assembly route utilizing the well-established gold-thiol chemistry (Figure 40). Typically, a long chain aliphatic thiol terminated surfactant was dissolved in ethanol with concentrations in the regime of 1 $mM \cdot l^{-1}$. Solutions were ultrasonicated to ensure the full dissolution of the surfactant molecule. Subsequently, after being immersed for 12 to 24 hours, substrates were removed from the solution and rinsed with pure ethanol in order to remove any excess molecules.

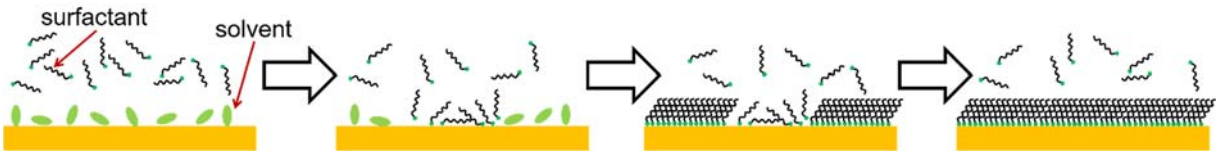


*Figure 40: Schematic of adsorption and SAM formation process on the substrate surface. The initially cleaned substrate is immediately covered with loosely bound solvent molecules. At the beginning of the process these solvent molecules are replaced by the surfactant species due to the much stronger interaction force. With increasing immersion time and driven by the van der Waals interaction, the initially laying down aliphatic chains tent to stand up forming a closely packed layer of a highly ordered film.*

Finally, rinsed substrates were dried in a gentle stream of dry nitrogen. Successful adsorption of the self-assembled monolayers was analyzed via static water contact angle measurements as well as FT-IR spectroscopy.

### 3.3.3. Deposition of thin films for substrate conditioning via PE-CVD route

Substrates were coated via plasma enhanced chemical vapor deposition (PE-CVD) with a thin layer of a $SiO_2$ plasma polymer using hexamethyldisiloxane (HDMSO) as a precursor. Preparation was performed in an improved version of the bell jar reactor originally designed by Grundmeier et al. [110] featuring an parallel electrode layout. Briefly, the experimental setup allowed for the mixture of two process gasses with defined ratios using mass flow controllers. Moreover, a precursor molecule could be dosed to the plasma chamber. Overall reactor pressure was monitored using a gas-species independent pressure gauge.

Deposition was performed using a gas composition with a high $O_2$ excess with respect to the precursor to ensure the formation of an inorganic glass-like film. Initially, Ar was supplied to the plasma cell at a flow rate of 0.9 ml·min$^{-1}$ and the pumping rate was adjusted to establish a stable pressure of 0.15 mbar within the camber. Then, $O_2$ was dosed until the total pressure reached 0.3 mbar. Finally, HMDSO was added increasing the pressure for additional 0.005 mbar and subsequently the plasma (500 V, 4 mA, 4 kHz) was ignited. Depositions process and layer thickness was continuously monitored using a custom designed sample holder (Figure 41) allowing for QCM measurements during ongoing deposition.

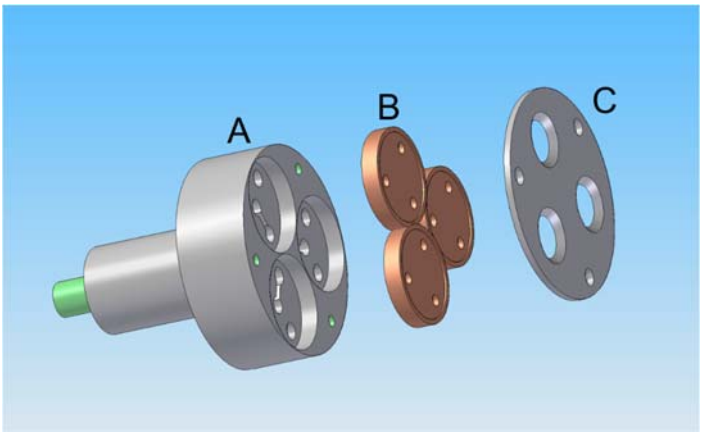


*Figure 41: Schematic of the custom designed sample holder allowing for the simultaneous coating of three 1-inch crystal substrates. Holder base A and lid C are made from aluminum whereas the three inner crystal holders B are carved from PTFE to ensure the for the measurement imperative electrical insulation of the QCM crystals backside electrode. QCM crystal electrodes are contacted via uniaxial spring-loaded pins.*

Surface chemistry of the deposited thin $SiO_2$ layers was analyzed by means of XPS and complementary FT-IR. Moreover, film morphology was characterized by means of FE-SEM and AFM. Corresponding results are presented in section 4.3.1.

## 3.4. Modification of particle and substrate interfaces

### 3.4.1. Chemical modification of particle surfaces via CVD route

Chemical vapor deposition (CVD) was performed in a two-stepped process. Initially the sample was placed in a PTFE-beaker together with ≈30 µl of the organosilane (Figure 42-left). Afterwards, the vessel was tightly closed and heated up to ≈130 °C. In case of an organosilane with an extraordinary high boiling point the temperature for the first step was changed accordingly. The closed reactor was heated for 2 h to ensure a thorough coating of the sample. For the second step, the sample was removed from the vessel and heated up to ≈180 °C for 2 h facilitating the crosslinking of the organosilane layer.

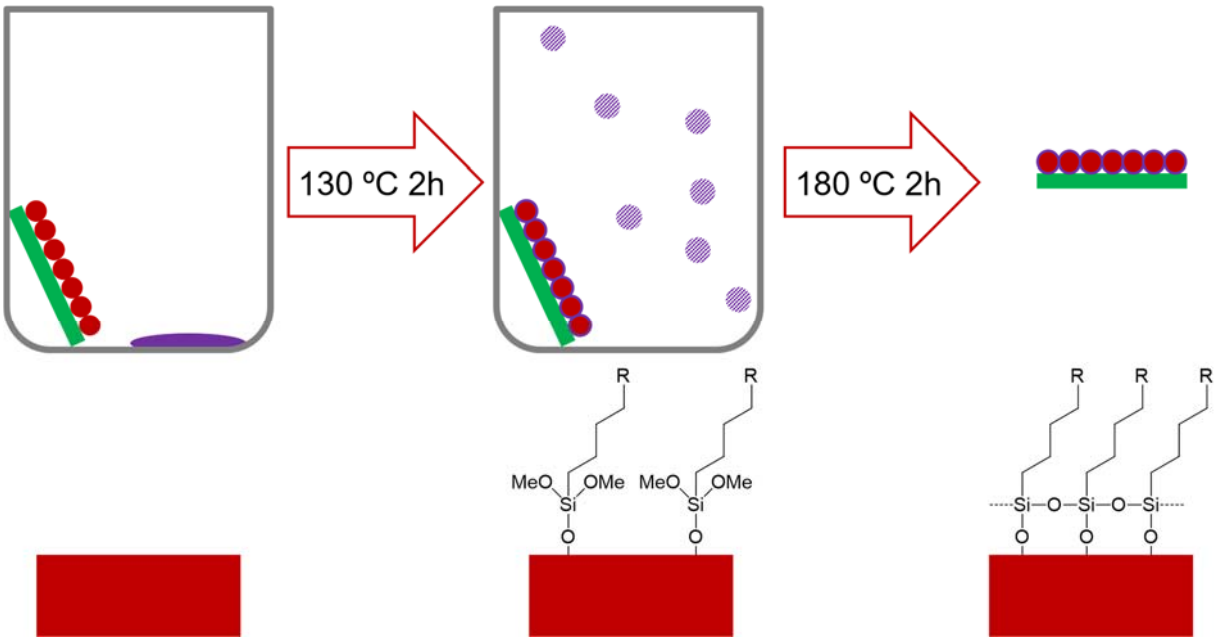


*Figure 42: Schematic of the two-stepped CVD process. Temperatures presented are subject to variation in accordance with the boiling point of the organosilane used.*

Typically, a broad range of organosilanes can be utilized for this process opening up a huge variety of possible surface modification. Examples of the organosilane used were perflouro-octyl-triethoxy-silane or dodecyl-trimethoxy-silane. In addition to the tridentate molecules also bi-dentate and mono-dentate species were employed. With respect to the leaving group, halogen organosilanes were avoided in favor of methoxy groups due to the highly corrosive nature of the resulting side products.

### 3.4.2. ALD based coating of surfaces with $TiO_2$

Both substrate and AFM cantilevers have been coated by means of atomic layer deposition, using a novel precursor material. Depositions were performed at our collaborating institute in Bochum at the chair of Prof. Dr. Anjana Devi by Mr. Maximilian Gebhard (Ruhr-Universität Bochum, Germany). Specific experimental details and through characterization of these layers have recently been published in Materials Chemistry C within the scope of a collaborative paper [111].

### 3.4.3. Modification of $TiO_2$ surface chemistry by means of UV-light irradiation

For the modification of particle surfaces via UV-light, samples were illuminated using a polychromatic Hg-bulb based UV-light source (Model: Omnicure S2000, Excelitas Technologies, Asslar, Germany) equipped with a liquid filled fiber optic. Irradiation energy was controlled by means of an iris aperture and was calibrated using an UV-light radiometer (Model: Omnicure R2000 Radiometer, Excelitas Technologies, Asslar, Germany).

## 3.5. Analytical and spectroscopic methods

### 3.5.1. Scanning electron microscopy

During typical experiments, the particle material was immobilized on a conductive substrate to limit unwanted charging. Although a metal substrate, with its superior conductivity properties was preferable for the immobilization of the particles, the lacking adhesion of particle material made the application often problematic and less appealing compared to the widely adopted adhesive covered "carbon-pads" (Figure 43). For this reason, a metal substrate was only chosen when charging was found to be a problem during the measurements. An alternative method for the immobilization which could also be employed for SEM analysis is described in section 3.5.2.

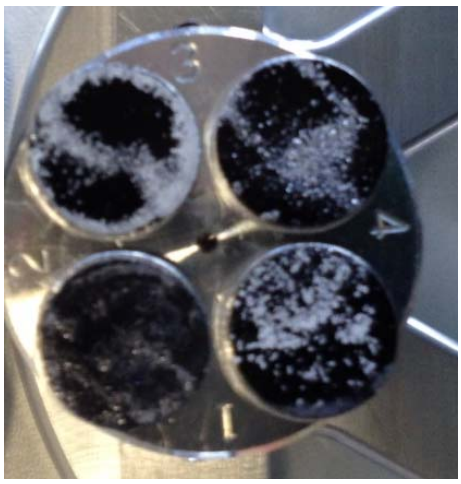

*Figure 43: Four different particle samples immobilized on sticky carbon tapes. The carbon pad is dipped in the particle powered and excess particles are removed by means of blowing with a stream of nitrogen. The actual corresponding SEM images are depicted in Figure 4.*

If not stated otherwise all SEM images presented in this thesis have been acquired using an Agilent 8500 field emitter electron microscope (Model: Agilent 8500 FE-SEM, Keysight Technologies, Böblingen, Germany) operated with an acceleration energy of 1000 eV.

### 3.5.2. X-ray photoelectron spectroscopy

In order to prepare a nanoparticle sample for XPS analysis, a small particle ensembles was pressed into an indium matrix as depicted in Figure 44. Initially a small amount of the particle powder was placed on a clean substrate. For this purpose, aluminum foil was found to be suitable as it is very clean and readily available. Next, a small piece of solvent cleaned indium foil (typical thickness of 250 µm) was placed on the particle powder. Then the whole stack was compressed in order to imprint the particles into the ductile indium matrix. Finally, the two foils were separated again and the substrate was blown with a strong stream of nitrogen to remove loosely bound excess particles.

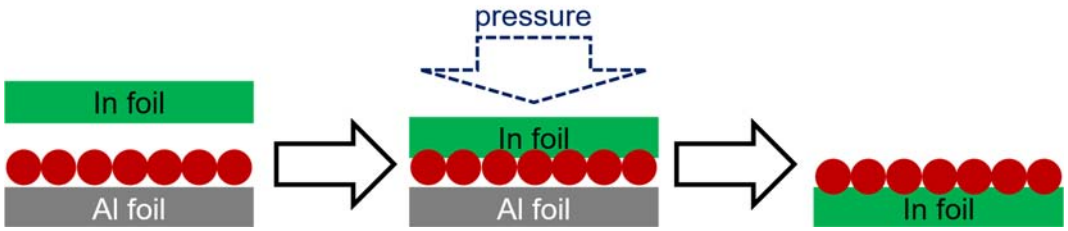


*Figure 44: Schematic of the process for the immobilization of particles for XPS analysis using an indium foil.*

If not stated otherwise XPS data presented within this thesis has been acquired using an monochromated Al kα source with an excitation energy of 1486.7 eV operated at an output power of 300 W. Photoelectrons were detected on a 128 channel plate detector (Model: Omicron-Argus, Omicron Nanotechnology, Taunusstein, Germany) after passing a hemispherical electron energy analyzer at an angle of 30° with respect to the surface normal. In order to balance the number of sweeps necessary for a satisfying signal to noise ratio with a desired energy resolution, the pass energy had been set to 50 eV and 10 eV for survey spectra and detailed spectra, respectively. Samples featuring charging due to poor electron conductivity have been neutralized by means of a charge neutralizer (Model: Omicron CN10) using the C 1s peak a 284.5 eV as internal reference.

### 3.5.3. Fourier transform infrared spectroscopy

If not stated otherwise, presented FT-IR data was acquired using a Bruker Vertex 70 FT-IR spectrometer equipped with a liquid nitrogen cooled mercury-cadmium-telluride (MCT) detector using a spectral resolution of 4 $cm^{-1}$. For improved signal to noise ratio typically 512 spectra have been averaged.

### 3.5.4. Quartz crystal microbalance analysis

QCM data has been acquired using a Saunders SA250 π-network analyzer for impedance measurements in combination with the software package QTZ provided by the group of Prof. Dr. Johannsmann (TU Clausthal, Germany). Details regarding the sample preparation are provided within section 4.

### 3.5.5. AFM based methods for the analysis of contact forces

AFM data presented in this thesis has been acquired using an Agilent 5500 Atomic Force Microscope equipped with a vibration isolating system positioned in a noise reducing box. Force calibration of the AFM was performed with each cantilever using a thermal noise based method (Agilent Thermal K) for the determination of the individual force constants. Corresponding deflection sensitivities were determined from the slope of the approach curve in the elastic regime (Figure 32).

### 3.5.6. Determination of specific surface area of nanoparticle powder

Measurements of the specific surface area have been performed at the chair of Prof. Dr. Tiemann (University of Paderborn, Germany) by Mr. Dominik Klaus. Therefore, the procedure will only be described briefly.

Particle surface area determination was performed by means of the BET method using an Autosorb-6B (Quantachrome, Odelzhausen, Germany). As received nanoparticle suspension was dried under vacuum conditions. Subsequently, received particle powder was heated to 120 °C for 12 h under vacuum conditions to remove residual water. Adsorbed nitrogen volume was measured for every $p/p_0$ with a step size of 0.02 up to a maximum of 0.99. Subsequently, the specific surface area was derived from the first five points of the isotherm adsorption branch by the BET-method.

# 4. In-situ analysis of capillary bridge formation via combined QCM-D / FT-IR

Results and figures presented in this chapter have partially been published in the journal of Physical Chemistry Chemical Physics (PCCP) [112] and are presented in agreement with the editorial office.

Within this chapter, a detailed study of the complex interplay between the water adsorption on defined nanoparticle layers and their surface chemistry is being presented. In particular, $SiO_2$ and $TiO_2$ particles were in focus as both material systems feature appropriate characteristics for serving as a model system in addition to their relevancy for modern applications. Key experiment presented in this section was the combined QCM-D / FT-IR based analysis of water adsorption in humid environments (section 4.4) and corresponding changes upon surface chemistry modifications by means of UV-light (section 4.5.2) as well as chemical vapor deposition (section 4.5.1), respectively.

## 4.1. Scientific approach

Experiments presented in this chapter focused on the study of small particle ensemble with the basic idea of the direct correlation of QCM data with spectroscopic analysis of the particle surfaces via FT-IR. On the one hand, the QCM gave insight towards the amount of water being adsorbed on the particles and changes in mechanical properties of the particle substrate contact, whereas on the other hand, FT-IR gave valuable information regarding the structure of the adsorbed water molecules and the overall composition of this rather complex system.

Planned experiments consisted of the stepwise dosing of humidity to a small particle ensemble immobilized on a quartz crystal substrate mounted in a new experimental setup specifically developed for these experiments (Figure 45). Mentioned custom made cell facilitated experiments under controlled conditions and allowed for simultaneous QCM-D and FT-IR measurements. Details regarding the development of the experimental setup will be discussed in the subsequent chapter 4.2.

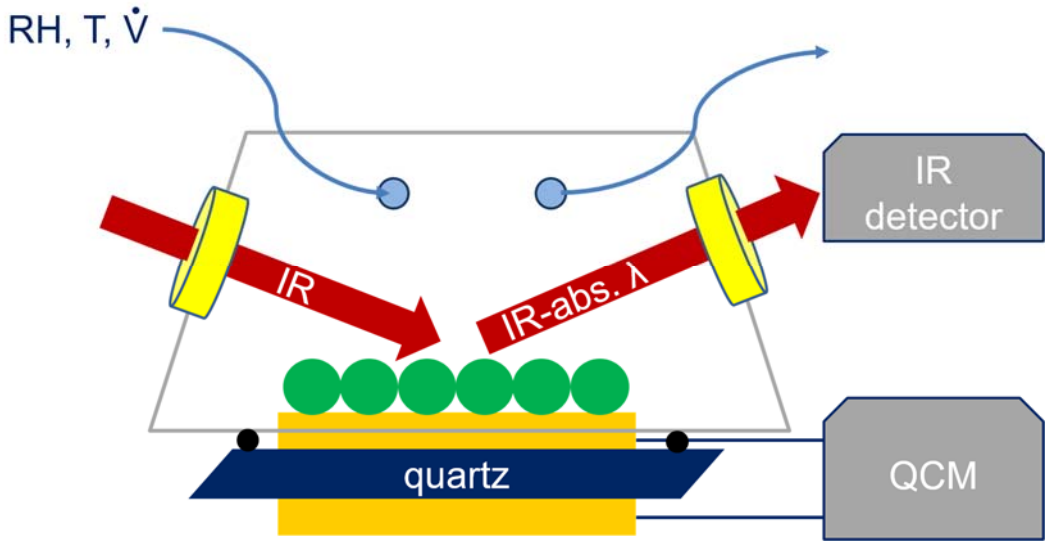


*Figure 45: Schematic of the setup for the combined in-situ QCM-D / FT-IR experiments [112].*

In addition to the new setup, a combination of experiments was derived allowing for the acquisition of suitable reference data for both QCM and FT-IR spectra (Figure 46.). Initially, the as received QCM crystals were cleaned according to the procedure presented in section 3.3.1.

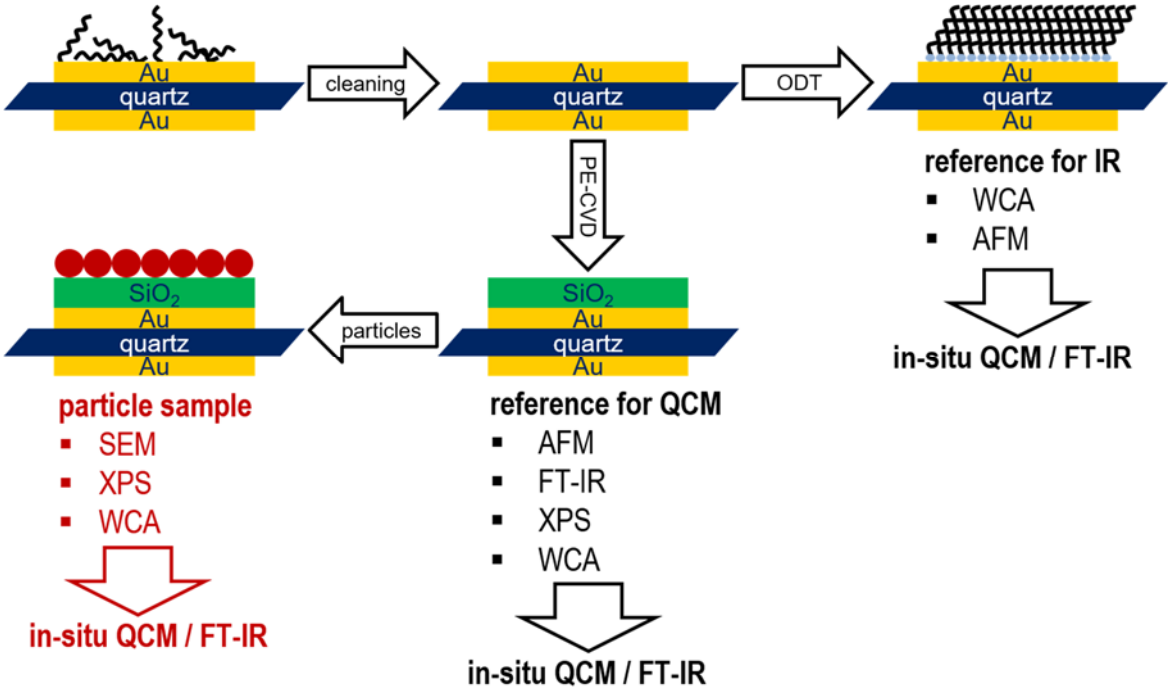


*Figure 46: Proposed set of experiments for the in-situ analysis of water adsorption on small nanoparticle ensembles (Figure adopted from [112] with small variation).*

As the QCM gives a surface area specific mass change a suitable reference system had to be created to put the particle data into context. For this reason QCM crystals were coated with a thin and smooth $SiO_2$ layer prepared via plasma enhanced CVD route as described in section 3.3.3. Prepared layers have been extensively characterized by various techniques like AFM, XPS and FT-IR (section 4.3), followed by the actual in-situ experiment with a stepwise increase in relative humidity collecting QCM as well as FT-IR data at all times. Subsequently, crystals were removed from the experimental setup and coated with $SiO_2$ particles as described in section 3.2.1 followed by extensive ex-situ characterization (section 4.3). Finally, crystals were again measured by means of combined QCM-D / FT-IR. Only employing this complex procedure, it was possible to normalize the mass change as derived from the QCM data for the increase in effective surface area. Mentioned normalization process will be disused in section 4.4.1. in great detail.

By nature, FT-IR probes not only the water absorbed on the specimen but also the water being adsorbed on the measurement cells windows as well. Therefore, another approach for an appropriate reference system had to be developed with respect to the FT-IR data. For this reason, another set of QCM crystals were coated with octadecane-thiol (ODT) self-assembled monolayers as described in section 3.3.2, resulting in ultra-hydrophobic surfaces. These crystals were then introduced to the experimental setup and the in-situ experiment was

repeated with identical relative humidity steps. All FT-IR data of the actual samples was then referenced based on the corresponding measurement of the SAM modified crystals effectively canceling out the water being adsorbed on the cells windows. Hence, resulting spectra would only consist of water being adsorbed on the particle/$SiO_2$ layer surface.

## 4.2. Development of experimental setup

Development of the cell necessary for the combined in-situ QCM-D / FT-IR experiments was a multistep process. With respect to the QCM part of the experiment, planned cell had to feature a holder assembly for the QCM crystal contacting both electrodes. Moreover, the working electrode had to be set to ground potential in order to avoid unwanted effect originating from charging such as the so called piezoelectric stiffening previously described by Johannsmann [113].

As for the FT-IR part of the experiment, the cell had to feature a form factor allowing it to fit into a commercial available infrared-reflection-absorption (IRRAS) cell featuring a mirror system allowing for variable angles of incidence. Moreover, the cell volume had to be sealed against the spectrometer using an appropriate window material allowing for the IR-light to pass through and at the same time keeping the humid atmosphere contained within. In addition, a rather short distance between the windows and the specimen was desirable as this would limit the intense gas phase water signals to a minimum.

For atmospheric control, the cell volume had to be small enough so that the gas could be exchanged fast with respect to the timescale of the experiment. Furthermore, in preparation for future experiments involving UV-light irradiation, a connector for a suitable light source had to be provided facilitating the irradiation of the QCM crystal.

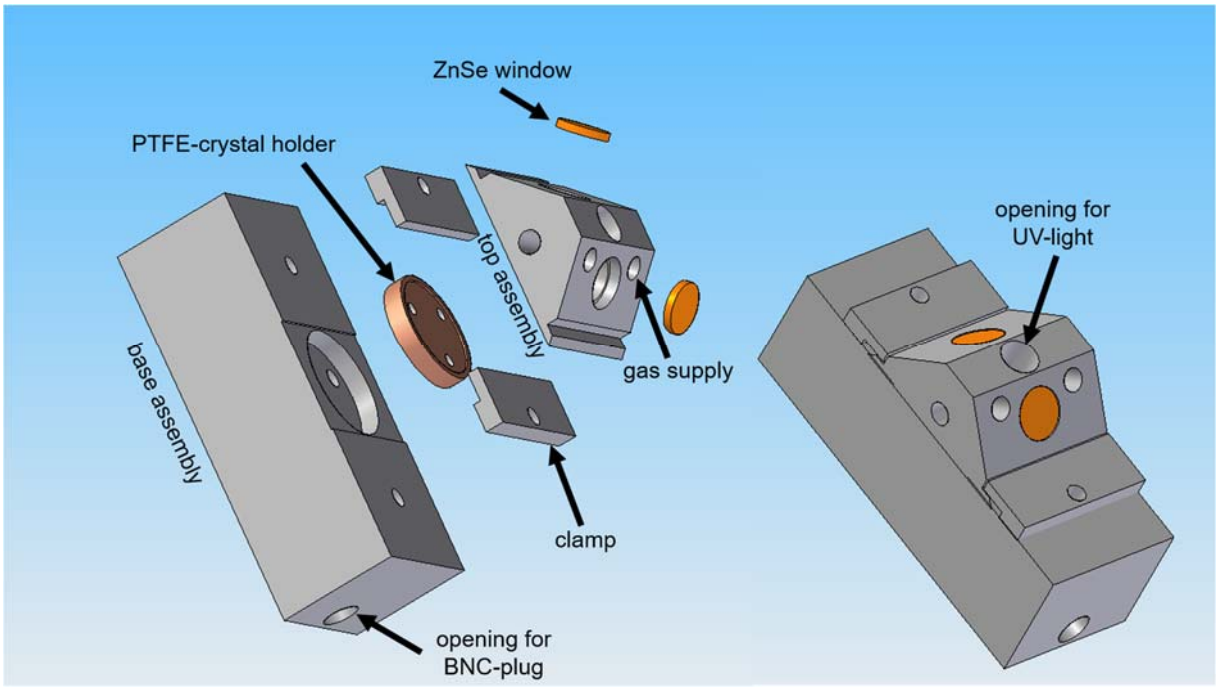


*Figure 47: Model of the first iteration of the cell for the in-situ QCM-D / FT-IR experiments.*

During preliminary experiments using the first iteration of the cell (Figure 47), certain limitations were encountered. E.g. in the first iteration the ZnSe windows had been glued into the cell assembly. However, it was found that most resins tend to fully wet the surface of the windows during the gluing process and would therefore always contribute to the single channel spectra. Although, in the sense of subtracted spectra, this did not play a major role, this unwanted effect had to be accounted for in the second generation. As a result, the second generation featured a mechanism which allowed for a mechanical fixture of windows using Viton® gaskets. In addition, it was found that a direct measurement of the relative humidity in close proximity to the crystal would be desirable. Hence, the setup was customized in such a way that a miniaturized probe for relative humidity determination could be placed within the cells volume. A corresponding schematic of the improved second generation cell is presented in Figure 48.

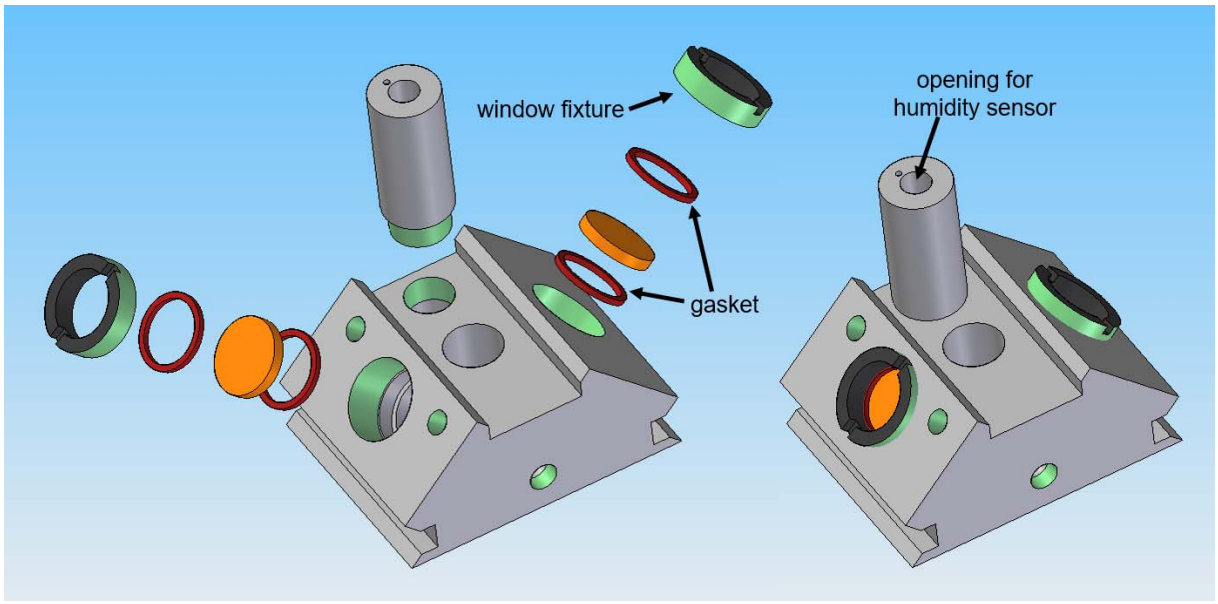


*Figure 48: Schematic of the improved top assembly part for the in-situ QCM-D / FT-IR experiment.*

In order to control the relative humidity in the cell, a custom designed humid air generator was used. In contrast to most commercially available systems which quickly alternate between a humid and a dry stream in order to create an atmosphere with desired water contend, the presented setup was able to provide a continuous stream of the process gas. This was found to be critical with respect to the QCM measurement as the crystal reacted sensitively to small variations of the gas flow.

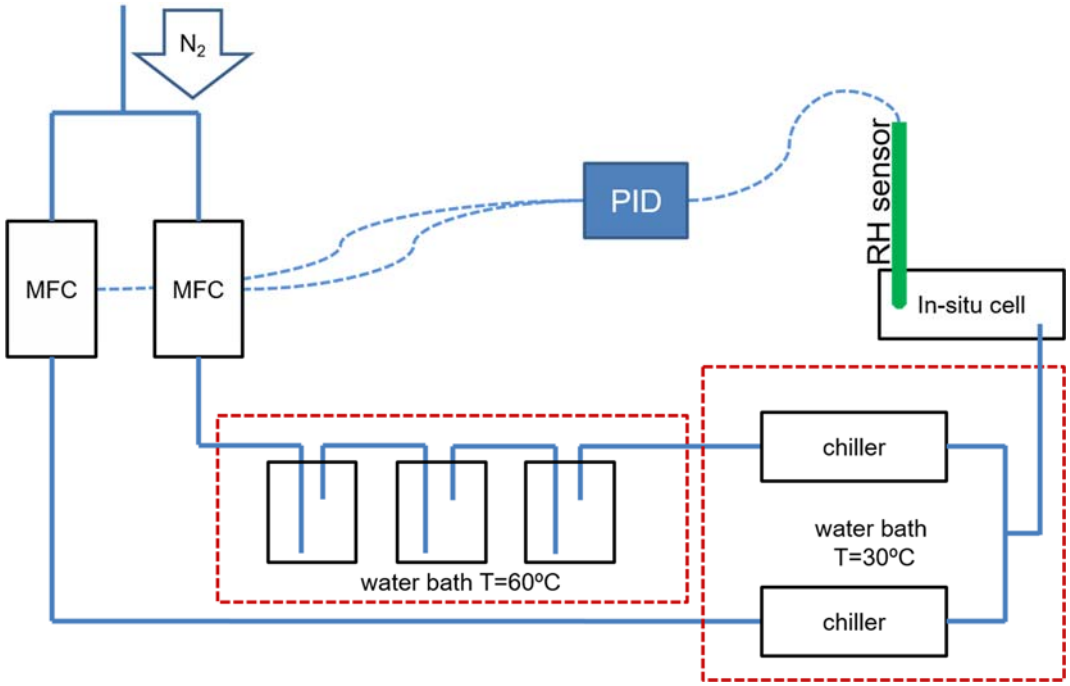


*Figure 49: Schematic of the custom designed humid air generator.*

The setup consisted of two mass flow controllers (MFC), two water baths with adjustable temperature and three bubblers filled with ultra-pure water. Moreover, a miniaturized relative humidity probe connected to a PID controller was added to automate the system. As depicted in Figure 49, this setup provided a stream of nitrogen with desired relative humidity by intermixing a dry stream with the appropriate amount of a second, fully wetted stream. In order to prevent any condensation within the device, all tubes were equipped with a heating system up to close proximity to the in-situ cell.

## 4.3. Ex situ characterization of substrates and particle layer composition

### 4.3.1. Ex-situ characterization of reference samples

Plasma polymer films were extensively characterized prior to the in-situ experiment and particle deposition. Initially performed AFM topography imaging on the PE-CVD $SiO_2$ layer modified QCM crystal substrates reveled a smooth surface with an RMS roughness in the range of ≈1.7 nm (Figure 50-A).

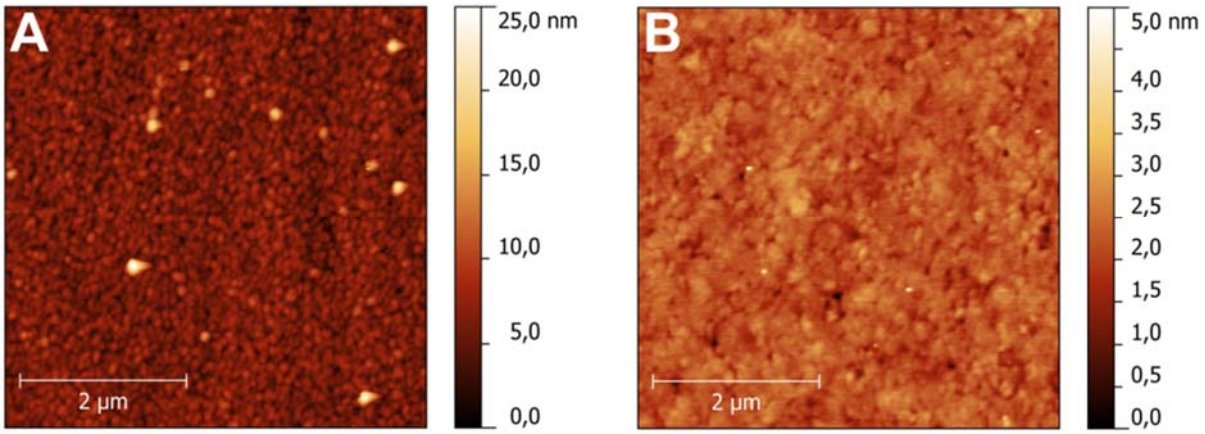


*Figure 50: Intermittent contact mode AFM topography imaging of PE-CVD modified QCM crystal substrate (A) and freshly cleaved mica template stripped gold (B). RMS roughness was determined to be 1.7 nm (A) and 0.3 nm (B). Figure adopted from [112].*

Reference experiments on PE-CVD $SiO_2$ layers deposited with identical parameters on mica template stripped gold featured even smoother layers with an RMS roughness of ≈0.3 nm. Hence, it can be concluded that the film roughness is mainly governed by the substrate morphology. For further chemical analysis, grazing incidence FT-IR spectroscopy was employed to as prepared films as depicted in Figure 51.

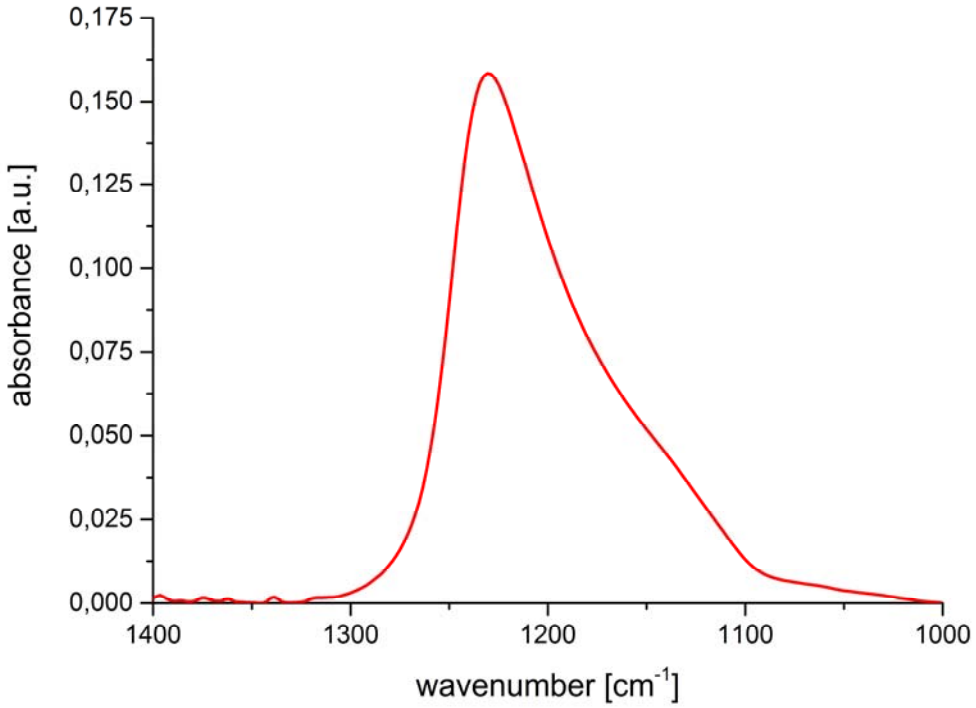


*Figure 51: Grazing incidence FT-IR spectrum of as prepared PE-CVD $SiO_2$ layer on quartz crystal substrate. Presented spectrum has been referenced with respect to a octadecane-thiol covered gold surface. Presented peak is characteristic for the Si-O-Si mode of oscillation, demonstrating the TO and LO modes of vibrations (Figure adopted from [112]).*

Presented spectrum showing the characteristic Si-O-Si mode has been referenced with respect to an octadecane-thiol covered gold substrate. From the spectrum, it can be concluded that the deposited layer exhibited no residual organosilane contamination considering that the $Si-CH_3$ signal at 1270 $cm^{-1}$ is absent [114]. Therefore, it is safe to assume that the layer was glasslike and fully inorganic in nature representing a good reference for the actual $SiO_2$ nanoparticles. Keeping in mind that the composition of the outmost surface has a crucial effect on the in-situ experiments, complementary XPS analysis was preformed to characterize the surface chemistry of the top 2-5 nm.

Corresponding XPS data presented in Figure 52 indicates only a minor contamination of carbon on the surface which is typical for samples prepared under ambient condition. This result further supports the FT-IR data also suggesting a purely inorganic film chemistry.

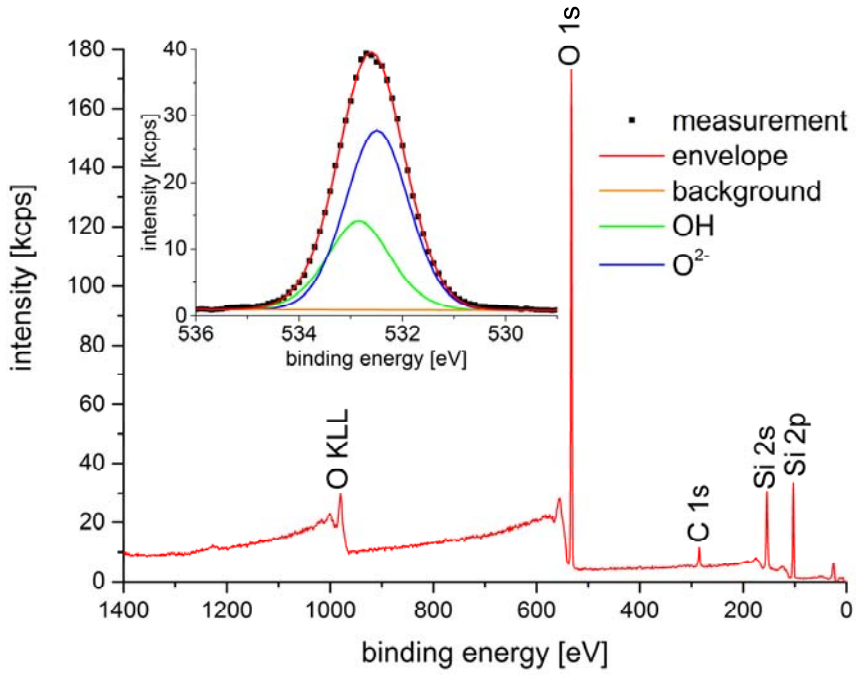


*Figure 52: XPS analysis of as prepared $SiO_2$ layer prepared via PE-CVD route on a QCM crystal substrate. The insert shows the O 1s signal fitted with two contribution corresponding to the $O^{2-}$ and OH species. (Data adopted from [112]).*

Results from the quantitative analysis of the XPS data (Figure 52) are presented in Table 1.

Table 1: Atomic surface composition of PE-CVD $SiO_2$ layer derived via XPS.

| species | content [at%] |
|---|---|
| Si | 36.7 |
| C | 6.5 |
| O | 56.8 |

In addition, the rather low full width at halve maximum of the O 1s peak indicates only two contributions originating from the inorganic matrix ($O^{2-}$, 37.8 at%) and a partially hydroxylated surface (OH, 19.0 at%). Moreover, the total absence on any gold related signals suggest that deposited film exhibited no macroscopic cracks.

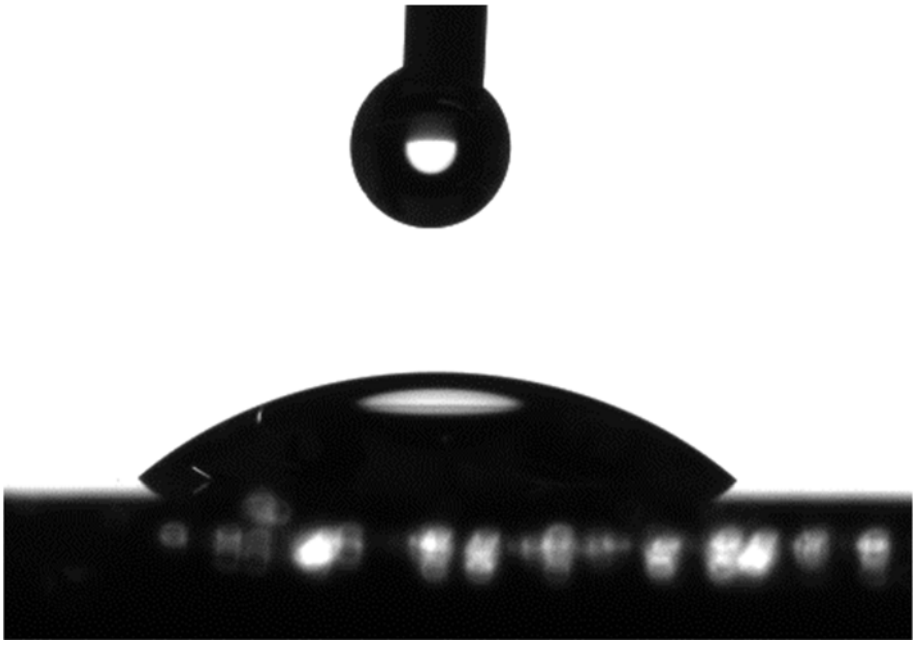

*Figure 53: Static water contact angle of PE-CVD $SiO_2$ layer on QCM crystal substrate.*

Finally, surface wettability was determined by means of static water contact angle measurements. For better statistics, measurements were repeated at least six times on each sample. In case one value deviated more than 8 degrees, additional two measurements were performed and the outliner was discarded. As prepared PE-CVD samples featured an average contact angle of 40.5° (Figure 53) indicating a hydrophilic surface which is in good agreement with the earlier discussed XPS data.

### 4.3.2. Ex-situ characterization of particle samples

Particle surface chemistry was analyzed by means of XPS using nanoparticle power generated by evaporation of the nanoparticle suspension. Received solid was prepared as described in section 3.5.2 using an indium substrate. Acquired spectra presented in Figure 54 indicate only a minor carbon contamination characteristic for samples which were exposed to ambient conditions.

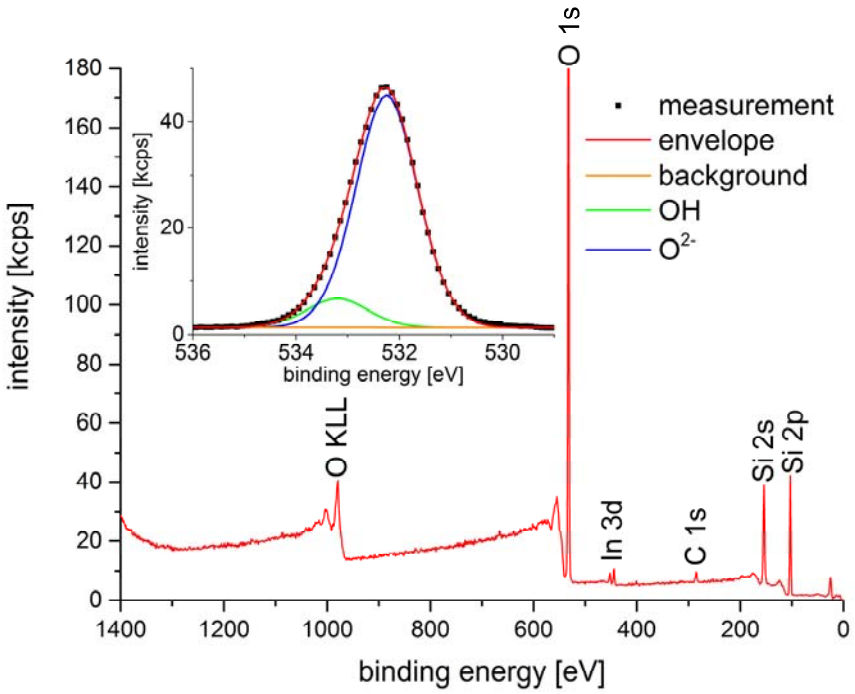


*Figure 54: XPS spectra of $SiO_2$ nanoparticle powder embedded in indium matrix. In 3d signals around 444 eV originate from the matrix material and are not a feature of the particles. The insert shows the O 1s signal fitted with two contribution corresponding to the $O^{2-}$ and OH species. (Data adopted from [112]).*

Moreover, the small shoulder of the $O^{2-}$ peak towards higher binding energies suggests a partially hydroxylated surface ($O^{2-}$: 52.3 at%, OH: 6.5 at%). Corresponding quantitative atom composition is presented in Table 2.

Table 2: Atomic surface composition of the $SiO_2$ spheres derived via XPS.

| species | content [at%] |
|---|---|
| Si | 38.0 |
| C | 3.2 |
| O | 58.8 |

In addition to the XPS analysis, specific surface area of the particle powder was analyzed by means of BET method according to the procedure described in section 3.5.6 with typical values in the range of 12.68 $m^2 \cdot g^{-1}$.

Particle samples intended for in-situ QCM-D / FT-IR experiments were prepared using PE-CVD modified QCM crystal reference substrates via sedimentation method as described earlier in section 3.2.1. Received samples had been characterized by means of FE-SEM prior to the in-situ experiment in order to determine the surface coverage (Figure 55 and Figure 56).

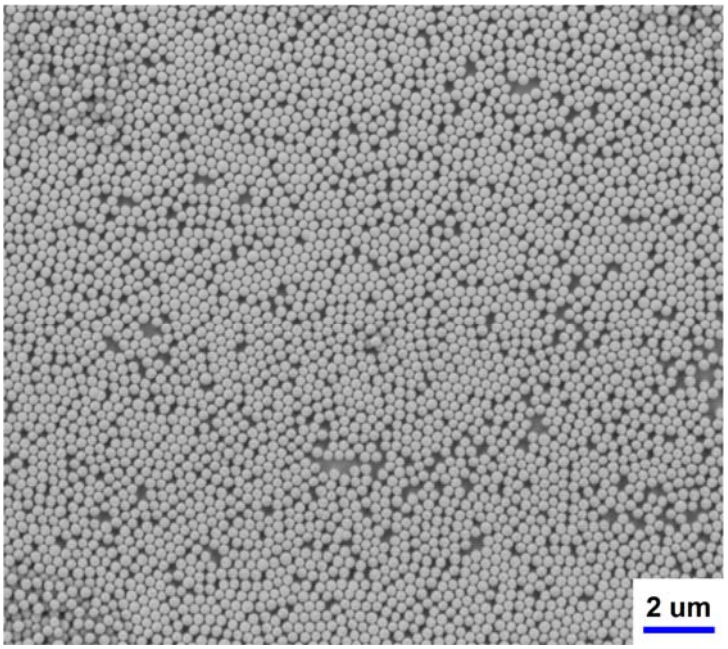


*Figure 55: FE-SEM image of $SiO_2$ particles on a $SiO_2$ plasma polymer modified QCM crystal. Surface coverage was approximated with 1.1 monolayers resulting in a surface increase factor of ≈5.3 as discussed later in this section. The average particle diameter was found to be 250 nm. (Figure adopted from [112]).*

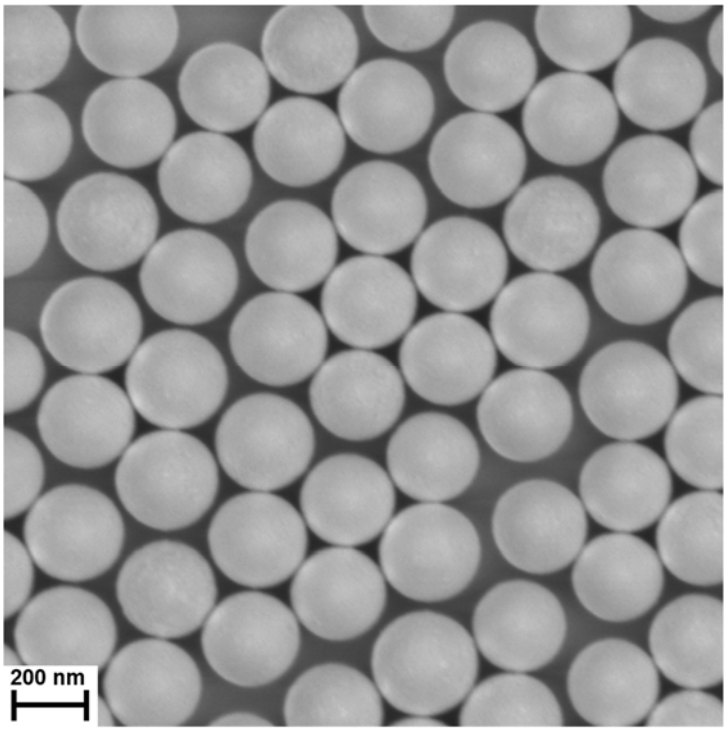


*Figure 56: High resolution FE-SEM image of the sample presented in Figure 55.*

It was found that a monolayer coverage was predominant. Nevertheless, a second layer was occasionally observed. Most of the particles in the first layer were in hexagonal close packing (hcp) with six spheres in direct contact. However, there were also domains in which the packing was not perfectly close and the spheres were lacking some of their neighbors. Overall the coverage was estimated to feature ≈1.1 monolayers.

## 4.4. Study on the water adsorption via combined in-situ QCM-D / FT-IR setup

### 4.4.1. Evaluation of QCM-D data

Combined in-situ QCM-D / FT-IR water adsorption studies were performed on as prepared $SiO_2$ plasma polymer films as well as on plasma polymer films coated with $SiO_2$ spheres.

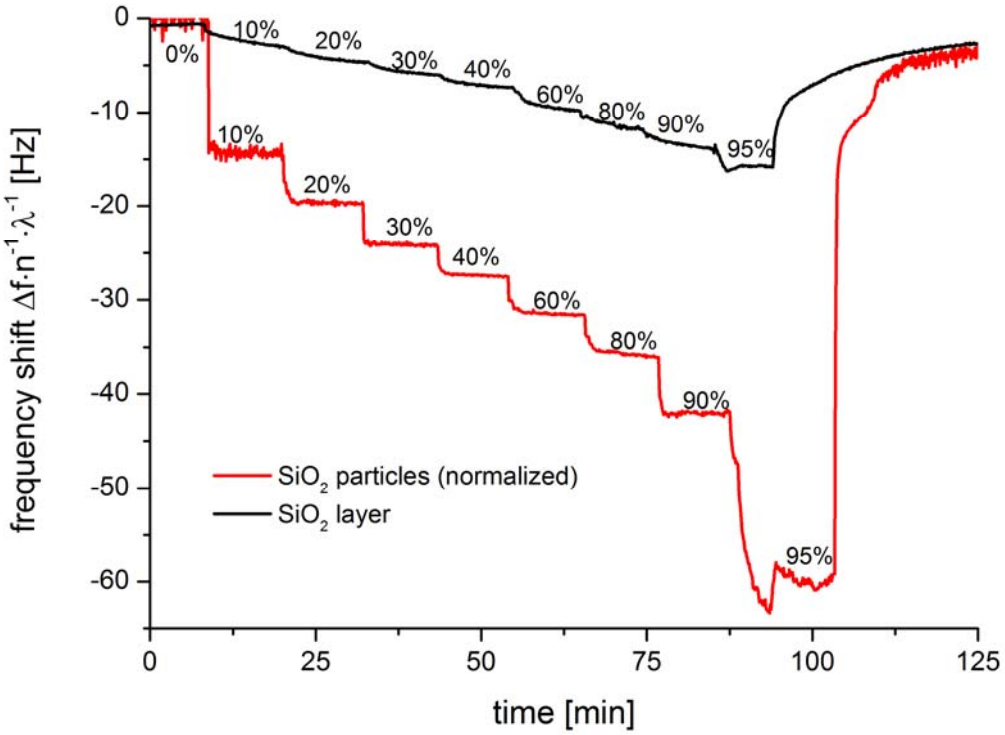


*Figure 57: QCM-D measurements of a smooth $SiO_2$ plasma polymer coated crystal (black) and the particle modified sample (red). Frequency shifts were divided by the order of overtone (n) observed and the surface increase factor λ (equation(4.7) later in this section). Indicated percentages represent the relative humidity in the cell. The surface increase factor for the correction was found to be ≈5.3 based on the FE-SEM and BET data. (Figure adopted from [112]).*

The QCM-D data presented in Figure 57 shows high shifts towards smaller frequencies as a result of the mass change induced by the adsorbed water. However, due to the coverage with nanoparticles, the effective surface area also increased dramatically. In order to compare the water uptake of the particle modified surface with the smooth $SiO_2$ plasma polymer, the increase in effective surface area had to be considered. Assuming a perfectly smooth surface that is covered with exactly one monolayer of hcp spheres, the effective surface increases with respect to the same layer without particles. Corresponding increase factor can be calculated by basic geometric considerations. In the case of a hcp, a fundamental translation lattice can be defined as depicted in Figure 58.

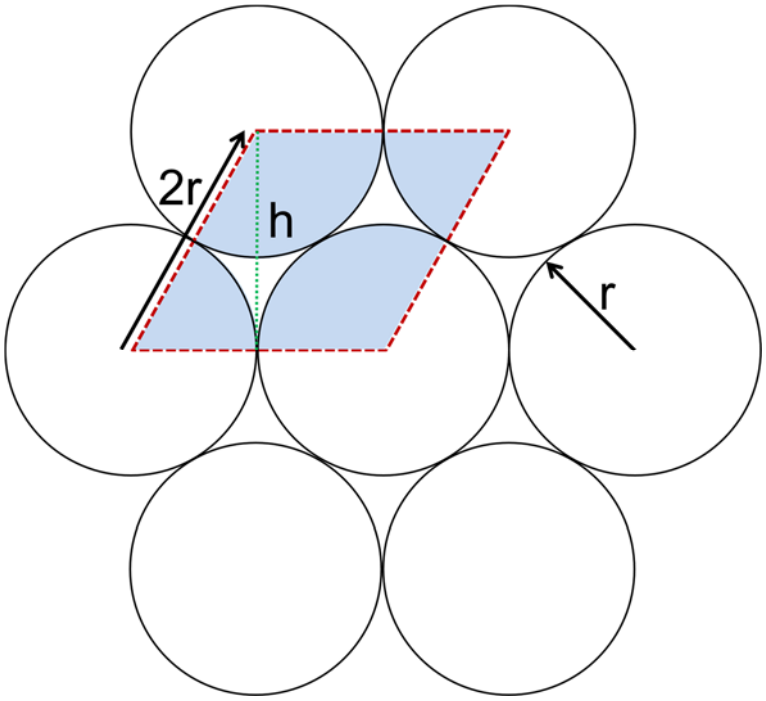


*Figure 58: Schematic of a hexagonal closest packed layer of spheres with a fundamental lattice indicated by the red parallelogram. (Figure adopted from [112]).*

Mentioned fundamental lattice indicated by the red parallelogram contains two times one third of a particle and two times one sixth of a particle as indicated by the blue fractions. Therefore, it contains a total sum of one particle.

Moreover, the surface area of the particle can be correlated to that of the area of the containing parallelogram. Via simple geometric considerations, the area of the lattice can be derived as a function of the particle radius r.

$$A_{\square} = h \cdot 2r \tag{4.1}$$

$$A_{\bigcirc} = \pi (2r)^2 \tag{4.2}$$

$$h^2 + r^2 = (2r)^2 \qquad h = r\sqrt{3} \tag{4.3}$$

Combination of equation (4.1) and (4.3) leads to expression (4.4) describing the area of the parallelogram as function of the particle radius.

$$A_{\square} = r^2 2\sqrt{3} \tag{4.4}$$

In order to obtain one of the factors for the surface increase factor λ, the ratio of the sphere and lattice surface is formed

$$\frac{A_{\bigcirc}}{A_{\square}} = \frac{\pi(2r)^2}{r^2 2\sqrt{3}}$$
$$A_{\bigcirc} = \frac{2\pi}{\sqrt{3}} A_{\square} \tag{4.5}$$
$$A_{\bigcirc} \approx 3.6 \cdot A_{\square}$$

Interestingly, the increase factor is a constant value and is found to be independent of the particle radius.

In the case of the real sample and under the assumption that the particles are in point contact to the surface, the substrate area itself cannot be neglected. Therefore, when comparing the particle modified substrate to the substrate without particles 1 has to be added to the surface increase factor accounting for the substrate area itself on which most adsorption sites are still available.

In this simple model, the substrate surface is approximated by a perfectly smooth plate. This approximation is supported by the AFM data (Figure 50-A) indicating that the real surface area is almost identical to the projection area due to the small roughness (RMS ≈1.7 nm).

Moreover, the actual surface area of one particle could potentially differ from the surface area of a perfect sphere due to a certain degree of surface roughness. BET measurements revealed the specific surface area to be 12.68 $m^2 \cdot g^{-1}$ (section 4.3.2). Taking the specific weight of $SiO_2$ for Stöber particles of 2.04 $g \cdot cm^{-3}$ [115,116] into account, the surface area of one specific particle with a diameter of 250 nm was calculated to be about ≈0.21 $\mu m^2$. This value is in good agreement with the surface area of a perfectly smooth sphere of identical diameter which is approximately 0.20 $\mu m^2$. Therefore, it is very likely that the used particles featured a negligible amount roughness and the small deviation in particle surface area originated from the small and inevitable size distribution. However, in order to derive a more general equation, the deviation of surface area from a perfect sphere is accounted for by defining a factor called β.

$$\beta = \frac{A_{BET}}{A_{perfect\bigcirc}} \tag{4.6}$$

Additionally, in most cases, prepared samples did not feature exactly one monolayer of particles. Therefore, a factor called α is defined which equals the average count of monolayers found on the sample surface as derived via FE-SEM. Taking all this into consideration the surface increase factor λ is given by:

$$\lambda = 1 + \frac{2\pi}{\sqrt{3}} \cdot \alpha \cdot \beta \tag{4.7}$$

Hence, in the case of one single monolayer of ideal smooth spheres, λ is found to be 4.6. In order to correct the acquired QCM-D data for the increase of surface area all shifts were divided by λ.

Prior to the QCM-D experiments, the actual surface coverage was determined by FE-SEM. In the case of the presented data, the surface coverage was approximated with 1.1 monolayers. Together with the BET data the resulting surface increase factor was found to be ≈5.3 for the presented dataset. When comparing the corrected frequency shifts of the particle film coated substrate to the smooth $SiO_2$ surface (Figure 57), it is obvious that the water uptake was significantly higher for the particle layer. This indicates that additional water has been adsorbed which is attributed to the formation of capillaries in the inter-particle and particle-substrate contact areas. The adsorption isotherm could be derived from the QCM-D data. For improved statistical reliability, the frequency shift values on each step were averaged and the mean shift was subsequently plotted versus the relative humidity as depicted in Figure 59.

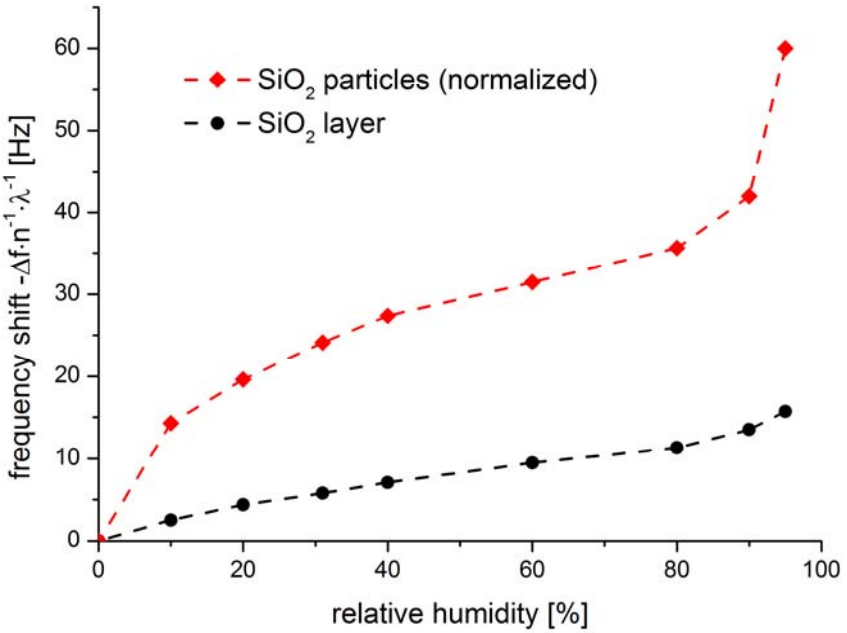


*Figure 59: Adsorption isotherm of water on the $SiO_2$ plasma polymer (black) and $SiO_2$ particle covered sample (red). Although the isotherm has been derived from the area corrected QCM-D data the total amount of water uptake is significantly higher than on the reference sample. This indicates that additional water is absorbed forming capillaries in the contact regions. (Figure adopted from [112]).*

The adsorption isotherm on the $SiO_2$ particle modified sample can roughly be divided into three segments. In the regime between 0 and 20% relative humidity, the transient is very steep

and almost half of the total water layer has been adsorbed. This indicates that water adsorption is highly favorable for the hydrophilic surface. In the second segment ranging from 20% to 80% relative humidity, the slope of the isotherm is rather low indicating that the surface is almost saturated. In the last section, the high increase in slope indicates ongoing multilayer formation as well as capillary condensation in the particle layer. In contrast to the particle modified sample, the smooth $SiO_2$ plasma polymer layer exhibited a very linear increase in water uptake throughout the whole relative humidity range.

The corresponding dissipation data of the particle modified sample presented in Figure 60 shows an increase of dissipation until a maximum has been reached at about 60% to 80% relative humidity.

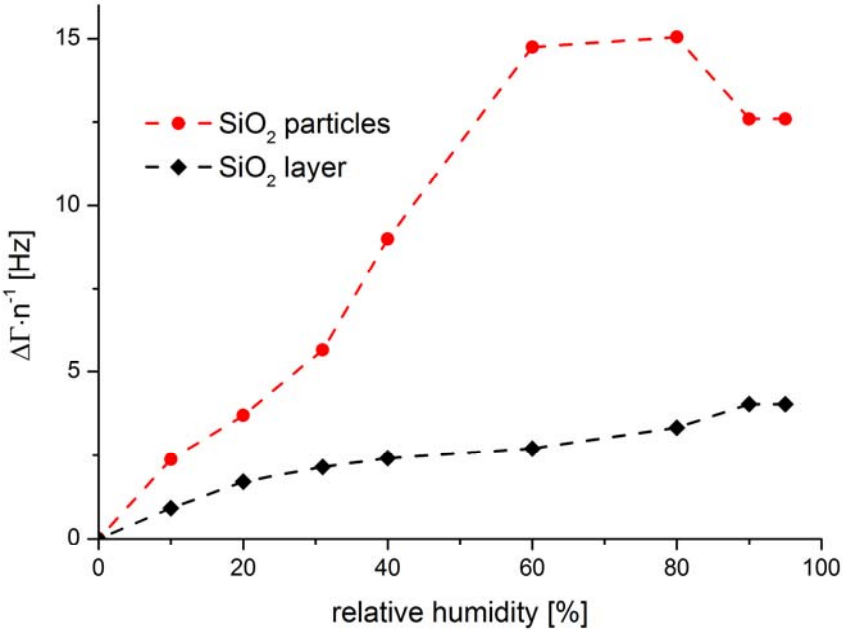


*Figure 60: Evolution of dissipation quantified by ΔΓ during the experiment. In contrast to the dissipation curve on the smooth plasma polymer, the particle modified sample exhibits a maximum around 60% to 80% relative humidity. This behavior, originating from the change of contact mechanics due to capillary formation, has already been described by Dybwad [97] and Johannsmann [95]. (Figure adopted from [112]).*

A similar behavior has previously been described by Dybwad [97] and Johannsmann [95] where it was found that the contact force between the particles and the resonator increased due to the formation of capillaries. Therefore, the system changed from elastic (weak contact forces) to inertial loading (strong contact forces) resulting in the local maximum in the dissipation. It is assumed that a similar mechanism is responsible for the dissipation results in this case. However, during the experiment, the transitional capillary state is approached in the opposite direction. In the experiment of Johannsmann and König [95] the fully wetted sample

was slowly allowed to dry. During this process, the initially continuous water film slowly evaporated inducing the formation of capillaries. As a result, the contact force increased inducing a peak of the dissipation signal during the transition. At variance, in the experiment presented, the relative humidity was slowly increased. As a result, the capillaries tended to grow according to the Kelvin equation (2.11). Hence, the growth of the capillaries resulted in two effects. Initially, the Laplace pressure decreased due to the larger capillary radius. Likewise, the wetted area grew resulting in the increase of contact force. In the case of large particles, typically both effects cancel each other (section 2.5.2), resulting in a constant capillary force over a wide range of relative humidity values [79]. However, recent experiments performed by Asay et al. [117] indicated that this assumption does not hold true for nanosized objects. They found, that in the case of different alcohols, the capillary force is strongest in the low partial pressure region and decreases for higher partial pressures. This is further supported by simulations performed by Dörmann and Schmid [80] which also found that in the case of small particles, some of the approximations used for the analytical solution do not hold true anymore. It is assumed that a similar process occurred during the experiment performed within this work.

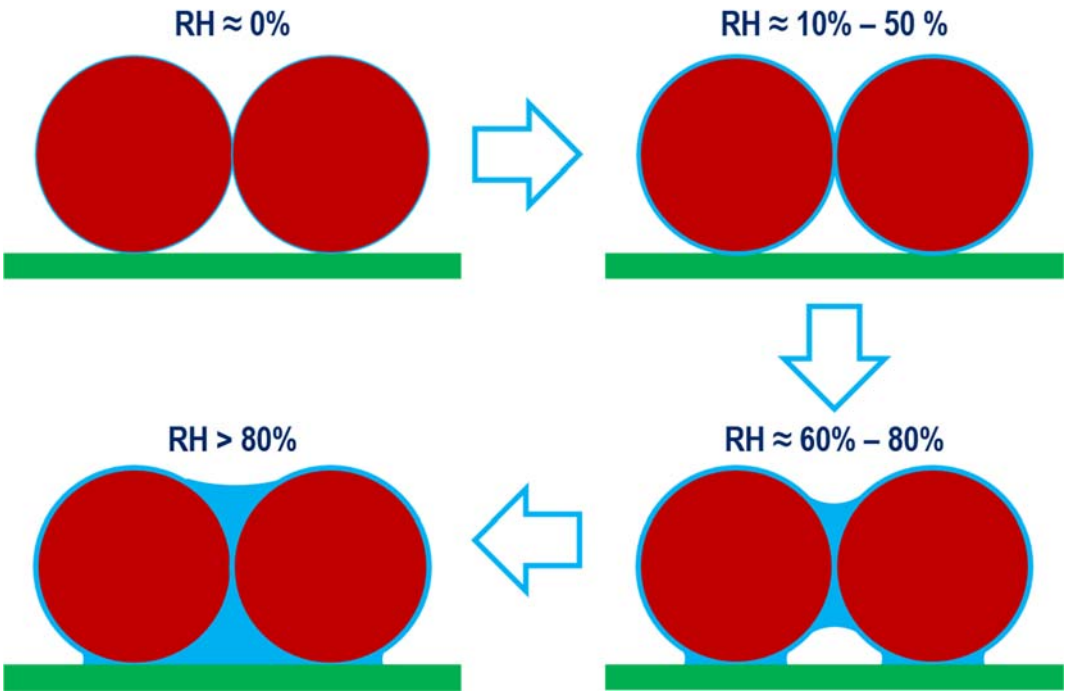


*Figure 61: Schematic evolution of the water film formation over the whole relative humidity range.*

In the initial state, the spheres were strongly attached due to the high contact force based on the very small capillary radii (Figure 61). The subsequent increase of relative humidity led to a decrease in contact force, until the system changed from inertial to elastic between 60% and 80% relative humidity. This transition caused the dissipation peak. Moreover, the increased water uptake at high relative humidity (e.g. >80%) can be attributed to ongoing capillary growth and the beginning of a closed water film formation due to the merging of previously individual capillaries. In comparison to the particle modified sample, the smooth $SiO_2$ sample exhibited a much lower rather linear increase in dissipation with no maximum indicating the absence of a significant change in mechanical properties of the film

Although, strictly speaking the Sauerbrey equation cannot be employed since the dissipation deviates from 0 it is commonly agreed that in the case of $\Delta f >> \Delta\Gamma$ it still gives acceptable results. Under this assumption the actual volume of every capillary can be calculated. In this context, the specific number of capillaries per surface area has to be estimated. Referring to Figure 58, the number of sphere per $m^2$ can be estimated by equation (4.8) assuming that each sphere blocks a total area corresponding to the parallelogram defined earlier. Moreover, the presence of more than one perfect layer is again considered by employing factor α.

$$N_{spheres} = \frac{1 \cdot m^2}{A_{\square}} = \frac{1 \cdot m^2}{r^2 2\sqrt{3}} \cdot \alpha \qquad (4.8)$$

As by definition, each sphere in the first layer shares six contacts with its direct neighbors and features one contact with the underlying substrate. According to Butt and Kappl [79], the volume of the meniscus can be calculated as a function of the reduced radius (R*) (equation (2.26)), the critical radius (r) as derived by the Kelvin equation (equation (2.11)), both wetting angles $\theta_1$ and $\theta_1$.and the distance (D) between the particles via equation (4.9).

$$V_{cap} = \pi R^* \left[ 4r^{\,2} \left( \cos\left(\Theta_1\right) + \cos\left(\Theta_2\right) \right)^2 - D^2 \right] \tag{4.9}$$

Under the assumption of D=0 and full wetting the much simpler equation (4.10) can be derived.

$$V_{cap} = 16\pi R^* r^2 \tag{4.10}$$

In the case of two identical spheres in contact R* is found to be $0.5 \cdot R_{1,2}$, whereas in the case of the contact between the sphere and the substrate plane $R^* = R_1$.

$$V_{cap,\bigcirc\bigcirc} = 16\pi \frac{R}{2} r^2 \tag{4.11}$$

$$V_{cap,\bigcirc\|} = 16\pi R r^2 \tag{4.12}$$

Thus, the volume of the meniscus between the sphere and the substrate features twice the volume of the menisci between two adjacent spheres. Moreover, in the case of the particle-particle contact, only halve of the total capillary volume can be accounted to every individual particle as both partners share the same volume. Contrary to that the capillary between the substrate can be fully attributed to every single sphere. Therefore, the total capillary volume for every particle is given by the equation:

$$\begin{aligned} V_{cap,total,hcp} &= \frac{6}{2} \cdot V_{\bigcirc\bigcirc} + V_{\bigcirc\|} \\ &= 24 \cdot \pi R r^2 + 16 \cdot \pi R r^2 \\ &= 40 \cdot \pi R r^2 \\ &= 5 \cdot V_{cap,\bigcirc\bigcirc} \end{aligned} \tag{4.13}$$

However, equation (4.13) only holds true for one perfect layer of spheres. In the case of a partial second layer further considerations have to be made. In the case of a particle in the first layer which features a second particle layer above it, additional three particle-particle

capillaries are formed. Similar to the previous case however all three capillaries are again equally shared between both partners. Thus the overall volume is given by equation (4.14).

$$\begin{aligned} V_{cap,total,hcp,bottom} &= 5 \cdot V_{cap,\bigcirc\bigcirc} + \frac{3}{2} \cdot V_{cap,\bigcirc\bigcirc} \\ &= 6.5 \cdot V_{cap,\bigcirc\bigcirc} \end{aligned} \tag{4.14}$$

In the case of the particle in the upper layer, it features the same 6 contacts with its neighbors as particles in the primary layer, however, instead of the contact to the substrate it features the aforementioned 3 contacts with particles from the layer underneath.

$$\begin{aligned} V_{cap,total,hcp,top} &= \frac{6}{2} V_{cap,\bigcirc\bigcirc} + \frac{3}{2} \cdot V_{cap,\bigcirc\bigcirc} \\ &= 4.5 \cdot V_{cap,\bigcirc\bigcirc} \end{aligned} \tag{4.15}$$

Combining equations (4.13),(4.14),(4.15) with the monolayer count α, expression (4.16) can be derived providing the average total capillary volume per particle for every given relative humidity.

$$\begin{aligned} V_{cap,total,\varnothing} &= \left[ \left(1-(\alpha-1)\right) \cdot V_{cap,total,hcp} + (\alpha-1) \cdot V_{cap,total,hcp,bottom} + (\alpha-1) \cdot V_{cap,total,hcp,top} \right] \cdot \frac{1}{\alpha} \\ &= \left[ \left(1-(\alpha-1)\right) \cdot 5 \cdot V_{cap,\bigcirc\bigcirc} + (\alpha-1) \cdot 6.5 \cdot V_{cap,\bigcirc\bigcirc} + (\alpha-1) \cdot 4.5 \cdot V_{cap,\bigcirc\bigcirc} \right] \cdot \frac{1}{\alpha} \\ &= V_{cap,\bigcirc\bigcirc} \left[ \left(1-(\alpha-1)\right) \cdot 5 + (\alpha-1) \cdot 6.5 + (\alpha-1) \cdot 4.5 \right] \cdot \frac{1}{\alpha} \\ &= V_{cap,\bigcirc\bigcirc} \cdot \frac{\Lambda}{\alpha} \end{aligned} \tag{4.16}$$

To make this expression shorter, the rather bulky factor in brackets has been combined in to new variable Λ. In case of one perfect layer with no particles on top $\Lambda \cdot \alpha^{-1}$ is found to be 5 which is in agreement with equation (4.13), whereas in the case of two stacked monolayers $\Lambda \cdot \alpha^{-1}$ is found to be 5.5. However, it has to be noted, that this simple model does not cover particles with missing neighbors found on defects or in the case of particle on the edge of a larger domain of spheres. Nevertheless, this systematic error should have only a minor effect to the overall calculations as FE-SEM images indicated that the surface was mostly covered with large domains of particles. Hence the number of spheres situated at boundary positions was small compared to the number of spheres within domains.

This average volume $V_{cap,total,,\varnothing}$ is important since it can be derived from the actual experimental data. Employing Sauerbrey equation to the observed frequency shifts, the area specific mass

change can be calculated. Dividing this area specific mass change by the area specific number of spheres as presented in equation (4.8), the fraction of mass which corresponds to the water belonging to one particle can be derived. Assuming the mass can be directly correlated to the volume via the density (ρ), the observed frequency shift can be used to calculate $V_{cap,\varnothing}$.

$$V_{cap,total,\varnothing} = \frac{\Delta m_{Sauerbrey,RH}}{N_{spheres} \cdot \rho_{H_2O}} = \frac{-c \cdot \Delta f_{RH}}{N_{spheres} \cdot \rho_{H_2O}} \tag{4.17}$$

Moreover, since Λ is known, the Volume of a capillary in the particle-particle contact can be deducted.

$$V_{cap,\bigcirc\bigcirc} = \frac{-c \cdot \Delta f_{RH} \cdot \alpha}{N_{spheres} \cdot \rho_{H_2O} \cdot \Lambda} \tag{4.18}$$

Corresponding theoretical and experimental derived capillary volumes are presented in Table 3.

Table 3: Measured capillary volumes and corresponding theoretical values.

| RH | $V_{cap,oo}$ experiment [nm³] | $V_{cap,oo}$ theory [nm³] |
|---|---|---|
| 10% | ≈1,3·10⁵ | ≈6,7·10² |
| 20% | ≈1,8·10⁵ | ≈1,4·10³ |
| 30% | ≈2,2·10⁵ | ≈2,5·10³ |
| 40% | ≈2,5·10⁵ | ≈4,2·10³ |
| 60% | ≈2,9·10⁵ | ≈1,4·10⁴ |
| 80% | ≈3,2·10⁵ | ≈7,2·10⁴ |
| 90% | ≈3,8·10⁵ | ≈3,2·10⁵ |
| 93% | ≈5,4·10⁵ | ≈6,8·10⁵ |

From the raw data it is evident that the measured volume is much higher that the theoretical value. However, from the plot depicted in Figure 62 it can be seen that the difference is almost constant in the low to mid humidity range. Therefore, it is assumed that this discrepancy corresponds to the water being adsorbed on the surface rather that the water which is situated in the capillaries. Moreover, it can be seen that the slope of the experimental data changes between 60% to 80% RH which is in good agreement with the corresponding theoretical data as this is the exact range when the capillary growth begins to dominate.

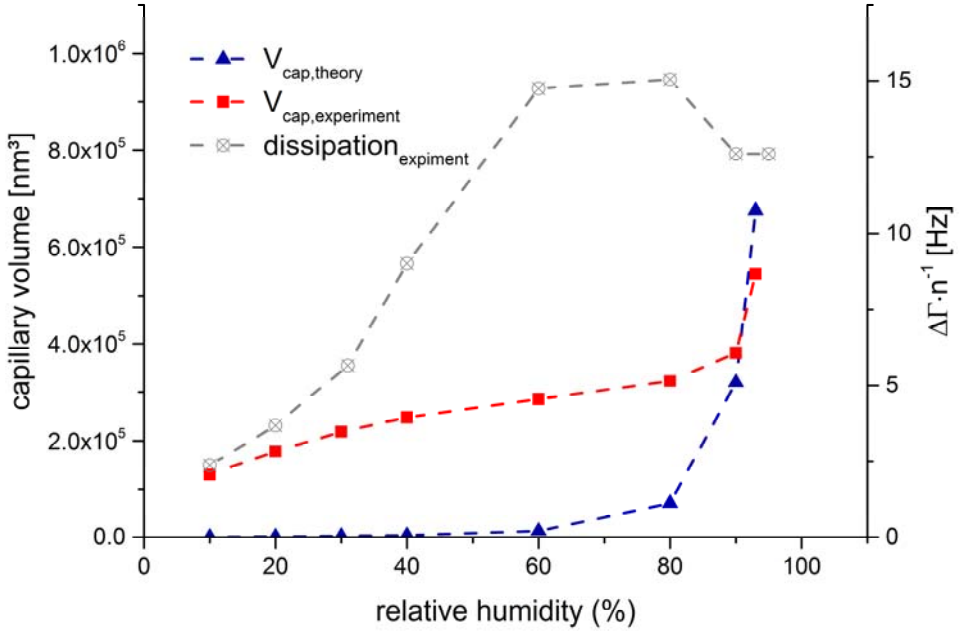


*Figure 62: Experimentally (red) and theoretically (blue) determined capillary volume. The grey curve represents the corresponding dissipation data and is identical to that of the particle sample presented in Figure 60.*

This assumption is further supported by the corresponding dissipation data which features the maximum earlier discussed exactly at the onset of capillary growth as predicted by the theory. The surpassing of the last experimental value by the corresponding theoretical value can be explained by the fact that in the case of a continuous water film the masses derived by Sauerbrey equation become increasingly wrong because of the more complex film mechanic. Overall however, the trend of the experimentally derived data is in good agreement with the theory.

### 4.4.2. Evaluation of FT-IR reflection data

FT-IR spectra were acquired simultaneously to the QCM-D experiment. All spectra were referenced to the spectra measured on the ODT sample at the same relative humidity. It was found that the OH-peak in the region of 3300 $cm^{-1}$ rose with increasing relative humidity indicating the adsorption of water on the particle surfaces.

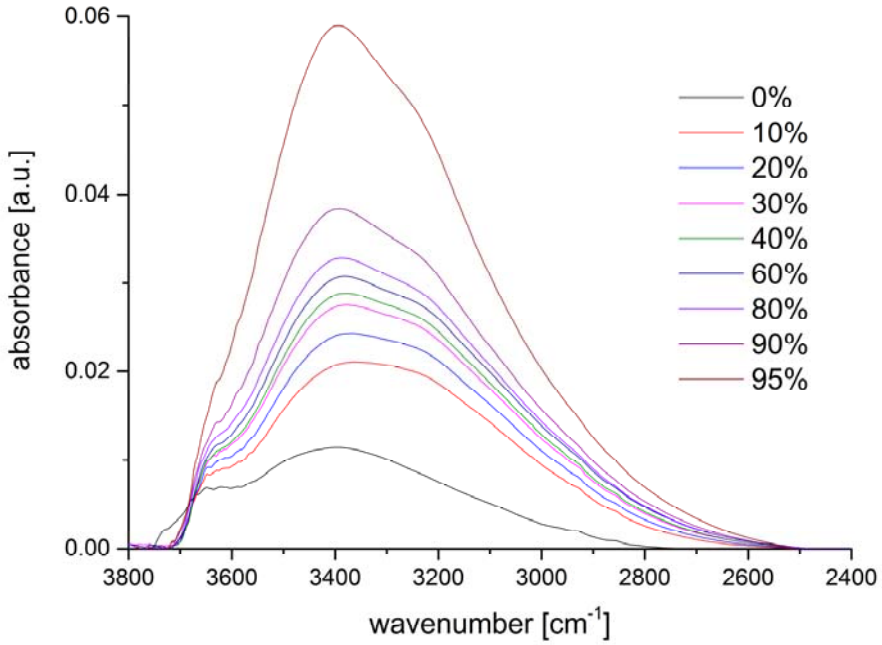


*Figure 63: FT-IR data of the $SiO_2$-particle coated QCM crystal. Presented spectra where measured simultaneously to the QCM-D data (Figure 57 and Figure 60). All spectra are referenced to the ODT SAM covered QCM crystal measured under identical conditions (temperature, relative humidity, gas flow rate). (Figure adopted from [112]).*

Moreover, in contrast to the measurement on the smooth $SiO_2$ layer, the intensity of the peak was dramatically higher which is in good agreement with the QCM-D data.

The FT-IR-data measured at 0% RH features a characteristic shoulder at ≈3700 $cm^{-1}$ and a peak at around ≈3400 $cm^{-1}$ (Figure 63). While the latter is mainly due to a single monolayer of water molecules adsorbed at the silanol groups of the silica surface [118], the former indicates the presence of so called "free" or "dangling" OH-groups of the surface silanols and/or of the adsorbed water monolayer [119,120], respectively. The shoulder at ≈3700 $cm^{-1}$ immediately decreased to zero when air of any relative humidity was being introduced to the measuring cell. The occurrence of the so called "ice-like" peak at around 3200 $cm^{-1}$ at higher relative humidity refers to the adsorption of multiple layers of water at the surface. For a more detailed discussion, the measured spectra were deconvoluted as demonstrated in Figure 64 for the measurement at 60% relative humidity.

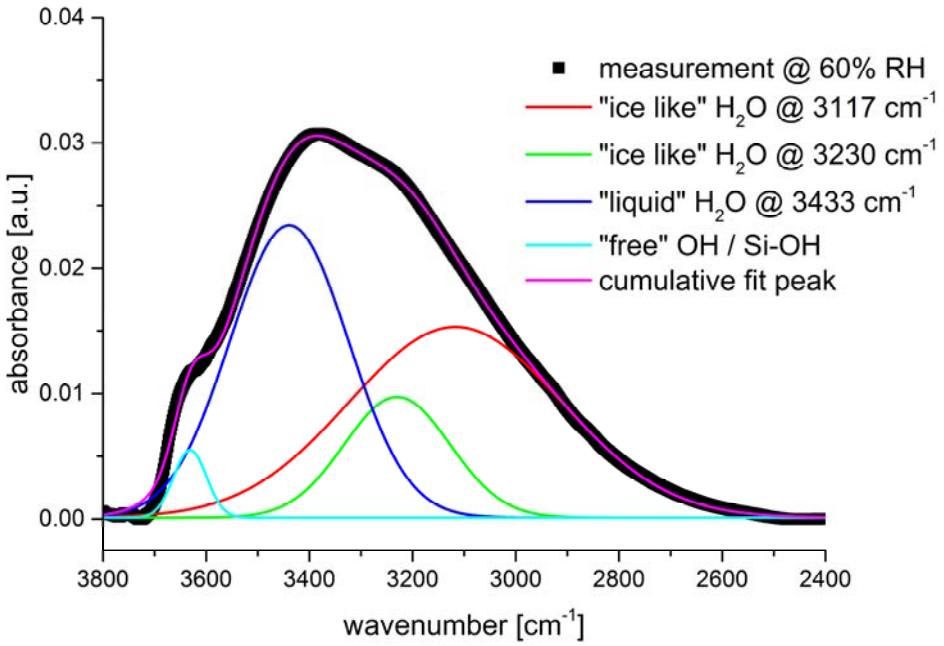


*Figure 64: Presentation of peak deconvolution of the OH-peak in the region between 2400 $cm^{-1}$ and 3800 $cm^{-1}$ based on the dataset measured at 60% relative humidity. The peak has been fitted with four components in total, corresponding to "ice-like" $H_2O$ (3117 $cm^{-1}$ & 3230 $cm^{-1}$), "liquid" $H_2O$ (≈3400 $cm^{-1}$), and "free" OH / Si-OH (≈3600 $cm^{-1}$). (Figure adopted from [112]).*

Previous publications [43,120-123] showed that the OH-peak consists of multiple sub-peaks corresponding to vibrations of "liquid" (≈3400 $cm^{-1}$) and "ice-like" (3230 cm-1 & 3117 $cm^{-1}$) water as well as "free OH" (≈3700 $cm^{-1}$), respectively. Therefore, the fit consists of multiple components corresponding to "ice-like" water (3117 $cm^{-1}$ and 3230 $cm^{-1}$) as well as bulk liquid water (≈3400 $cm^{-1}$) and a rather general peak at around ≈3650 $cm^{-1}$ that corresponds to dangling OH-bonds of water molecules and/or silanol groups at low relative humidity. The presence of the "ice-like" peaks is due to the fact that at higher relative humidity multiple monolayers of water are adsorbed at the surface that are oriented similar to the water/air interface [120]. The corresponding peaks have been attributed to the hydrogen bonds between the first and second monolayer of water [121], which is why the "ice-like" peaks are appearing at higher relative humidity only. However, as shown previously by Zhang and Kühne [122], the peaks at 3400 $cm^{-1}$ and 3230 $cm^{-1}$ corresponds to the symmetric and asymmetric stretching modes (ν1 and ν2) of liquid water molecules whose hydrogen-bond strengths is asymmetric [124,125]. As a consequence, the latter "ice-like" peak must be attributed to a liquid water configuration, in spite of the name. On the contrary, the ν1 and ν2 coalesce into one peak at 3117 $cm^{-1}$ whenever the hydrogen-bond strength becomes symmetric, i.e. "ice-like". The aforementioned peak at 3650 $cm^{-1}$, which refers to free OH-groups at low relative humidity, is consistent with the fleetingly broken hydrogen-bonds due to finite temperature

within the bulk water portion at high relative humidity [119,125]. This is further supported by the fact that the associated peak area stays almost constant over the whole range of relative humidity (Figure 65).

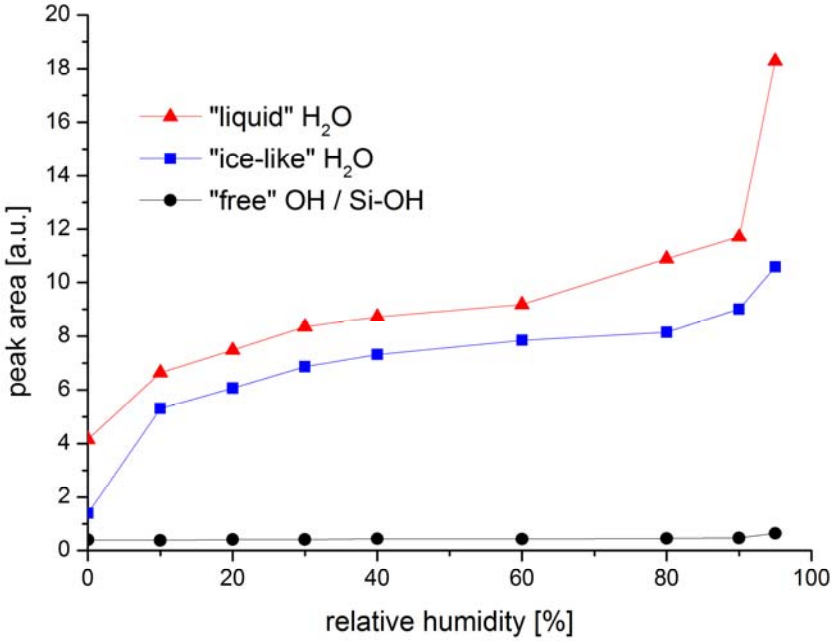


*Figure 65: Evolution of the peak area as a function of relative humidity. It can be seen that the peak of the "free" OH shows almost no change over the whole humidity range. The peak area corresponding to the "ice-like" $H_2O$ shows a very steep shape for low humidity, while for higher humidity the "liquid-like" signal shows a high increase in the peak area. (Figure adopted from [112]).*

This indicates that mentioned contribution is either originating on the one hand from dangling OH-bonds of water molecules and/or silanol groups at low relative humidity or, on the other hand, from dynamically broken OH-bonds of bulk water molecules at high relative humidity. With respect to the former, the presence of surface Si-OH groups is in good agreement with the XPS data, which also indicated the presence of OH-species based on the O 1s peak (Figure 54).

The detailed analysis of the OH-peak region revealed the presence of a single monolayer of liquid water adsorbing to the particle surface and otherwise dangling OH-groups of the water molecules and/or silanol groups under dry conditions. The steep increase in the peak area of the components corresponding to "ice-like" water indicates the presence of multiple monolayers of water as well as different absorption affinities at different sites [118]. At even higher humidity (>60%), the system more and more resembles bulk water as indicated by the strong increase in integrated area of the "liquid-like" peak. This is in good agreement with the corresponding dissipation data, which exhibits a local maximum between 60% and 80%

relative humidity (Figure 60) that can be attributed to the predominant growth of capillaries resulting in a decreased contact force (section 4.4.1). The correlation of the dissipation data with the observed water structure implies that the particle substrate contact mechanics (indicated by the QCM-D) drastically changed at the same time when adsorption of "liquid-like water" started to dominate. This might indicate that the lowering of the contact force during the inertial/elastic transition not only originates from the reduced Laplace pressure, but also from a change in the water adsorbate structure. This is further supported by comparison of the theoretical capillary volume with the IR data (Figure 66). As predicted by theory, the "liquid" like contribution featured an increased slope during the onset of capillary growth.

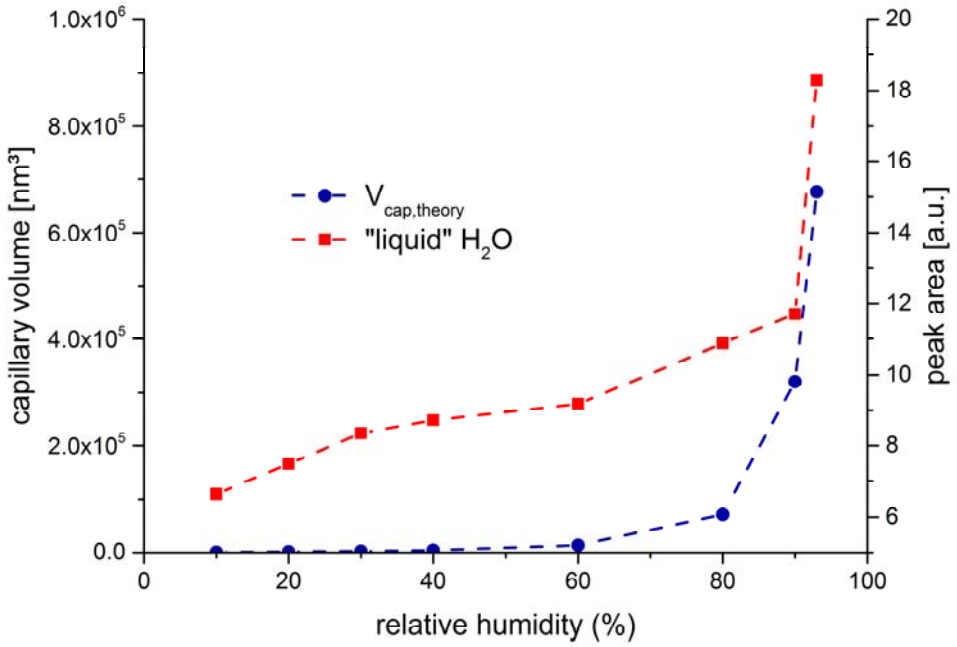


*Figure 66: Comparison of capillary volume as predicted by theory and „liquid" $H_2O$ contribution derived from the deconvoluted IR spectra.*

In addition, the isotherm derived from the QCM-D data (Figure 59) as well as the isotherm derived from the FT-IR data (Figure 65) feature a similar trend. At low relative humidity both exhibit a very steep increase in water content followed by a low increase regime between 20% to 80% relative humidity. Moreover, the two datasets feature a steep increase at high relative humidity however the FT-IR data additionally indicates that the adsorbed water is predominantly of "liquid-like" nature which is in good agreement with the proposed capillary growth (Figure 61) due to ongoing condensation.

## 4.5. Investigations on chemically modified particle ensembles

### 4.5.1. CVD modified particle systems

For this study $SiO_2$ nanoparticle modified QCM quartzes were prepared similar as discussed in section 4.4. However, after the same sequence of ex-situ characterization and combined in-situ FT-IR / QCM-D experiments, samples were modified via CVD route as described in section 3.4.1 using perfluoro-alkylsilanes in order to increase the interface hydrophobicity. Since the aliphatic organosilane backbone featured fluorine as a hetero atom, XPS analysis was employed for confirmation of surface modification. From the spectra presented in Figure 67 it can be seen that a strong fluorine signal is visible both at 686 eV (F 1s) and 841.7 eV (F KLL).

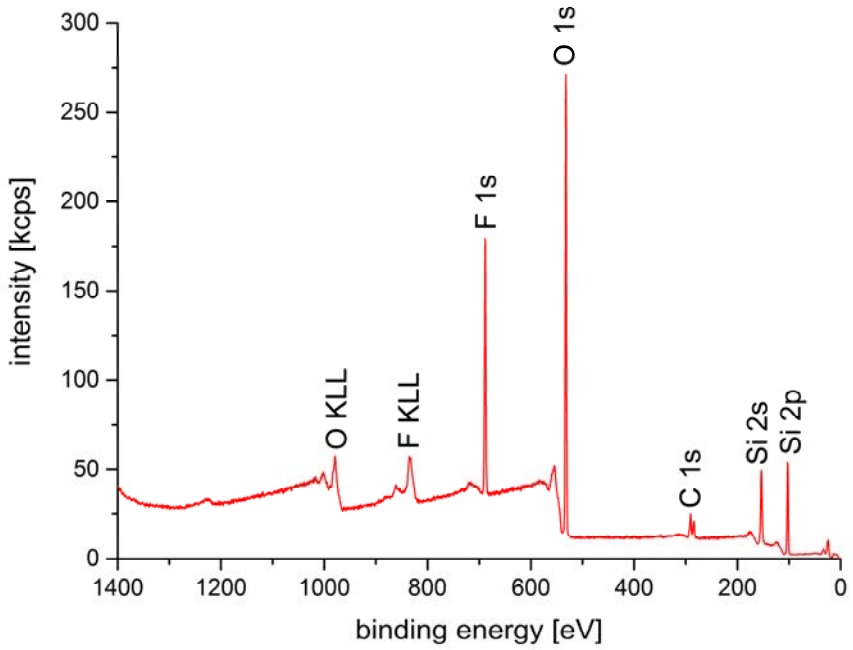


*Figure 67: XPS analysis of $SiO_2$ nanoparticles modified with perflouro-octyl-triethoxy-silane.*

Moreover, due to the intense chemical shift of the C 1s signal induced by the fluorine atoms, a further deconvolution of the carbon signal into aliphatic ($-CH_3$ / $-CH_2$), oxygen rich (-CO-R / -COO) and fluorinated carbon species ($-CF_3$ / $-CF_2$) was possible as depicted in Figure 68.

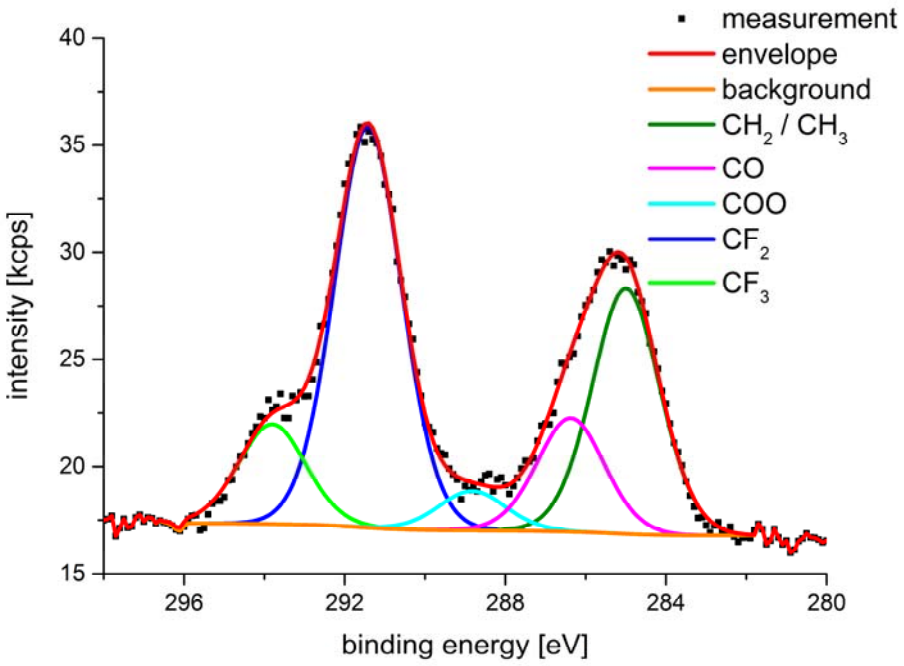


*Figure 68: Deconvolution of C 1s peak of the perflouro-octyl-triethoxy-silane modified $SiO_2$ spheres.*

Corresponding elemental compositions are presented in Table 4.

Table 4: Atomic surface composition of CVD modified $SiO_2$ spheres derived via XPS.

| species | content [at%] |
|---|---|
| O | 41.1 |
| F | 17.7 |
| Si | 29.8 |
| C | 11.4 |

Employing peak deconvolution to the C 1s peak it was possible to identify individual chemical species. Values presented in Table 5 represent fractions of the overall sample composition. Hence the sum of all values in Table 5 equals the overall concentration of carbon in Table 4.

Table 5: Composition of the C 1s peak with respect to the different chemical species.

| species | content [at%] |
|---|---|
| $-CH_x$ | 3.1 |
| -CO-R | 1.4 |
| -COO | 0.5 |
| $-CF_2$ | 5.1 |
| $-CF_3$ | 1.3 |

Furthermore, the change in hydrophilicity was confirmed via static water contact angle measurements. Considering that the water droplet would inevitably affect the nanoparticle arrangement, reference samples have been used for that purpose and the actual quartz crystal was only used for contact angle measurements after the in-situ experiment was finished. Typically, the static contact angle changed from full wetting without modification to ≈100° after the treatment as presented in Figure 69.

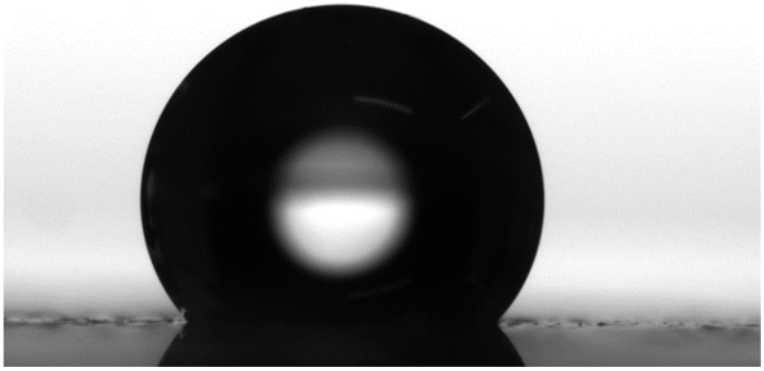

*Figure 69: Static water contact angle on QCM crystal with PE-CVD $SiO_2$ and $SiO_2$ particle layer, modified with long chain organosilane.*

Most interestingly however, a change in water uptake behavior was not observed after surface modification. This was confirmed with adsorption isotherms derived from both QCM (Figure 70) and FT-IR (Figure 71) results.

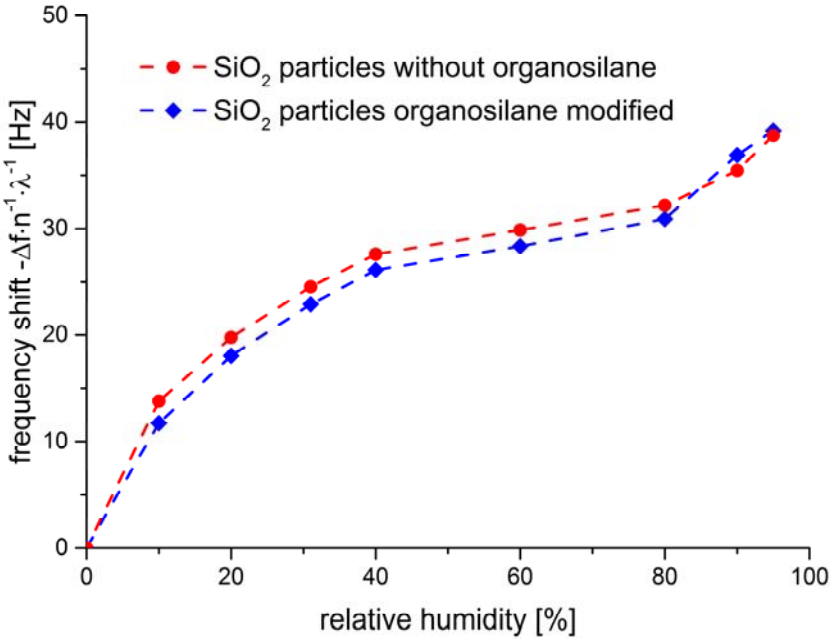


*Figure 70: Water adsorption isotherm derived via QCM-D measurement. Frequency shifts have been corrected for the surface increase factor λ.*

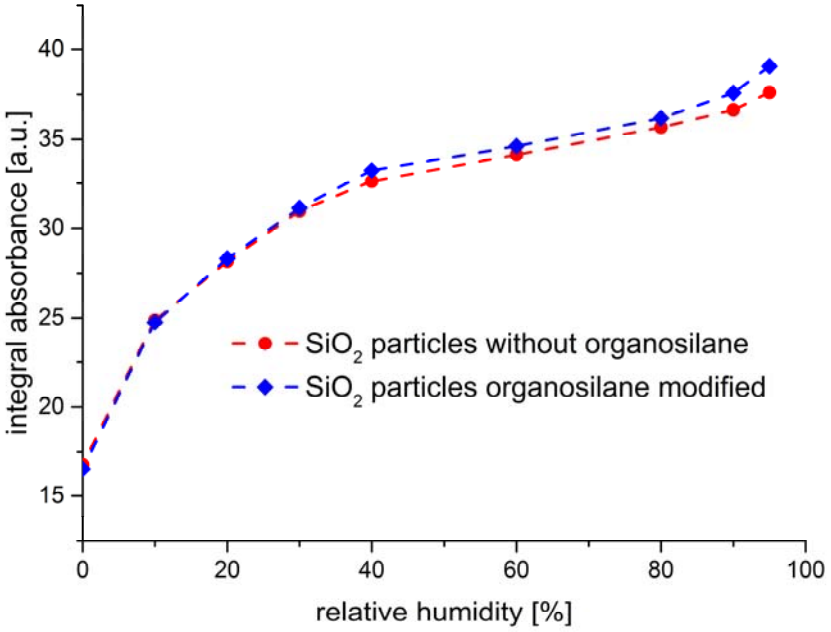


*Figure 71: Adsorption isotherm as derived from the FT-IR data. Presented values represent the peak area under the OH related signal in the region between 3800 $cm^{-1}$ to 2400 $cm^{-1}$ as presented in Figure 64.*

In order to further elucidate this unexpected behavior, additional studies on a more fundamental system were conducted. Smooth PE-CVD $SiO_2$ layers were selected as a model system and analyzed by means of combined FT-IR with variable relative humidity values both with and without similar organosilane thin layer. PE-CVD preparation was performed as discussed in section 3.3.3. However, as the expected signal was much lower than for the particle covered sample, PM-IRRAS was employed. For quantification, the broad peak around 3000 $cm^{-1}$ corresponding to the earlier discussed OH signal (Figure 72) as well as the much smaller peak around 1630 $cm^{-1}$ corresponding to the H-O-H mode (Figure 73) have been integrated.

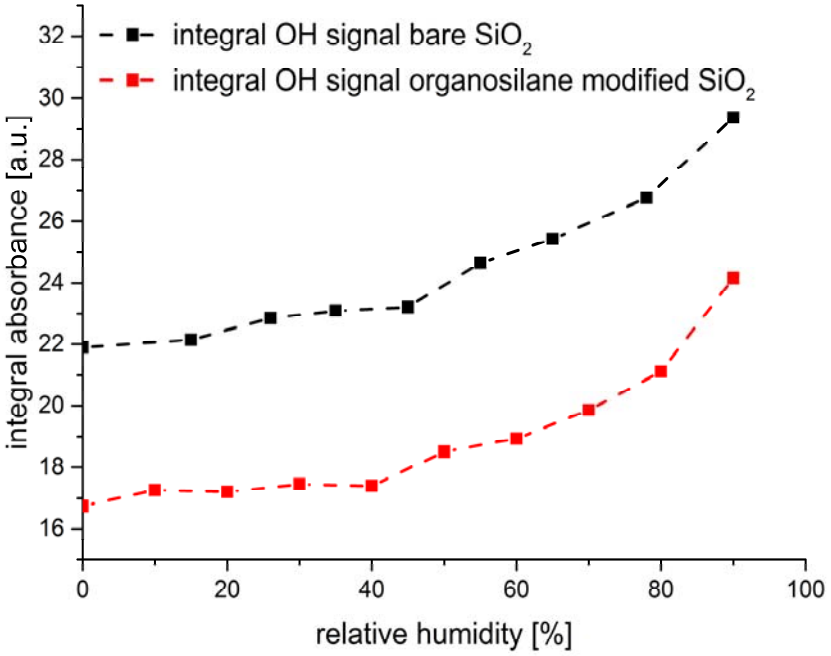


*Figure 72: Evolution of the peak area for the OH-related signal in the region between 3600 $cm^{-1}$ and 3000 $cm^{-1}$.*

From the evolution of the peak area presented in Figure 72, it is evident that the as prepared as well as the organosilane modified sample featured a very similar behavior despite the big difference in wetting angle. Moreover, both curves exhibit a change in slope around 40% to 60% relative humidity which corresponds to the regime of relative humidity where the capillary growth begins to dominate as discussed in section 4.4. The offset between the two curves can be explained by means of the overall smaller number of surface OH-groups due to the partial saturation with organosilane molecules. This assumption is in good agreement with the peak area corresponding to the Si-O-Si signal which was much higher on the modified sample than on the untreated, accounting for the additional Si-O-Si groups due to the bond formation between the substrate and organosilane molecules. In addition, the difference in the peak integral of the H-O-H mode (Figure 73) between both samples is much smaller indicating a similar total uptake of water.

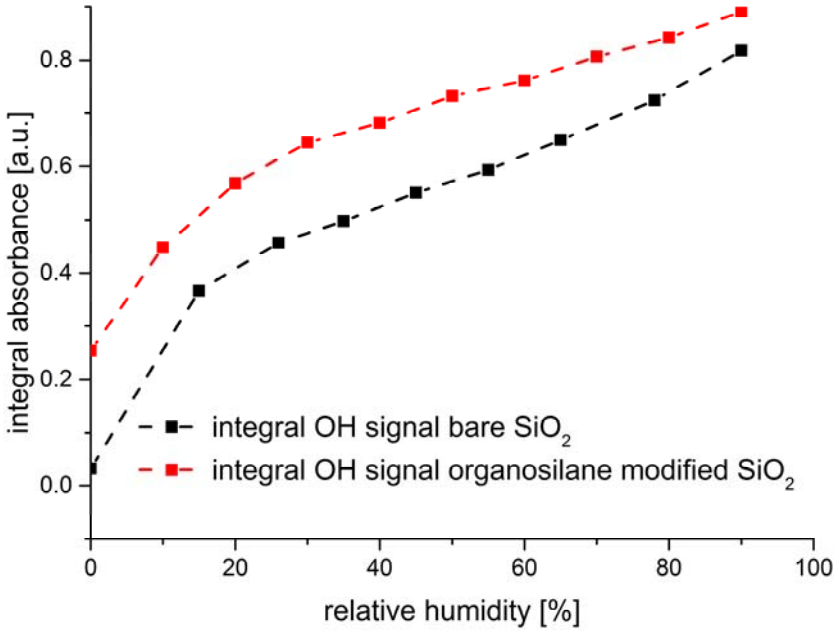


*Figure 73: Evolution of the peak area for the H-O-H related signal around 1630 $cm^{-1}$.*

Interestingly, the actual shape of both sets of curves (Figure 72 and Figure 73) is very different. On the one hand, the OH related signal features only a very shallow increase between 0% and 40% relative humidity and a much steeper increase at higher relative humidity. On the other hand, the H-O-H related signal features a very steep increase in the beginning and almost linear behavior from 20% relative humidity onwards. In a recently published study, Naik et al. [126] found evidence that the commonly discussed model for the organosilane thin film formation as presented in Figure 74-A might be misleading. Instead of every organosilane molecule featuring a covalent bond to the surface, oligomers are being formed which in then are only attached by few groups(Figure 74-B).

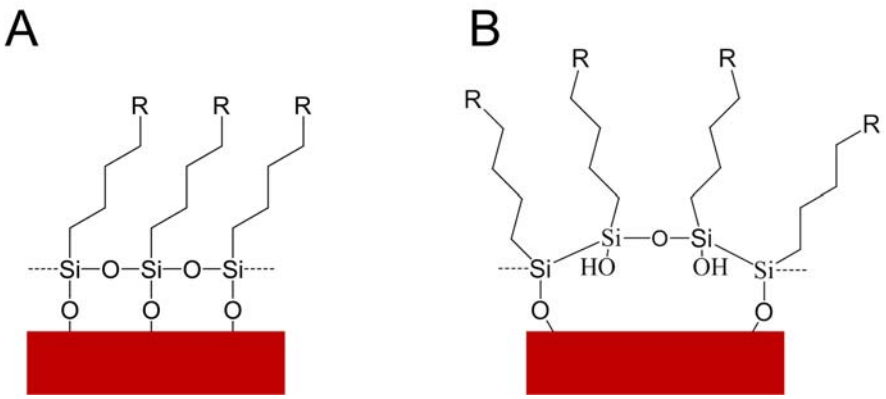


*Figure 74: Schematic of the typically discussed organosilane thin-film structure (A) and the model as proposed by Naik et al. [126].*

Based on this model most of the adsorption sited would be still available for water molecules under the assumption they could penetrate through the hydrophobic layer. This assumption is supported by a publication of Maxisch et al. [127] where a similar behavior for a much more densely packed self-assembled monolayer was found. In his study, it was shown that water molecules were able to penetrate through highly ordered hydrophobic octadecane-phosphonic acid (ODPA) self-assembled monolayers and interact with the underlying substrate. Therefore, they concluded that the barrier properties were almost negligible despite the macroscopically high wetting angles. Hence the same assumption most likely holds true for the system presented in this study as the organosilane layer is typically much less ordered when compared to an ODPA SAM on aluminum.

In this context the steep increase in H-O-H signal can be attributed to the favorable adsorption of water on the mostly unblocked adsorption sited when dosed to the initially dry system. In the second stage, the almost linear increase can be correlated to the absence of particle contact zones and thus the lack of capillary formation. Where in the QCM data obtained from a $SiO_2$ particle sample, a second steep increase was visible around 60% to 80% relative humidity due to the onset of capillary formation, similar effect is missing on the smooth substrate resulting in more linear behavior. Moreover, the much steeper increase in OH related signal might indicate the partial hydrolization of the organosilane substrate bonds at high water activities resulting in a disproportionate increase of OH-groups.

In conclusion, presented experiments on the much simpler model system revealed that the adsorption of an organosilane has negligible influence on the water adsorption on the surfaces due to the special structure of these thin films. However, presented argumentation only explains the behavior of the particle sample at low relative humidity as the actual capillary growth dominating in later stages of the in-situ experiment should be affected by the change in contact angle based on equation (4.9). However, such an effect was not observed during the experiments. In fact, this behavior can also be attributed to the special nature of film morphology as discussed in this section. Taking into account the Kelvin equation (2.11) the capillaries radius of curvature is found to be rather small even at high relative humidity values ($r \approx 10$ nm @ 90% RH) for given particle system when compared to the size of an organosilane agglomerate consisting of a few molecules. Typically, the length of the aliphatic chain ($C_{18}$) is already in the order of magnitude as the allowed capillary radius given by the Kelvin equation.

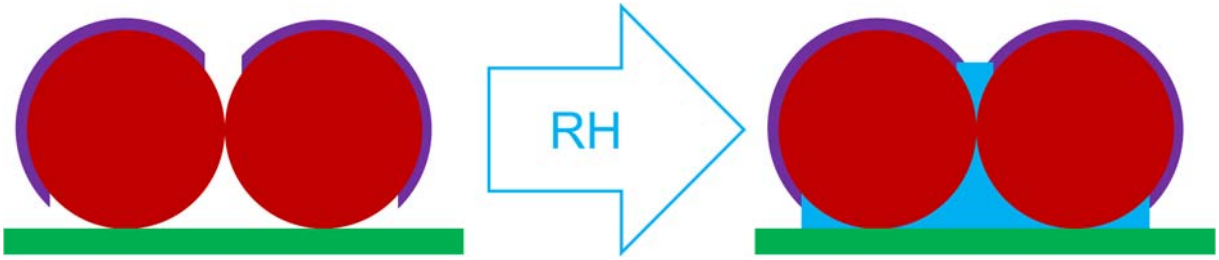


*Figure 75: Schematic of the proposed coverage of the organosilane on the particle modified crystal.*

Hence, is assumed that although most of the surface area is being covered with the organosilane resulting in a high macroscopic contact angle, the actual contact area between two particles might still be unmodified as a result of steric hindrance during adsorption (Figure 75). Therefore, the formation of the capillaries is almost unaffected by the presence of the organosilane molecules despite the high wetting angle.

In the context of these experiments, a more detailed analysis of the Si-O-Si peak stemming from the organosilane substrate bond would shed a light on the film structure. However, such a route was not followed due to the dominating nature of the underlying $SiO_2$ film. Instead, a detailed analysis of the behavior of used organosilanes on an ZnO substrate was performed. Corresponding results are subject of a manuscript which has been submitted to Applied Materials and Interfaces and is currently under review.

In addition to the study of water adsorption on particles with surface polarities modified towards a decreased wettability, a similar study with a modification in opposite direction was performed. However, instead of employing ex-situ CVD based methods for the particle interface modification, an in-situ approach based on UV-light induced hydrophilization of $TiO_2$ surfaces was chosen. Corresponding results are discussed in the subsequent section

### 4.5.2. UV-light modified particle system

#### 4.5.2.1. DRIFTS study on $TiO_2$ anatase nanoparticle modification via UV-light

In preparation of the in-situ experiments presented in the subsequent chapter, DRIFT spectroscopy based investigations of the activation and decay of anatase nanoparticle powder under the influence of UV-light have been performed. Received spectra as presented in Figure 76 indicate a strong increase of surface hydroxyl groups and a simultaneous decrease of carbon related species upon the irradiation with UV-light.

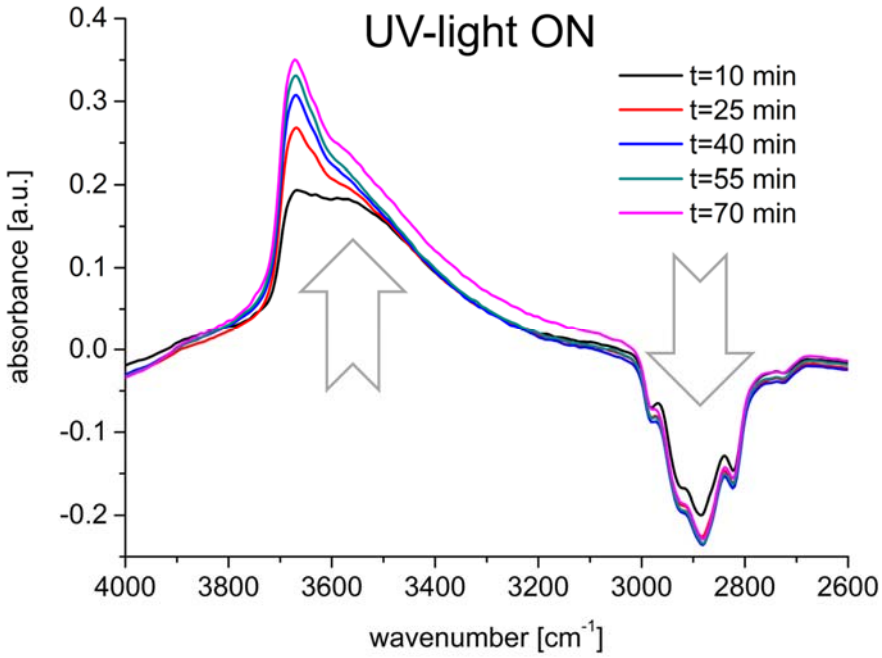


*Figure 76: DRIFT spectroscopy of the $TiO_2$ activation induced by irradiation with UV-light. Presented spectra have been referenced with respect to the as received particle powder.*

Presented process reached saturation after roughly 70 minutes of UV-light exposure. Most interestingly, the highly asymmetric OH related signal around 3500 $cm^{-1}$ features a maximum around 3650 $cm^{-1}$ characteristic for the so called free OH-groups as discussed in section 4.4.2. This finding is in excellent agreement with the proposed mechanism for the UV-light induced hydrophilization based on the dissociative adsorption of water on oxygen vacancy sites resulting in the formation of additional surface hydroxyl groups [65-68]. In contrast to the increase of the OH related signal, the $-CH_2$ and $-CH_3$ related signal decreased almost instantaneously indicating a very fast photo-oxidation of the adsorbate layer originating from ambient atmosphere. Subsequent study of the decay process indicated an initially very quick decrease of the free OH-groups.

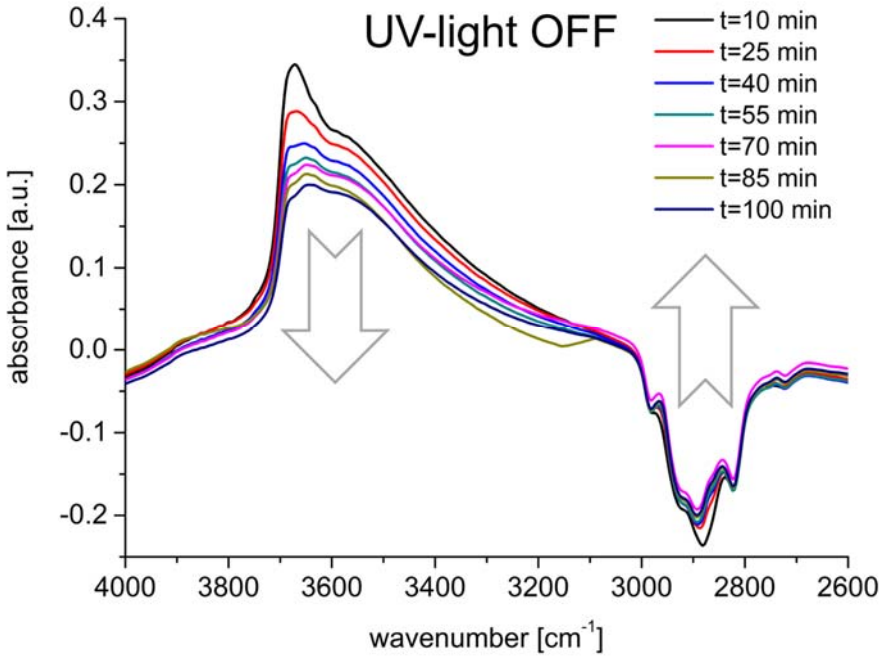


*Figure 77: DRIFT spectroscopy of the decay after UV-light irradiation was stopped. Presented spectra have been referenced with respect to the as received particle powder.*

It appears that the decay (Figure 77) obeys an exponential behavior with quick slowdown of free OH reduction after stopping the UV-light exposure. Moreover, only a very limited amount of recontamination of the particles could be observed due to the clean conditions of the surrounding atmosphere within the spectrometer. However, with respect to the combined FT-IR / QCM-D experiments presented in the subsequent section, it could be concluded that the initial decay reaction is fast in case of the very reactive free OH-groups which has to be taken into account.

#### 4.5.2.2. In-situ FT-IR / QCM study of water adsorption on $TiO_2$ NP under UV-light

Investigations on the influence of UV-light on the water adsorption was studied on $TiO_2$ nanoparticles prepared by the method described in section 3.1. In contrast to the studies on $SiO_2$ particles discussed in previous sections, these particles were deposited on the quartz crystal substrates via electrophoresis (section 3.2.2) since corresponding PE-CVD $TiO_2$ film with the highly UV-light active anatase crystal phase were not available. Unfortunately, received particle films were much less defined than the films containing the $SiO_2$ nanoparticles. Corresponding FE-SEM analysis revealed a film consisting of particle aggregates exhibiting an island like structure as depicted in Figure 78.

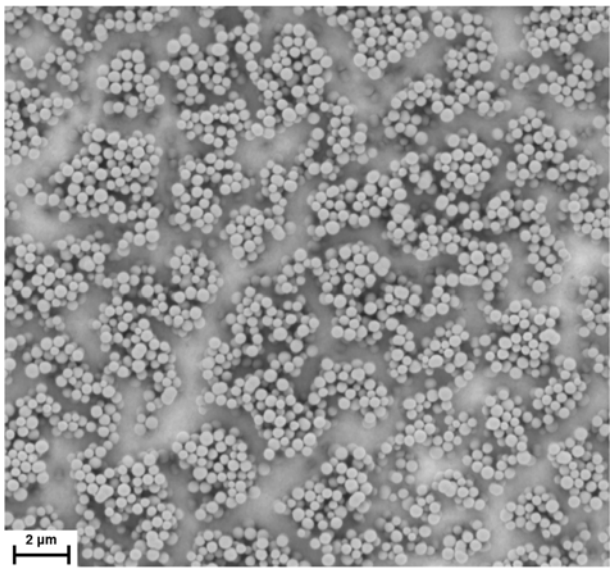


*Figure 78: FE-SEM image of $TiO_2$ nanoparticles deposited via electrophoresis on QCM crystal substrate.*

Initially, a basic experiment was performed for the study of the interplay between UV-light and the water adsorption. QCM results depicted in Figure 79 show an experiment where upon the stabilization of the crystal in dry conditions, UV-light was dosed with an average intensity of 50 $mW \cdot cm^{-2}$ resulting in a steep positive frequency shift attributed to the thermal energy supplied to the quartz crystal.

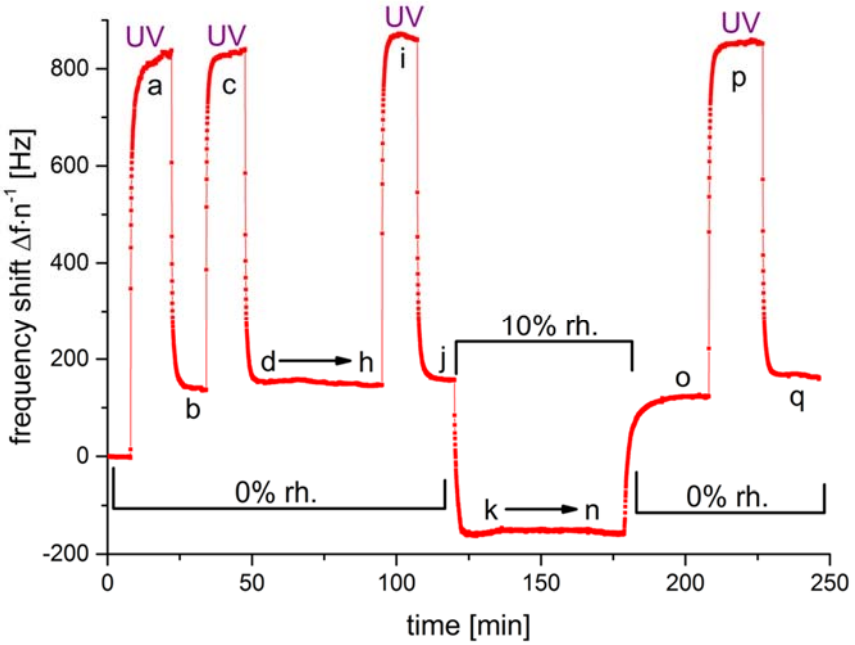


*Figure 79: QCM frequency shift of multistep UV-light irradiation experiment on immobilized $TiO_2$ nanoparticles.*

After 10 minutes of irradiation the UV-lamp was shut off and the quartz was allowed to stabilize on a new plateau (b) corresponding to a positive frequency shift of ≈140 Hz which is attributed to the desorption of adsorbate species and water present in the initial state. Subsequent repetition of the UV-light exposure (10 minutes) led only to a slightly higher positive shift of ≈151 Hz (d→h) indicating that the desorption process did not fully reach saturation within the initial UV-light dose. Subsequent third UV-light exposure led to a shift comparable to the second dose indicating that the desorption process was finished after the second irradiation step. Corresponding FT-IR spectra presented in Figure 80 to Figure 83 are referenced based on an initial spectrum of the immobilized particles measured at t=0 in Figure 79. Hence, only relative changes of the particles due to the irradiation with UV-light or the dosing or humidity in later stages of the experiment are visible.

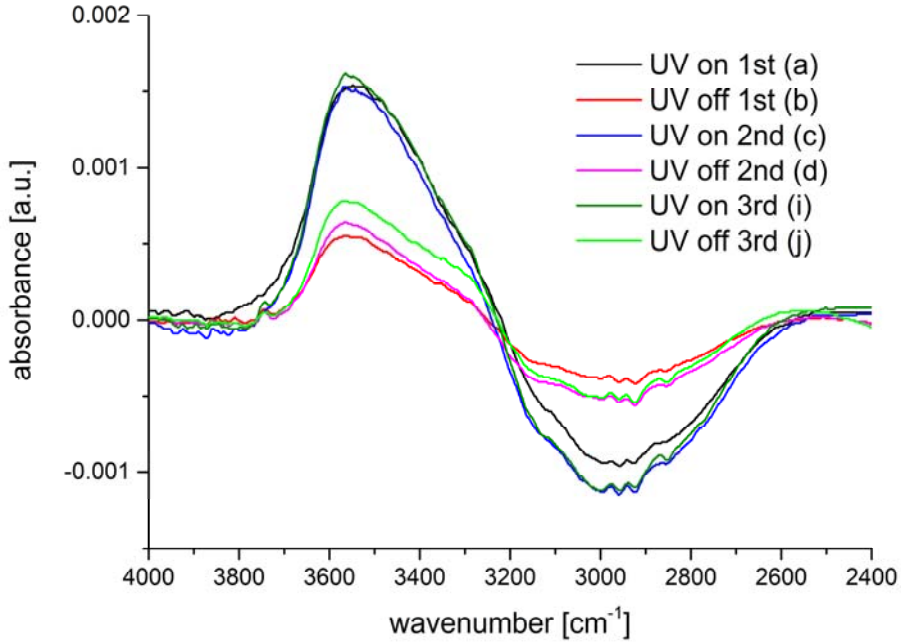


*Figure 80: FT-IR spectra of $TiO_2$ nanoparticles during ongoing and after UV-light irradiation. Indicated letters a-j correspond to time of acquisition denoted in Figure 79.*

Acquired spectra presented in Figure 80 indicate that two processes were induced by the irradiation with UV-light. It was found that, a positive contribution around 3550 $cm^{-1}$ hinted towards the formation of surface bound OH-groups due to the photo-induced dissociation of water. Likewise, a negative contribution around ≈3000 $cm^{-1}$ indicates the desorption and removal of water from the system. Furthermore, it can be noted that the decrease of this peak after both the second and third UV-light dose is identical and slightly higher than after the initial UV-light treatment which is in good agreement with the corresponding QCM results. A similar trend is also visible in the spectra acquired during ongoing irradiation which exhibit an identical decrease at ≈3000 $cm^{-1}$ during the second and third UV-light dose which again is slightly higher than during the initial irradiation phase. Furthermore, it is clearly visible that the increase of surface bound OH as well as the decrease of water in the system immediately relaxes upon interruption of the UV-light. In order to further study this relaxation process, subsequent spectra were acquired between the second and third UV-light dose (Figure 79 d-h).

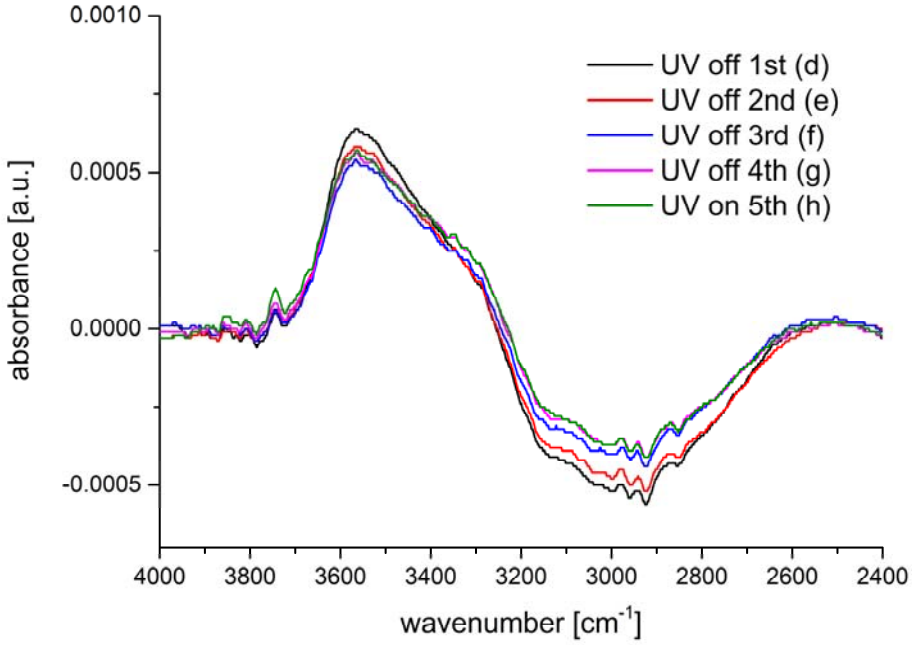


*Figure 81: FT-IR spectra acquired between 2nd and 3rd UV-light dose as presented in Figure 79 d → h.*

Time resolved measurements presented in Figure 81 suggest that the relaxation is rather slow after the initial abrupt decrease due to the interruption of the UV-light and reached an almost constant condition after 30 min (4$^{th}$ measurement). This finding is in good agreement with the ex-situ DRIFTS data presented in Figure 76 which also suggested a considerable decline of the relaxation around 40 minutes.

After the initial study of the excitation process, the relative humidity within the cell was increased to 10%, immediately resulting in a steep negative frequency shift of about 150 Hz with respect to the initial state of the system (t=0). However, with respect to the plateau right after UV-light irradiation (Figure 79-j) this would equal a total shift of ≈-300 Hz. Unfortunately, a more detailed analysis of the frequency shift with respect to capillary volume and contact mechanics could not be employed due to the much more complex and less defined film morphology. Analogous to the study of the relaxation process, several subsequent FT-IR spectra were acquired during the presence of humidity which are presented in Figure 82. In addition to the referencing of the acquired single channel spectra based on the initial state of the particles, additional post-processing was employed to remove the contribution of water being adsorbed on the ZnSe windows. For this purpose, a similar method as described earlier in this chapter was employed. After the measurement of the particle specimen, a super hydrophobic ODT SAM covered quartz crystal was measured both at 0% and 10% relative humidity respectively. Resulting difference spectrum (10% RH spectrum divided by 0% RH

spectrum) accounted for the water in the gas phase as well as the water being adsorbed on the ZnSe windows. Thus, in order to correct the particle spectra, mentioned spectrum has been subtracted from all particle spectra acquired at 10% relative humidity.

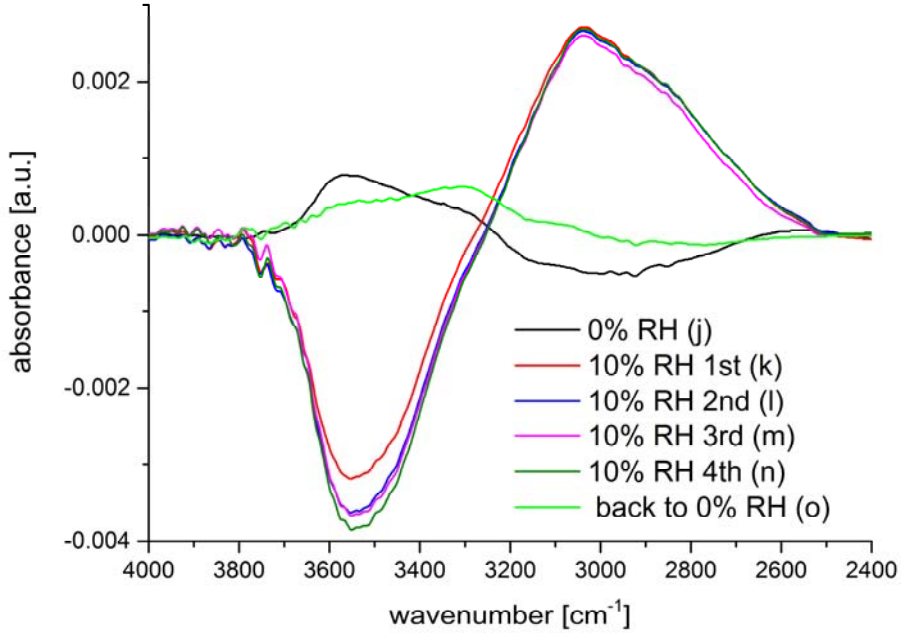


*Figure 82: FT-IR spectra acquired right before (j), during (k-n) and shortly after (o) the dosing of humidity to the system as presented in Figure 79 j → o.*

Presented spectra exhibit a drastic change upon the introduction of humidity indicating the adsorption of "liquid" like water at the expense of the free surface hydroxyl groups as a result of the saturation with an adsorbed water layer. Time resolved spectra show that the process quickly reached saturation between (k) and (l) (Figure 79). Removal of the humidity via purging with dry gas led to a structure with a rather diffuse and less pronounced peak indicating a small deviation from the initial reference spectrum. This stands in clear contradiction to the corresponding QCM data which still features a clear positive shift of ≈120 Hz with respect to the initial state indicating the overall loss of mass from the system which based on the FT-IR data is not accounted for by water only. At this point the only explanation for this behavior is the permanent desorption of carbon species during the initial UV-light irradiation and the possible change of film morphology as a result of the water leading to changes in the particle crystal contact mechanics.

In a final step, the dried specimen was again exposed to UV-light leading to the desorption of previously chemisorbed water species as indicated by a positive QCM shift of about 48 Hz with respect to the plateau at (o). This is further supported by comparison of the FT-IR data acquired at (j) and (q) presented in Figure 83.

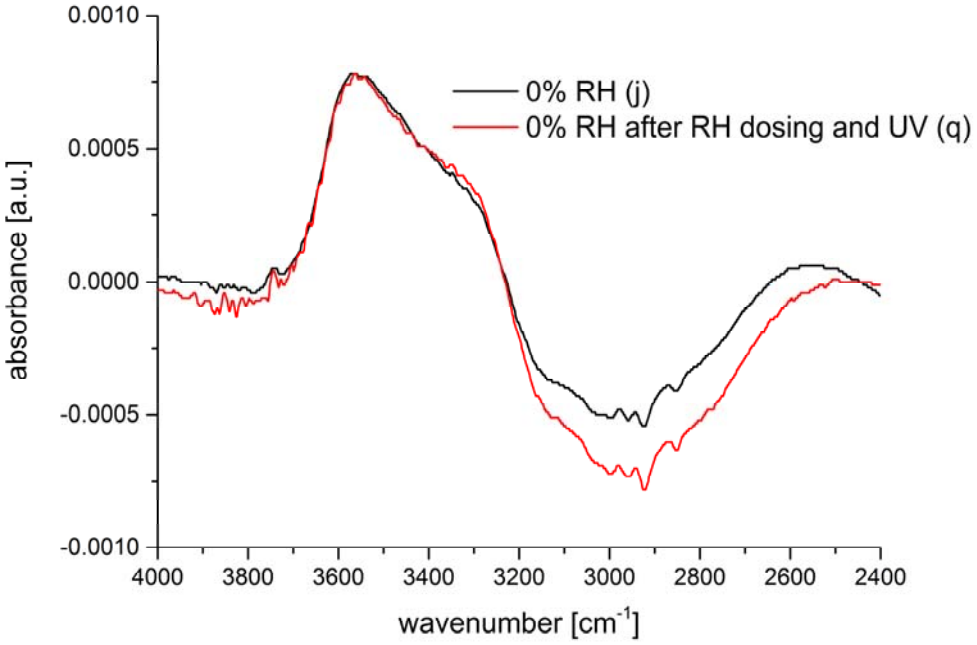


*Figure 83: FT-IR data of $TiO_2$ nanoparticles after UV-light treatment before (j) and after (q) water adsorption experiment. Indicated letters j and q correspond to time of acquisition denoted in Figure 79.*

Presented spectra reveal that the surface OH species was fully restored during UV-light irradiation, and only a minor change of the contribution accounting for water occurred comparing both FT-IR datasets. This finding is in good agreement with the overall small frequency shift between (j) and (q).

To further elucidate the interplay between the UV-light driven activation and water adsorption four consecutive experiments were performed with the identical sample. First, a water adsorption experiment similar to the experiments in section 4.4.1 was performed without the influence of UV-light to establish a reference. Second, the experiment was repeated with an irradiation step before and after the adsorption measurements. The third experiment consisted of ongoing UV-light irradiation while dosing humidity in order to diminish the effect of relaxation during the adsorption experiment. However, the permanent supply of energy to the system had to be kept in mind. Therefore, the fourth experiment consisted of a short UV-light activation phase before every humid gas dosing step in order to “reset” the interface chemistry and establish a quasi-equal interface for every humidity level. During all four experiments the

particle equipped quartzes were equilibrated in dry atmosphere. During the experiment, the relative humidity was stepwise changed from:

0% → 10% → 20% → 30% → 40% → 60% → 80% → 90% → 95% → 98% → 0%.

Figure 84 shows the QCM data of the first two experiments. For the experiment with the predeceasing UV-light activation step, the frequency right after stopping the UV-light exposure was chosen as reference state. From Figure 84 it is evident that the shifts observed during the experiment without UV-light activation (black curve) were generally smaller when compared to the shifts of the experiment with UV-light activation. This result is in good agreement with both the proposed hydrophilization of the particle surfaces and the freeing of adsorption sites due to the UV-light induced oxidation of native adsorbates.

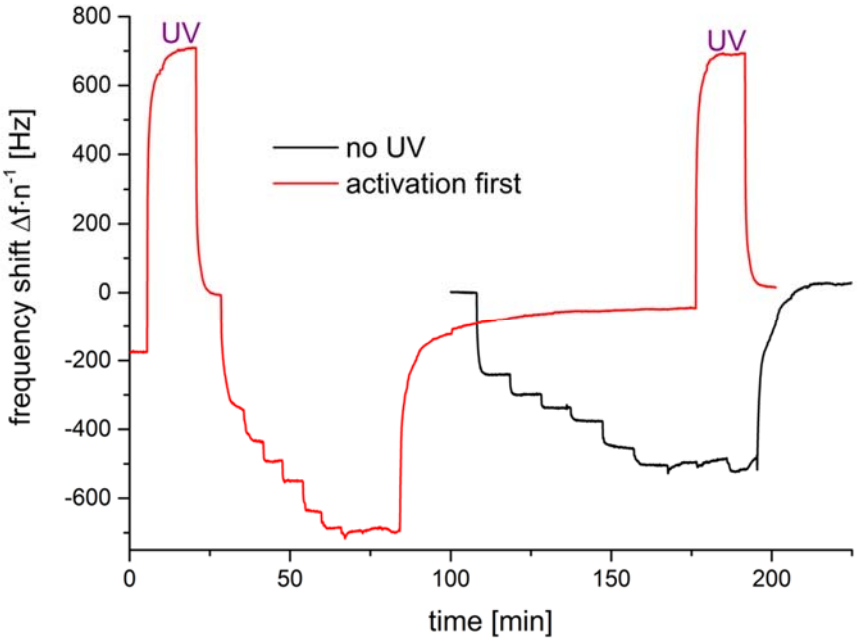


*Figure 84: QCM data for the water adsorption on anatase nanoparticles without UV-light (black) and with an initial activation phase (red). The black curve has been shifted on the x axis for better visibility.*

However, it has to be kept in mind that the actual water adsorption experiment with preceding UV-light activation could possibly be affected by the ongoing relaxation of the activated surface.

Results of the third experiment featuring the water adsorption during ongoing UV-light irradiation presented in Figure 85 suggested a similar trend as preceding experiments. In this case, the initial plateau at 0% relative humidity and ongoing UV-light irradiation was set as reference state. As evident from Figure 85, observed shifts were generally smaller compared to the experiment with initial activation as well as without any activation (Figure 84). This

behavior is attributed to two competing processes. The ongoing UV-light irradiation kept the surface very hydrophilic and effectively prevented any relaxation. On the contrary, the permanent energy input resulted in heat which as a consequence lowered the effective relative humidity within the cell and at the same time induced a thermal desorption of water from the surface.

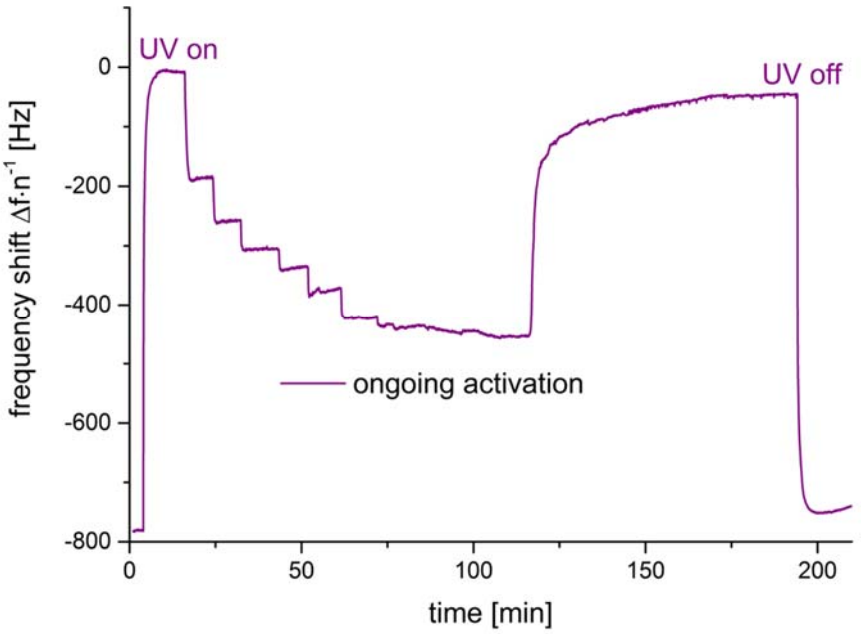


*Figure 85: QCM data for the water adsorption on anatase nanoparticles during ongoing UV-light irradiation.*

In order to overcome the limitations of the two experiments featuring the UV-light activation, the fourth experiment was designed in such a fashion that neither the heat supplied by the UV-lamp nor the relaxation process should influence the water uptake. Therefore, the specimen was subsequently cycled through a sequence of:

0% RH → UV-light on → UV-light off → X% RH →0% RH

With identical values for X as during the previous experiments. For the corresponding dataset presented in Figure 86 the frequency right after an activation step and prior to the dosing of humidity was chosen as reference state.

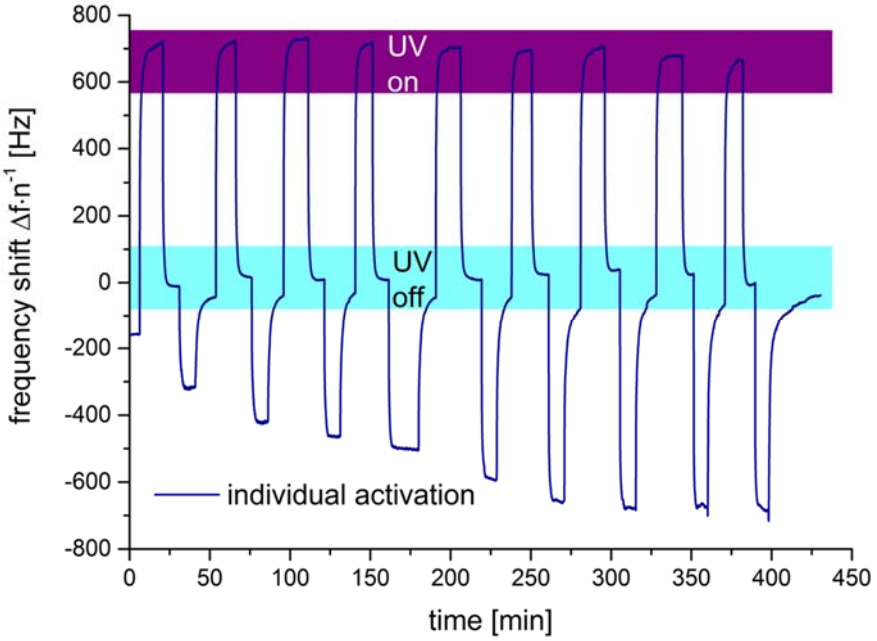


*Figure 86: QCM data for the water adsorption on anatase nanoparticles with individual activation phases before each humidity change.*

Presented data exhibits shifts very comparable to the shifts observed during the experiment with only one initial activation step at each given relative humidity level. For better comparability adsorption isotherms have been derived for all four experiments which are presented in Figure 87.

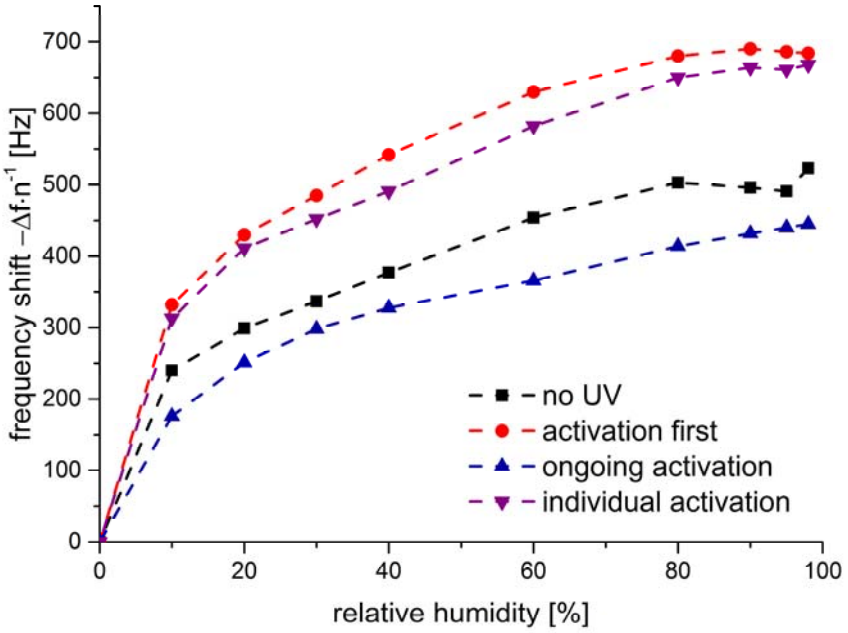


*Figure 87: Adsorption isotherms derived from all four water adsorption experiments.*

From this plot it can be seen that the water uptake during the experiment with ongoing UV-light irradiation was lowest indicating that the heat induced desorption dominated. In

contrast to that, during both experiments with intermitted UV-light irradiation the water uptake was considerably higher than on the non-activated particles which is in good agreement with the initial assumption of the interface hydrophilization. Moreover, both the experiment with a single activation step and the experiment with the individual excitation phases behave very comparable. The slight offset can again be attributed to the accumulation of heat in the latter experiment due to the numerous UV-light irradiation phases. In this context it is noteworthy that the shape of the adsorption isotherms deviates from the corresponding isotherms found on the $SiO_2$ particles at high relative humidity values (Figure 59). This behavior indicates that the capillary formation plays an inferior role in this system which might be attributed to the very different particle film morphology featuring less particle-particle contacts as well as the rather hydrophobic nature of the gold substrate in comparison to the PE-$SiO_2$ layer in the previous experiments.

## 4.6. Conclusions

A new in-situ analytical experimental setup combining FT-IR reflection absorption spectroscopy and QCM-D was established for the investigation of water adsorption and capillary bridge formation in nano- and micro-particle layers. The comparison of the water adsorption isotherms for $SiO_2$ nanoparticle layers with a smooth $SiO_2$-like thin film allowed for the analysis of particle induced water layer formation in the contact regions.

It was shown that at low relative humidity, only a single monolayer of water is adsorbed at the surface that gives rise to free OH-bonds of the water molecules and/or the surface silanol groups. In contrast, at high humidity, the first two monolayers of water are oriented similar to the water/air interface, which entails the occurrence of the "ice-like" peaks in the FT-IR spectrum. Moreover, the comparison of the FT-IR and QCM-D data indicated a clear transition from an adsorbed layer to capillary bridges.

This finding was supported by the corresponding dissipation data exhibiting a local maximum at between 60% and 80% relative humidity indicating a decrease in contact force due to the growth of capillaries in agreement to former studies by Johannsmann et al. [95].

Moreover, the detailed analysis of the water adsorption on chemically modified systems reveled that despite a macroscopic change of wetting induced by greatly altered surface chemistry, the water adsorption was almost unchanged. However, the detailed analysis of a suitable model system revealed that the observed effect could be attributed to the special structure of the organosilane films employed for the modification of the particle chemistry.

In addition to the experiments performed on $SiO_2$ based system, proposed method proved to be a powerful tool for the study of UV-light induced changes of surface chemistry on $TiO_2$ nanoparticles and the correlated changes of water absorption properties. It could be shown that activated surfaces exhibited a greatly increased number of surface bound OH-groups facilitating a much higher water uptake when compared to the corresponding relaxed state.

The presented results illustrate that the combination of in-situ FT-IR and QCM-D facilitates the qualitative and quantitative analysis of water adsorption and capillary bridge formation in particle layers on multifarious and partially very complex particle systems.

# 5. In-situ AFM study of inter-particle forces in humid environments

## 5.1. Scientific approach

Experiments presented in this chapter focus on the measurement of the contact force between individual particles via AFM based force distance spectroscopy under environmental conditions. The key idea behind this approach is that most other analytical methods, like the shear testing for example, rely on probing bulk properties representing an average of many contact events in order to derive the contact force on a single particle basis. On the contrary, AFM features the unique advantage of being capable to directly measure the actual forces present between two individual nanoscale objects as a function of various parameters as depicted in Figure 88.

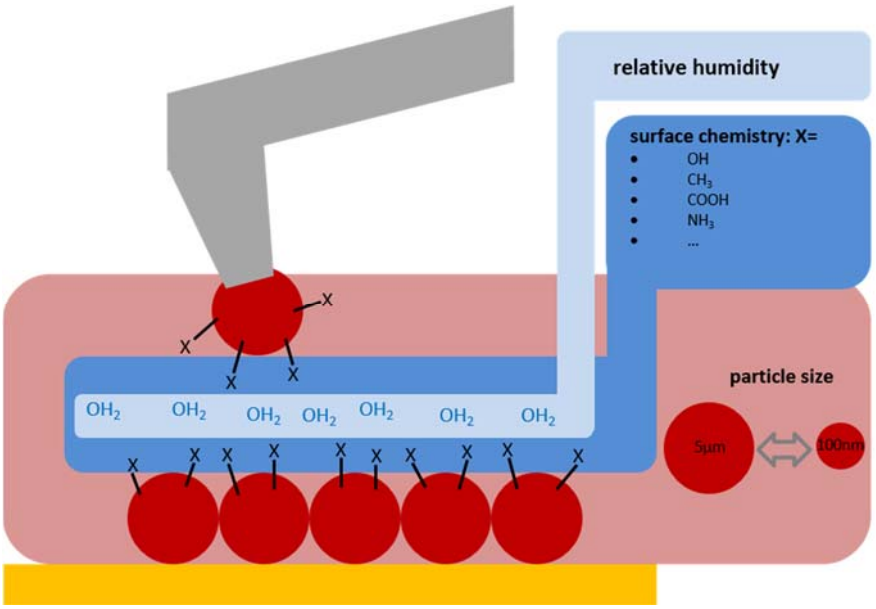


*Figure 88: Schematic of the parameters of interest for the in-situ AFM based approach.*

In this context, the only simplification which was made to the system was the transition from a particle-particle contact to a particle-wall contact. However, as discussed in great detail in section 2.5., corresponding forces could be directly correlated to a corresponding particle-particle contact.

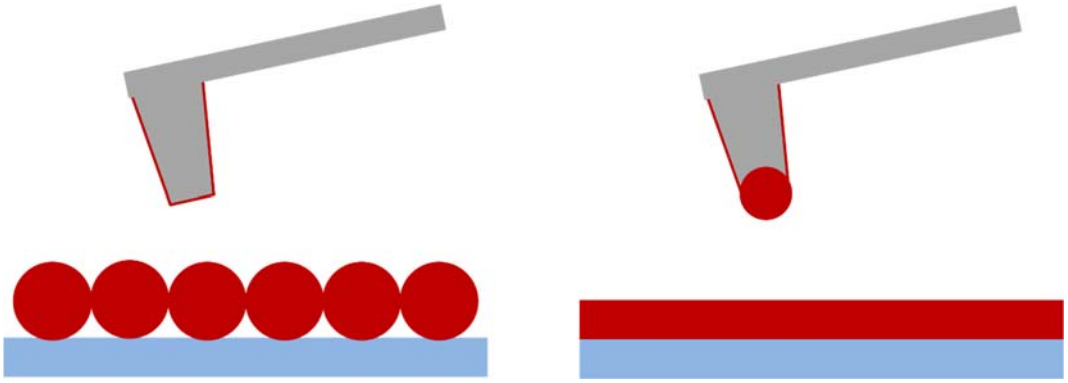

*Figure 89: Schematic of the two approaches planned, both resembling a particle wall contact.*

Planned experiments consisted of contact force measurements by means of force distance mappings between either a layer of immobilized particles and a micro-plateau shaped tip, or a smooth substrate and a particle-shaped probe with both resembling a nanosized particle wall contact, as can be seen on Figure 89. Subsequently, an external stimulus (humidity, UV-light) was changed and the measurement were repeated to study the resulting effect.

## 5.2. Development of experimental setup

In order to shed some light on the influence of environmental factors on the inter-particle force, a new experimental setup was designed allowing for the variation of gas composition as well as UV-light irradiation during ongoing AFM experiments. First, a special sample holder was developed allowing for the in-situ illumination of the sample via UV-light. Second, a new atmospheric chamber was designed allowing for the control of gas composition during force spectroscopy measurements.

Since most of the AFMs available featured only a small gap between the scanner and the sample, illumination from top was not feasible. Hence, a new approach with the illumination of the sample from underneath through a UV-light transparent substrate was chosen. A schematic of the corresponding holder is depicted in Figure 90.

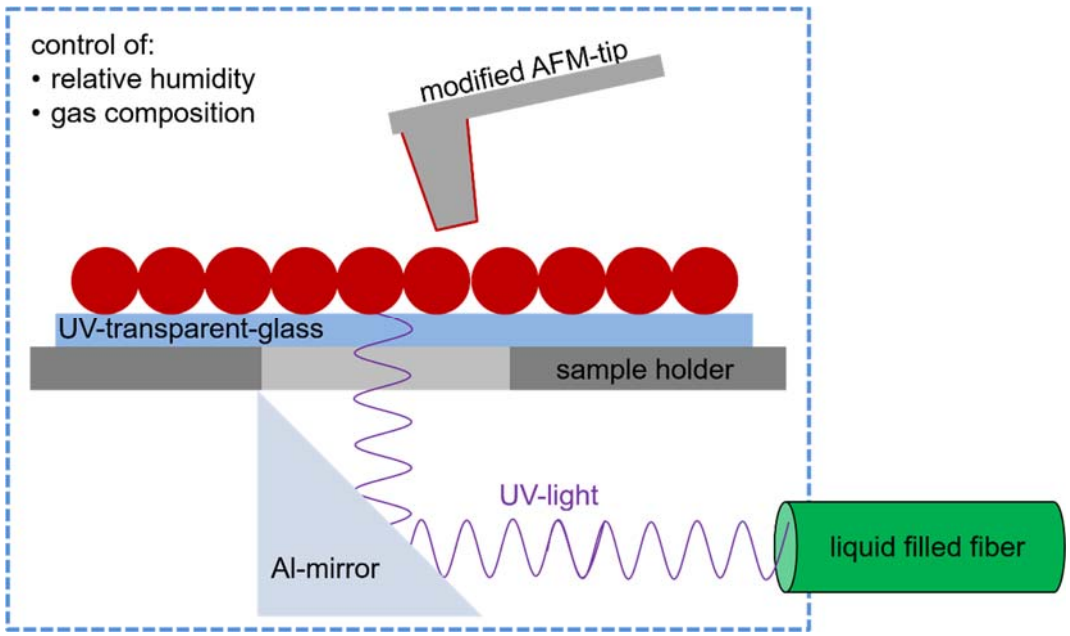


*Figure 90: Schematic of the new sample holder for the in-situ UV-light irradiation of the specimen.*

Presented holder features an aluminum mirror reflecting the supplied UV-light to the substrate. However, in order for the UV-light to reach the probed surface, the specimen was immobilized on a highly UV-light transparent fused silica substrate. Moreover, the sample thickness had to be very small in order to prevent the total absorption of the supplied UV-light within the sample layer before reaching the sample interface.

In addition to the new sample holder, a custom designed environmental chamber was manufactured facilitating the supply of UV-light to the mentioned Al mirror as well as the control of the gas composition.

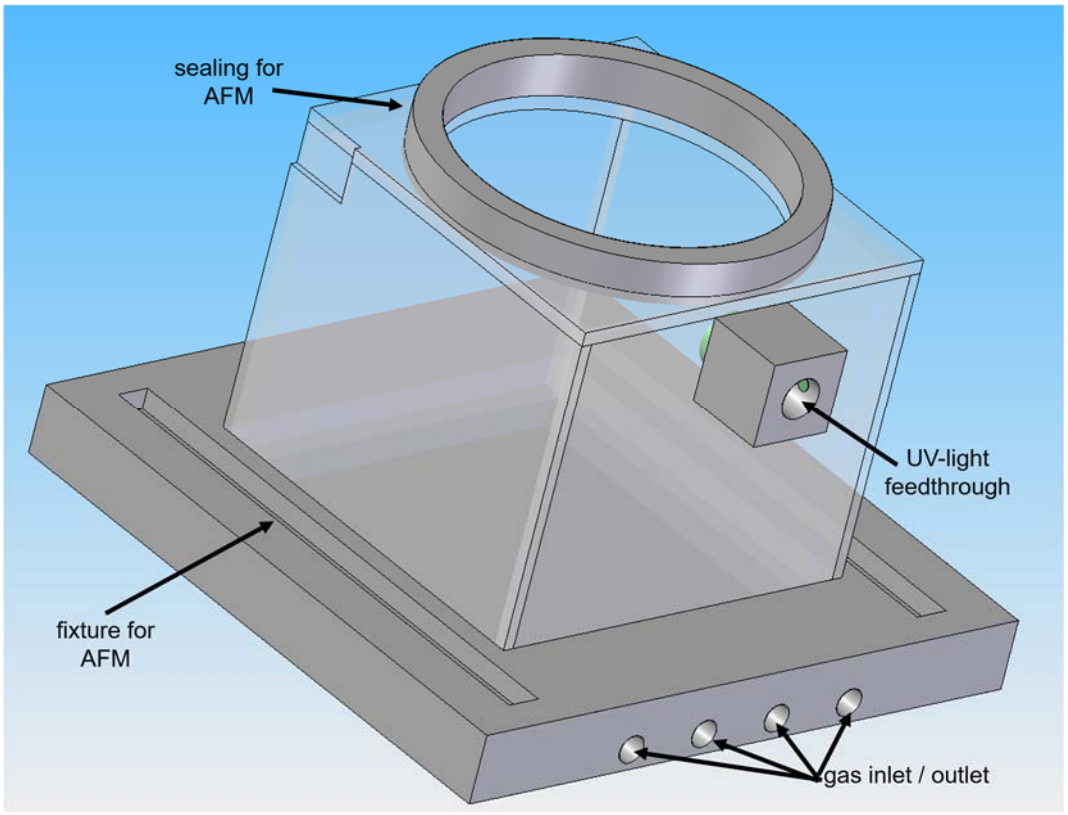


*Figure 91: Schematic of the new environmental chamber for the Agilent 5500 AFM.*

Presented cell (Figure 91) features a solid aluminum base equipped with an polymethyl-methacrylate housing containing the atmosphere and shielding most of the UV-light. The cell was attached to the humid air generator presented in Figure 49 where a humidity sensor was placed within the cell in close proximity to the specimen. During a typical experiment, the cell was constantly purged with nitrogen containing the desired amount of humidity. The AFM assembly was placed on top of the cell with the magnetically connected sample holder reaching into the cells volume.

## 5.3. Cantilever preparation

### 5.3.1. Preparation nano-plateau Cantilever

For the preparation of AFM tips featuring a nanosized plateau, two approaches were followed. In the first method, AFM-tips were cut by means of focused ion beam (FIB) using a gallium source whereas in the second route, AFM-tips were grinded against an RCA-1 cleaned $SiO_2$ covered Si wafer. Cantilevers used typically featured a force constant of 0.63 $Nm^{-1}$. Although the FIB based approach allowed to cut the tips in a very controlled fashion, the inevitable implantation of gallium atoms to the cut edge had to be considered. Therefore, cut tips were subsequently coated with an ultra-smooth $SiO_2$ plasma polymer via PE-CVD route as presented in section 3.3.3 effectively reestablishing a clean surface of known chemistry. The second and certainly more straightforward approach utilized an AFM, scanning the tip against a clean wafer at high loads. Once the force exerted on the tip passed a certain threshold value, abrasion occurred creating a plateau with a size proportional to the scan time and pressure applied.

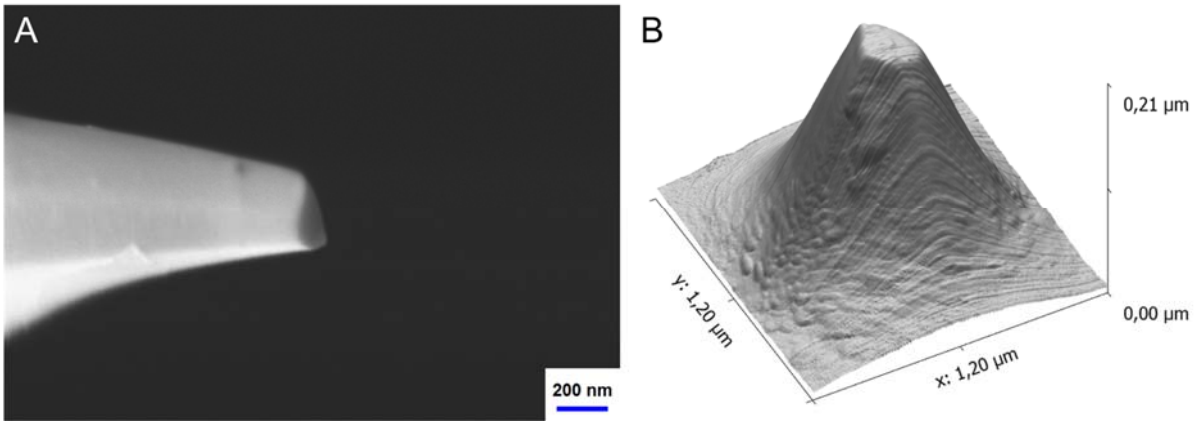


*Figure 92: FE-SEM image of a FIB cut cantilever featuring a plateau with a diameter of approximately ≈300 nm (A). Topography image of a grinded tip measured by means of inverse tip imaging (B). Plateau diameter was found to be ≈280 nm.*

Every tip prepared by either of these methods was individually characterized by means of inverse imaging using an inverse tip sample to determine the actual plateau dimensions (Figure 92-B) as well as FE-SEM (Figure 92-A). In contrast to the FIB based approach, the grinding method avoided the incorporation of hetero atoms and featured a native $SiO_2$ oxide which formed spontaneously under atmospheric conditions.

### 5.3.2. Preparation of nano-spherical tips via annealing method

Nanosized colloidal probes were prepared by an annealing method similar to the procedure proposed by Huttl et al. [128]. Briefly, as received Si based cantilevers were initially cleaned by means of RCA-1 cleaning. Subsequently, cleaned probes were annealed at 1150 °C for approximately 1 h under ambient atmosphere resulting in a blunt tip with spherical geometry and a typical diameter of ≈300 nm as characterized by high resolution FE-SEM (Figure 93).

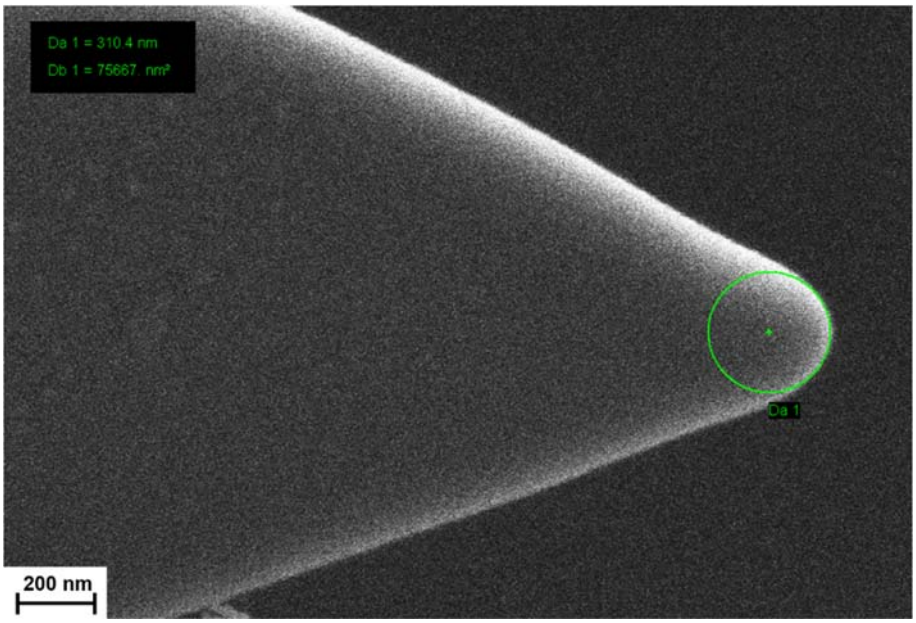


*Figure 93: High resolution FE-SEM image of an annealed AFM tip featuring a diameter of 310 nm.*

Depending on the type of experiment to be conducted, annealed tips were coated with $TiO_2$ via ALD method as described in section 3.4.2. In the case of an ALD coating, a second annealing step at lower temperatures (≈500 °C) was employed in order to trigger the crystallization process of the ALD layer from its amorphous state to a crystalline anatase phase. However, as the temperature during the second annealing step was found to be much lower, no further change of tip geometry was observed.

### 5.3.3. Preparation of colloidal probes via gluing method.

For the preparation of colloidal probes, $TiO_2$ anatase nanoparticles prepared via sol-gel route as described in section 3.1, featuring an average diameter of ≈1.5 µm were spread on a glass slide. In addition, a small droplet of a commercial available two component epoxy resin (UHU Plus Endfest 300) was placed on a particle free region on the same glass slide.

A silicon chip featuring at least two tipless cantilevers was mounted on a custom designed holder which was fixed to a hydraulic driven micromanipulator equipped with an inverted microscope.

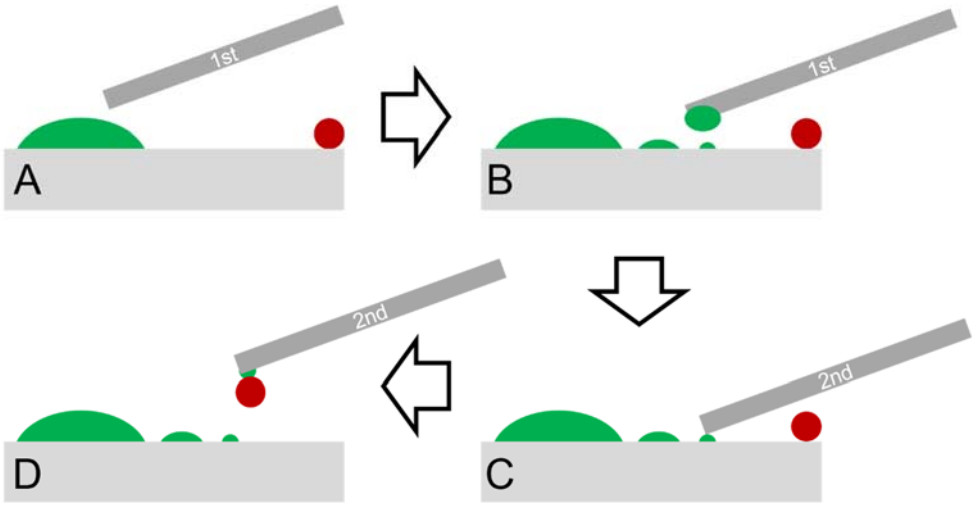


*Figure 94: Schematic of the gluing (green) process of colloidal probes using the synthetized $TiO_2$ particles.*

The very delicate gluing process consisted of three steps, initially one of the cantilevers was sacrificed in order to generate micron sized glue drops. Therefore, the cantilever was fully immersed into the macroscopic drop in order become loaded with glue (Figure 94-A). In analogy to a classic pen, the cantilever was subsequently brought into contact with a clean area of the glass slide effectively generating small glue drop with decreasing size (Figure 94-B). After a drop size of ≈1 µm was reached, the clean cantilever was brought into contact wetting it with a small amount of the resin (Figure 94-C).

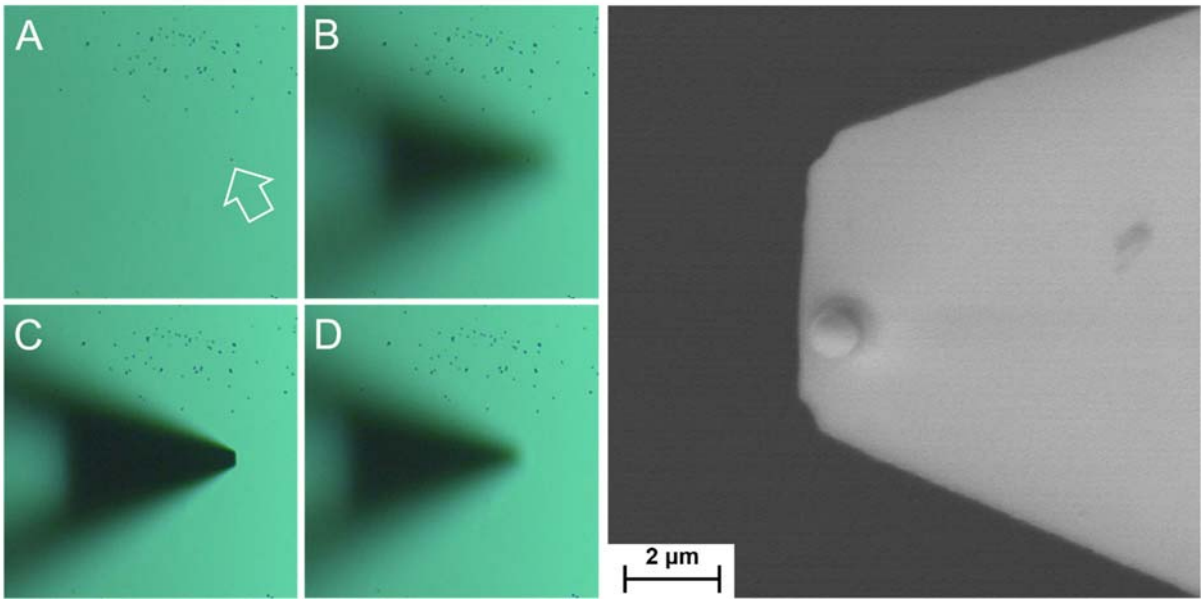


*Figure 95: Optical microscope images acquired during the gluing process (A-D). The white arrow indicates the isolated particle intended to be attached to the cantilever. Corresponding FE-SEM image of the glued and annealed cantilever featuring a single $TiO_2$ particle of ≈1.5 µm diameter (right).*

Finally, an isolated particle was identified and subsequently picked up by the wetted cantilever (Figure 94-D). Corresponding optical microscope images of the picking process are presented in Figure 95 A-D. Resulting colloidal probes were finally annealed at 100 °C for 2 h in order to fully cure the adhesive and subsequently characterized by means of FE-SEM imaging (Figure 95-right). In case the particle was found to be not situated at the very apex of the tip or in case of full wetting with resin the cantilever was not used for further experiments.

## 5.4. Results of colloidal probe studies

### 5.4.1. Influence of humidity on ultra-small $SiO_2$ // $SiO_2$ contacts

Initial experiments for the benchmarking of the new setup were performed using standard AFM probes with a sharp Si based tip versus a native $SiO_2$ terminated silicon wafer. During these experiments force distance curves were recorded at different relative humidity values. Corresponding results presented in Figure 96 indicate an increase of contact force upon the presence of water. However, it was found that the observed force exhibited a maximum at around 50% relative humidity followed by a strong decrease towards higher humidity values.

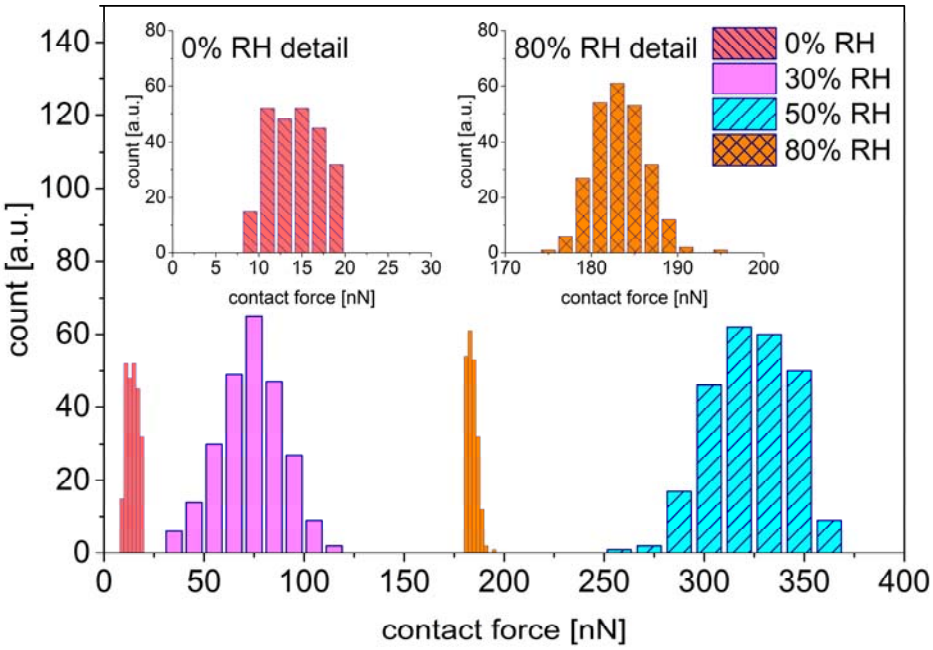


*Figure 96: Histogram of the observed contact force at different relative humidity levels.*

In addition, the distribution of the observed force values was much higher in the intermediate humidity regime than on both the dry and very humid end as evident from the corresponding boxplot in Figure 97.

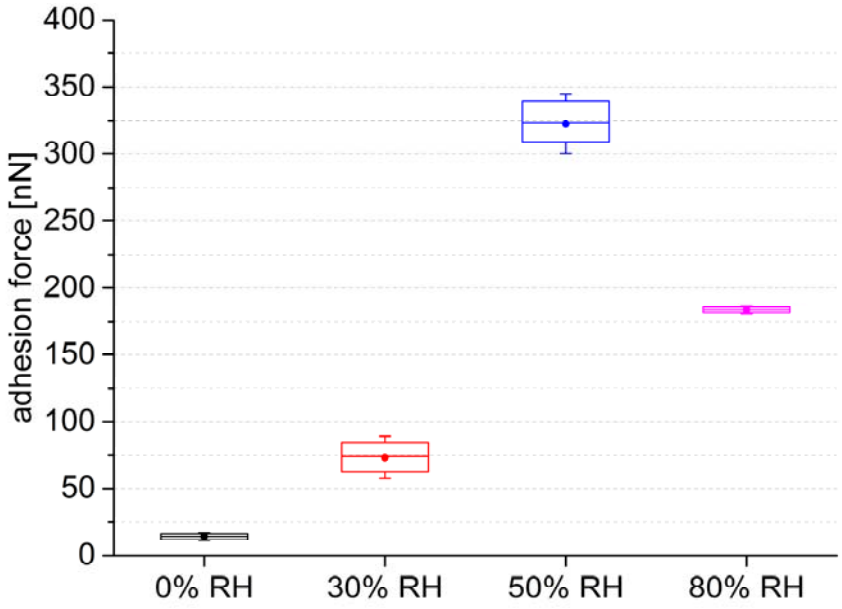


*Figure 97: Boxplot corresponding to the data presented in Figure 96.*

Observed behavior can be explained by the formation of a capillary bridge in the tip substrate contact zone effectively increasing the observed contact force due to the pressure difference within the water meniscus. As this process is highly dynamic in its nature, the distribution of the observed forces is much wider than at dry conditions. In addition, the length scale of the capillary radius at intermediate humidity is in the regime of the substrate roughness. Hence instead of one capillary, multiple smaller ones were formed at asperities on the substrate surface. As a result, the histogram corresponding to 50% RH featured a higher contact force compared to the histogram at 30% RH indicating contact events with a higher number of capillaries involved. Moreover, proposed argumentation also explains the decrease at high humidity values as under these conditions the size of the capillaries exceeds the length scale of the substrate roughness forming one large capillary instead of multiple smaller ones. As a result, the observed contact force decreased due to the much lower capillary pressure and the distribution of the observed forces narrowed due to the much more uniform contact events.

### 5.4.2. Influence of humidity to $SiO_2$ nanoparticle – micro-plateau contact

Investigations on the influence of relative humidity on the inter-particle contact force were performed by means of AFM based force distance spectroscopy. AFM tips used were prepared by the "grinding" method as described in section 5.3.1 facilitating force distance spectroscopy under defined geometry (Figure 89-left). Particle layers were prepared as described in section 3.2.1 using $SiO_2$ terminated wafers as substrates. Prior to the measurement, the system was purged with dry nitrogen for at least 2 hours. After dry conditions were established within the cell, an array of 16x16 force distance curves corresponding to a measured area of 2 µm x 2 µm was mapped. Subsequently, the relative humidity within the cell was varied. At each selected humidity 256 force distance curves were analyzed regarding the contact force and statistically evaluated as presented in Figure 98.

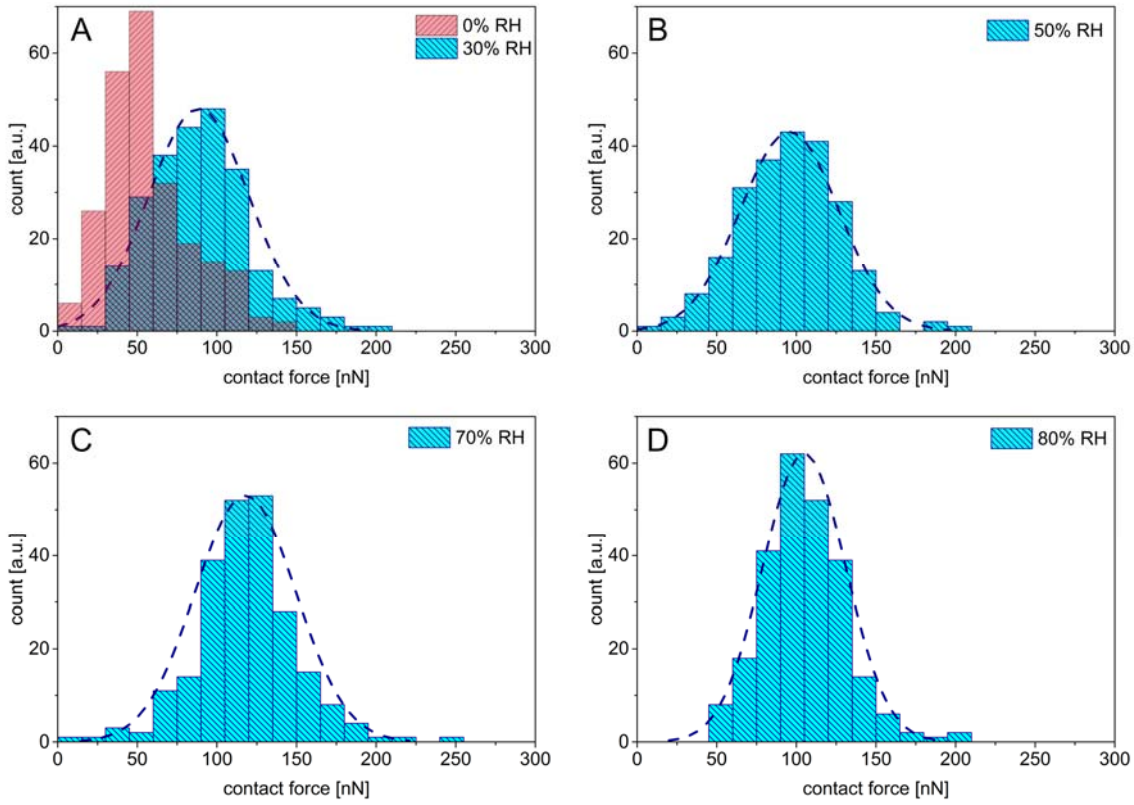


*Figure 98: Statistical evaluation of contact force measured at each given relative humidity (equilibration time: 30 minutes). Histograms plotted exhibit a shift of the mean contact force towards higher values upon the dosing of humidity as clearly visible in (A). Further variation of the water activity resulted in smaller changes of the mean contact forces with a maximum around 70% RH.*

It was found that the contact force observed immediately increased upon the presence of humidity in the surrounding atmosphere, comparable to the results presented in the previous section. However, in the regime between 30% and 70% RH only a much smaller additional increase of contact force was observed. This behavior is attributed to the initial change of interface chemistry due to the adsorption of water as well as the formation of capillaries in the contact zone. Once the free OH-groups were saturated with water molecules, additional humidity had only a minor impact on the overall contact force. In the experiment presented, a noticeable decrease of contact force around 80% RH has been observed.

Although measured forces are in good agreement with the corresponding values from the analytical solution as presented in Table 6, it has to be noted that the trend observed is quite opposite to the force evolution predicted by equation (2.27).

Table 6: Experimental and corresponding theoretically derived contact forces.

| RH | $F_{contact}$ experiment [nN] | $F_{contact}$ theory [nN] |
|---|---|---|
| 30% | 89 ±21 | 120 |
| 50% | 96 ±31 | 117 |
| 70% | 118 ±32 | 115 |
| 80% | 105 ±26 | 113 |

In order to emphasize this behavior, experimentally derived contact force values are presented in Figure 99 together with the corresponding theoretical values derived via equation (2.27).

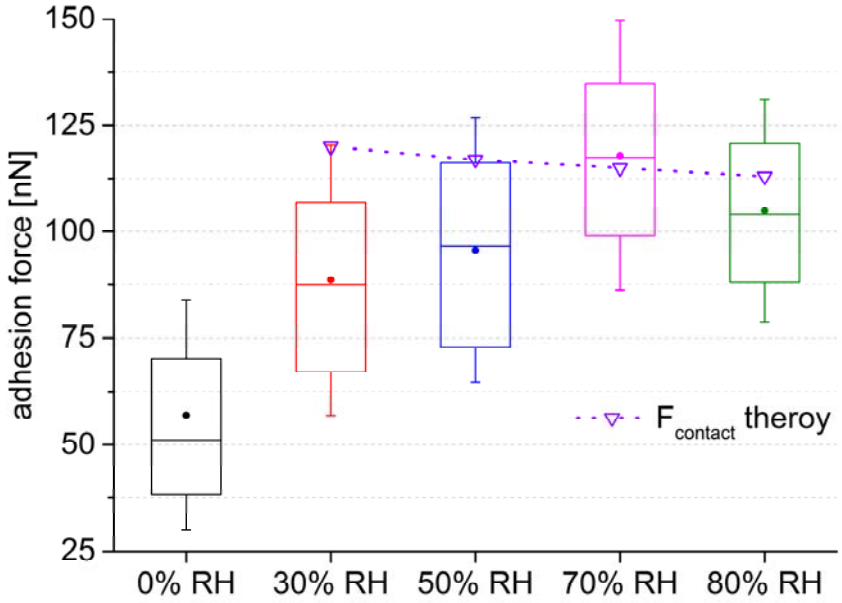


*Figure 99: Boxplot of the observed contact forces at different relative humidity values The violet triangles indicate the corresponding theoretical values based on equation* (2.27) for conditions where humidity was present in the system.

From Figure 99 it is evident that the analytical solution predicts a minor but steady decrease of the capillary force with increasing relative humidity. In contrast to that, the boxplot hints towards an increase up until a maximum is reached around 70% RH followed by a decrease towards even higher water activities. In this context is has to be noted that the standard deviation of the measured contact forces represented by the whiskers in Figure 99 is quite large in comparison to the total shift observed. However, presented results are in good agreement with multiple publications suggesting that this behavior can be attributed to the surface roughness [72,129-135]. Hence, it is assumed that although the particles as well as the grinded tip appeared to be smooth, they still featured a sub nm roughness below the detection limit which was in the same order of magnitude as the critical radius given by the Kelvin equation. Hence instead of one single capillary, multiple smaller capillaries were formed at asperities on the objects in contact. In the case of an increase in humidity, the number of smaller capillaries formed was increased resulting in a higher macroscopically observed contact force. However, mentioned process is limited by a certain threshold value for the humidity which is reached once the critical radius as given by the Kelvin equation surpasses the length scale of the roughness. In this case the smaller capillary start to merge forming one larger capillary. As a result, the analytical solution and its prediction of a decreasing force with increasing humidity begin to hold true once this threshold value is being surpassed. Based on this, it can be concluded that this threshold value was exceeded between 70% and 80% RH which justifies the measured values as well as the trend observed, despite contradicting the theoretical calculations. In addition, it has to be noted that during the evaluation of presented experiments some of the force distance curves had to be omitted as outliers, most probably stemming from contact events where the micro plateau did not hit a single particle or induced a rolling motion. In order to overcome this, further studies were conducted with model contacts using colloidal probes prepared either by gluing or annealing as presented in the preceding sections.

### 5.4.3. Influence of humidity and UV-light on $TiO_2$ micro and nano-contacts

Sample preparation for this study was made by means of ALD deposition of a 30 nm thick $TiO_2$ layer on a UV-light transparent fused silica slide facilitating the investigation of the influence of UV-light on the contact force between anatase surfaces. In addition to the coated substrate, an annealed AFM tip featuring a radius of curvature of ≈150 nm was coated by the same process effectively resembling a single $TiO_2$ nanoparticle. Both the plane and the cantilever were annealed at 500 °C for 5 h in order to trigger the crystallization process from the as received amorphous phase to an anatase crystal phase. The experiment consisted of force distance spectroscopy without as well as with UV-light exposure, each at various relative humidity values. Corresponding results are presented in Figure 100 and Figure 101.

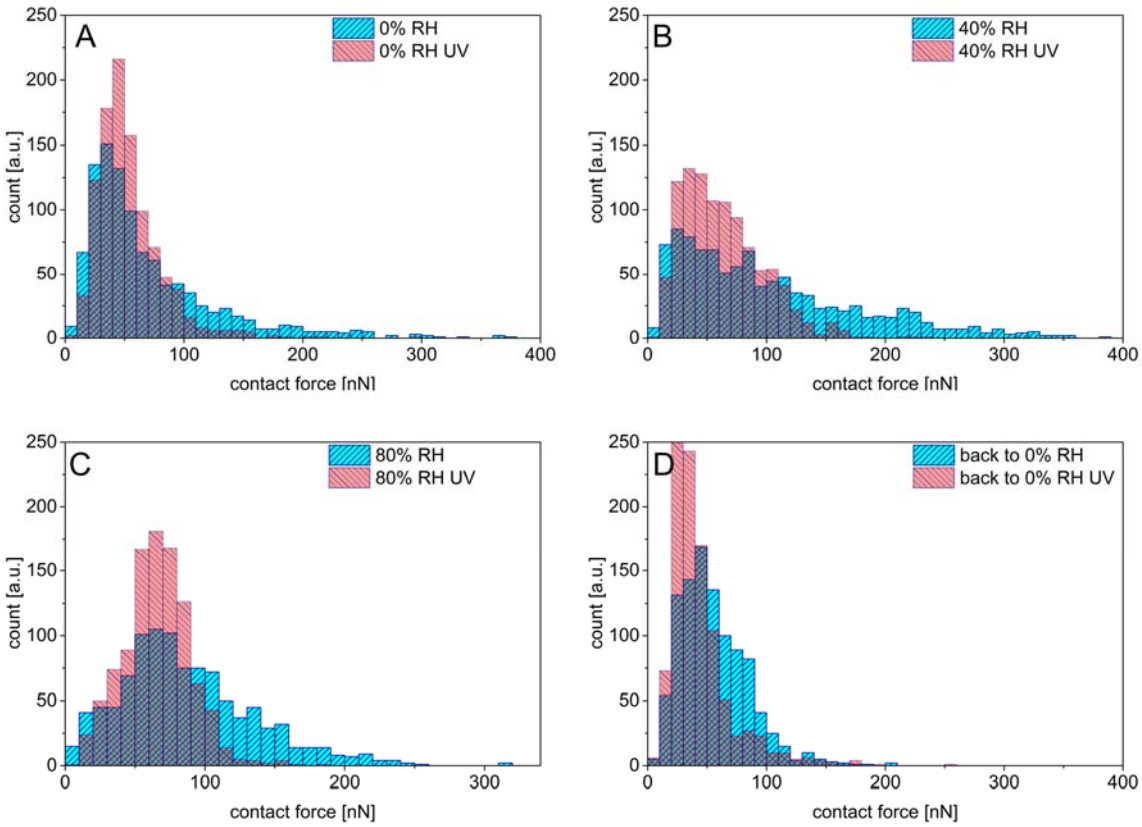


*Figure 100: Force histograms of the experiments performed on an anatase sphere wall contact at different relative humidity values both with (violet) and without (blue) UV-light exposure.*

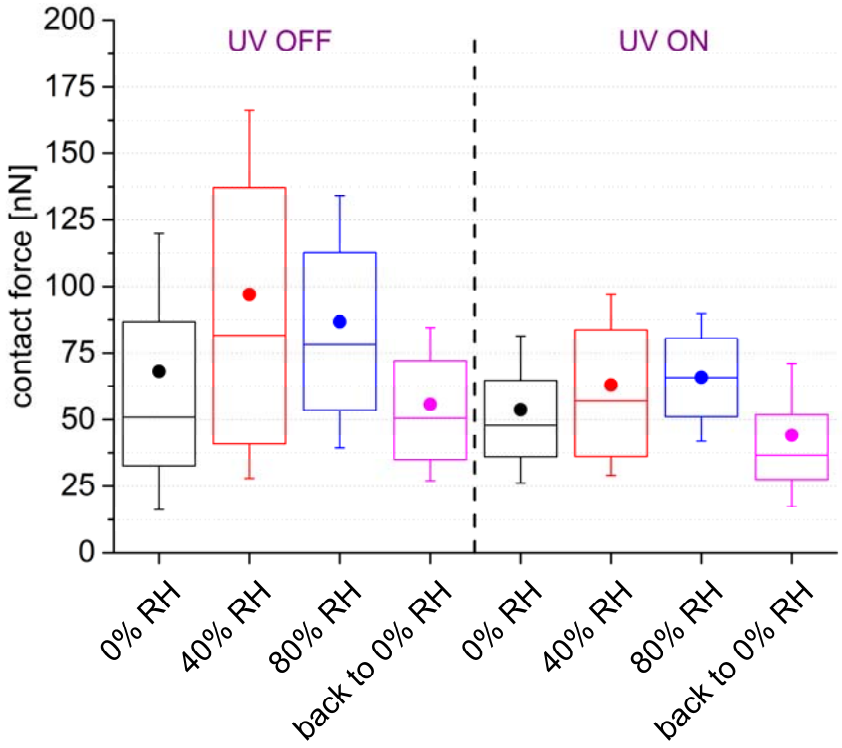


*Figure 101: Boxplot of the histograms presented in Figure 100. Datasets acquired without the influence of UV-light (left) and during ongoing UV-light irradiation (right).*

Following section will focus on the results in the absence of UV-light. It was found that the contact force increased immediately in the presence of humidity in the system (Figure 101-left, red box). This finding is in good agreement with the experimental data discussed in the preceding sections. In addition, a dramatic broadening of the histogram was noticed at 40% RH indicating many different contact events. As the substrate surface was much rougher compared to previous experiments, this behavior can again be attributed to the formation of capillary bridges with a broader size distribution. This is further supported by the fact that the distribution narrowed considerably at higher relative humidity values (Figure 101-left, blue box) due to the fact that the critical radius predicted by the Kelvin equation again surpassed the length scale of the surface roughness. As a result, instead of multiple smaller capillaries, one single, much larger capillary with more uniform properties was being formed. Moreover, the studied contacts also exhibited the characteristic decrease of the contact force at high water activities as predicted by the analytical solution. Presented results are further supported by the fact that the experimentally derived values of the contact force are found to feature the same order of magnitude as the theoretical values as predicted by the analytical solution. However, the experimental values are generally slightly lower than expected which again is attributed to the roughness effectively reducing the overall force due to the lower effective contact area.

Force histograms acquired in presence of UV-light were found to exhibit a narrower distribution, as can be seen on Figure 101-right. This can be explained with the assumption that surface contaminations were oxidized and desorbed upon UV-light exposure, leading to a more uniform surface chemistry. Consequently, the contact events tended to be much more similar resulting in a significantly narrower force distribution. In addition, the histograms mean value was slightly shifted toward higher values in the case of dry and very humid (80% RH) conditions. The histogram at 40% lacked the many multi capillary events present in the dataset without UV-light exposure. In context of the UV-light dependent QCM experiments presented in section 4.5.2.2 where it was found that the ongoing irradiation actually lowered the water uptake due to the energy dissipation, it can be concluded that a similar process occurred during this experiment. On the one hand, the UV-light irradiation induced the photo-oxidation of adsorbate species effectively increasing the surface polarity leading to higher capillary forces. On the other hand, the dissipated energy promoted the thermally initiated desorption of adsorbate water despite the increased polarity of the surfaces. Hence, the formation of contact events consisting of multiple smaller capillaries as found at intermediate humidity levels became less favorable resulting in smaller number of high contact force events. A similar, but much less pronounced trend was also observed in the high humidity region. However, as the capillaries at this conditions are generally much larger, the dissipated heat induced a much smaller effect.

### 5.4.4. Influence of UV-light on the contact force of chemically modified surfaces.

The set of experiments presented in this chapter consisted of two steps: initially the evolution of the contact force as a function of UV-light irradiation was studied similar to the results presented in the preceding section. Subsequently the probe as well as the substrate were chemically modified with a hydrophobic SAM in order to study the effect of UV-light towards the contact force affected by a model contamination. However, in order to mitigate the influence of roughness on the observed forces, a custom prepared colloidal probe was used (section 5.3.3). Hence, by scaling the contact from few hundred nm (annealed tip) to ≈1.5 µm (particle diameter) the effective contact area was increased considerably. Initial experiments presented in Figure 102 featured a much higher contact force compared to the previous results which is in good agreement with the values predicted by the analytical solution for given geometry.

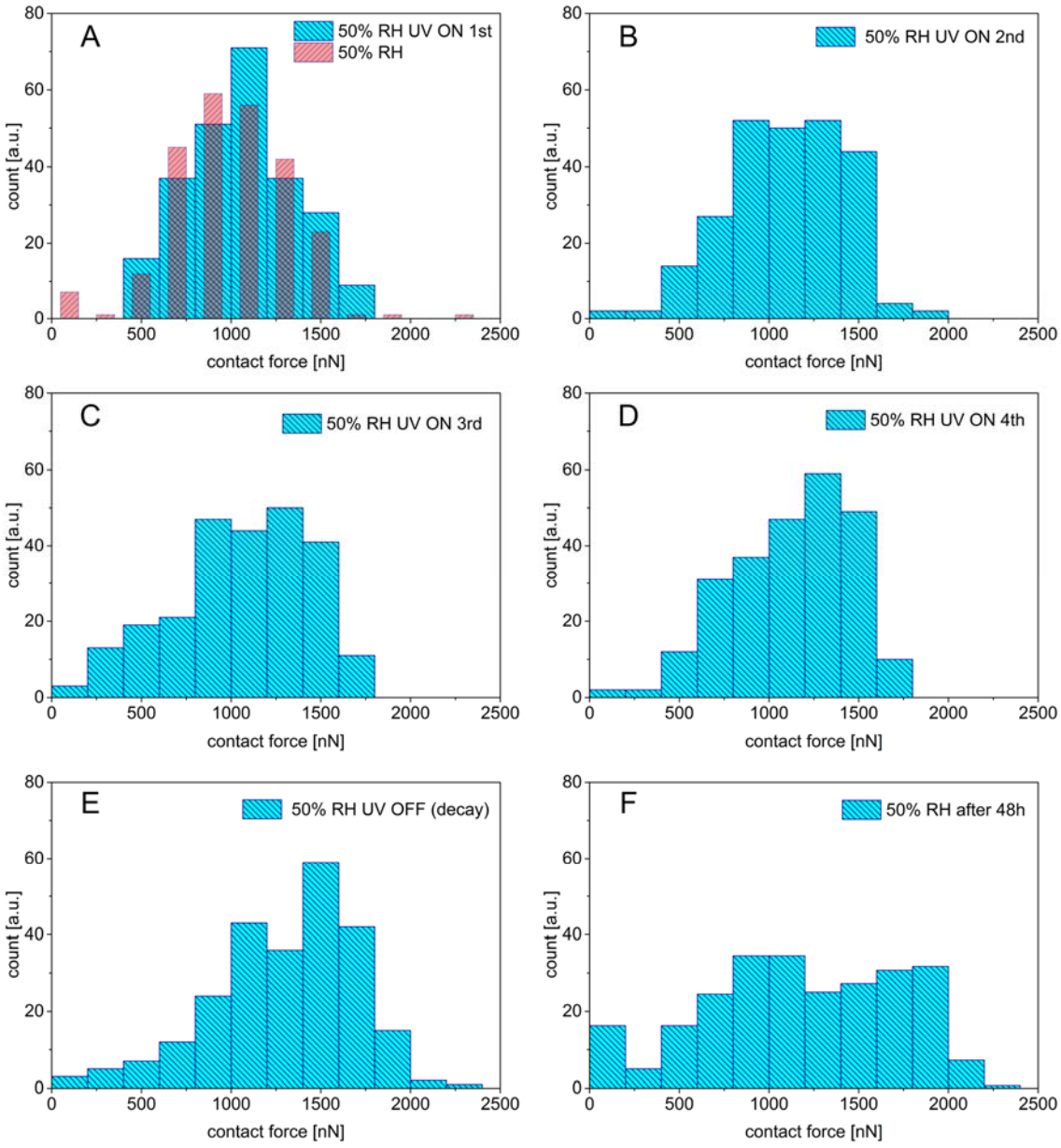


*Figure 102: Evolution of the contact force as a function of exposure towards UV-light (A →D) and corresponding relaxation (E,F). Acquisition time of each histogram was ≈25 min.*

Presented histograms indicate a gradual shift of contact force towards higher values during ongoing irradiation. As the data acquisition was rather slow (≈25 minutes per histogram) with respect to the surface activation, intermediate datasets featured a considerable broadening. This stems from the fact that the contact force was undergoing changes on a timescale comparable to that of the experiment itself.

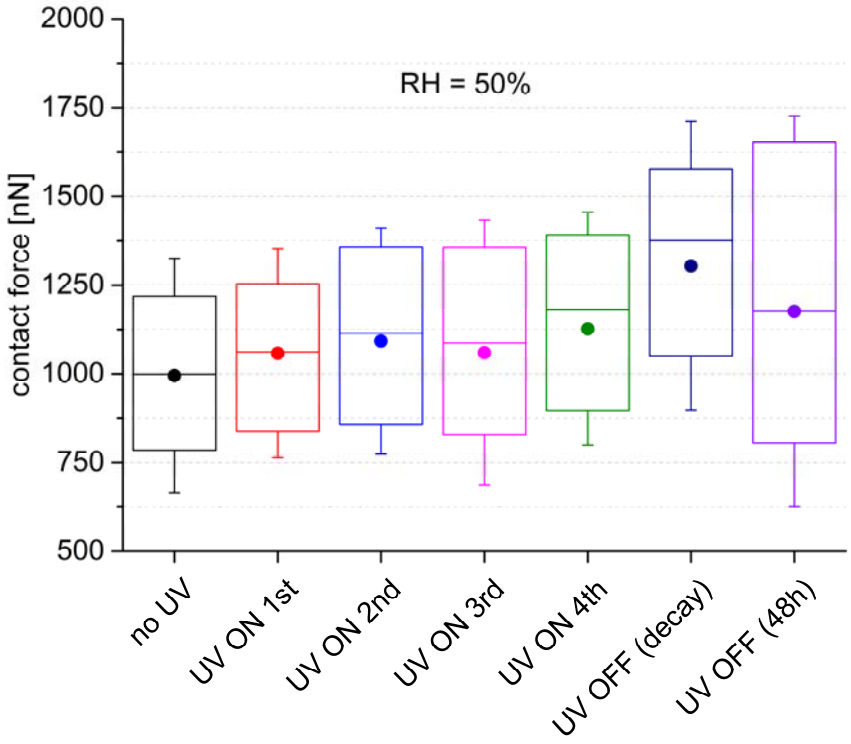


*Figure 103: Boxplot of the histograms presented in Figure 102.*

The increase of the average contact force during UV-light irradiation as indicated by the boxplot in Figure 103, can be attributed to the increase in surface polarity reducing the contact angle which in turn increases the capillary pressure. Interestingly, a UV-light induced narrowing due to the loss of multi-capillary contact events featuring very small capillaries was not observed. Hence it can be assumed that this system seems to be less dominated by roughness, as the capillary volume is much larger, resulting in dissipated heat playing a less important role when compared to previous experiments. After a stable condition was established (Figure 102-D), the UV-light irradiation was stopped and surfaces were allowed to relax for 30 minutes before a new dataset was acquired. Corresponding histogram (Figure 102-E) indicates a noticeable broadening compared to the last excited state (Figure 102-D) towards the higher contact force as well as to the lower contact force region. The latter can be explained by the slow relaxation reducing the number of surface OH-groups and effectively decreasing the surface polarity. In contrast to that, the broadening

towards the higher contact force branch is attributed to the lack of thermal energy input. As a result, smaller capillaries could form again facilitating the observation of contact events with a higher number of participating capillaries inducing contact events featuring a much greater observed force. Interestingly, the contribution of higher contact force events seems to dominate as both the mean and median contact force values are much higher when comparing the blue (UV-light off) and green (UV-light on) box in Figure 103.

Finally, the sample was allowed to relax for 48 h before the measurement was repeated. As indicated by the corresponding histogram (Figure 102-F) a very broad distribution with no clear maximum was found. Interestingly, both larger and smaller forces were observable when compared to the initial dataset (Figure 102-A green histogram). The fact that the samples contact force properties did not fully restore to the values initially found even after 48 h makes it unlikely that this can be attributed to a partially relaxation. Instead it is much more likely that the sample did not fully re-contaminate due to the very clean conditions within the AFM. Hence, in order to shed some more light on the effect of UV-light induced photo-oxidation of adsorbate species on $TiO_2$, the sample as well as the colloid were modified by means of solution self-assembly of ODPA serving a model adsorbate. Although phosphonic acids do not resemble a typical atmospheric contaminant, this approach was chosen as they feature outstanding binding properties on $TiO_2$. Preparation was performed as discussed in section 3.3.2 followed by subsequent AFM based force distance spectroscopy. Corresponding histograms are presented in Figure 104.

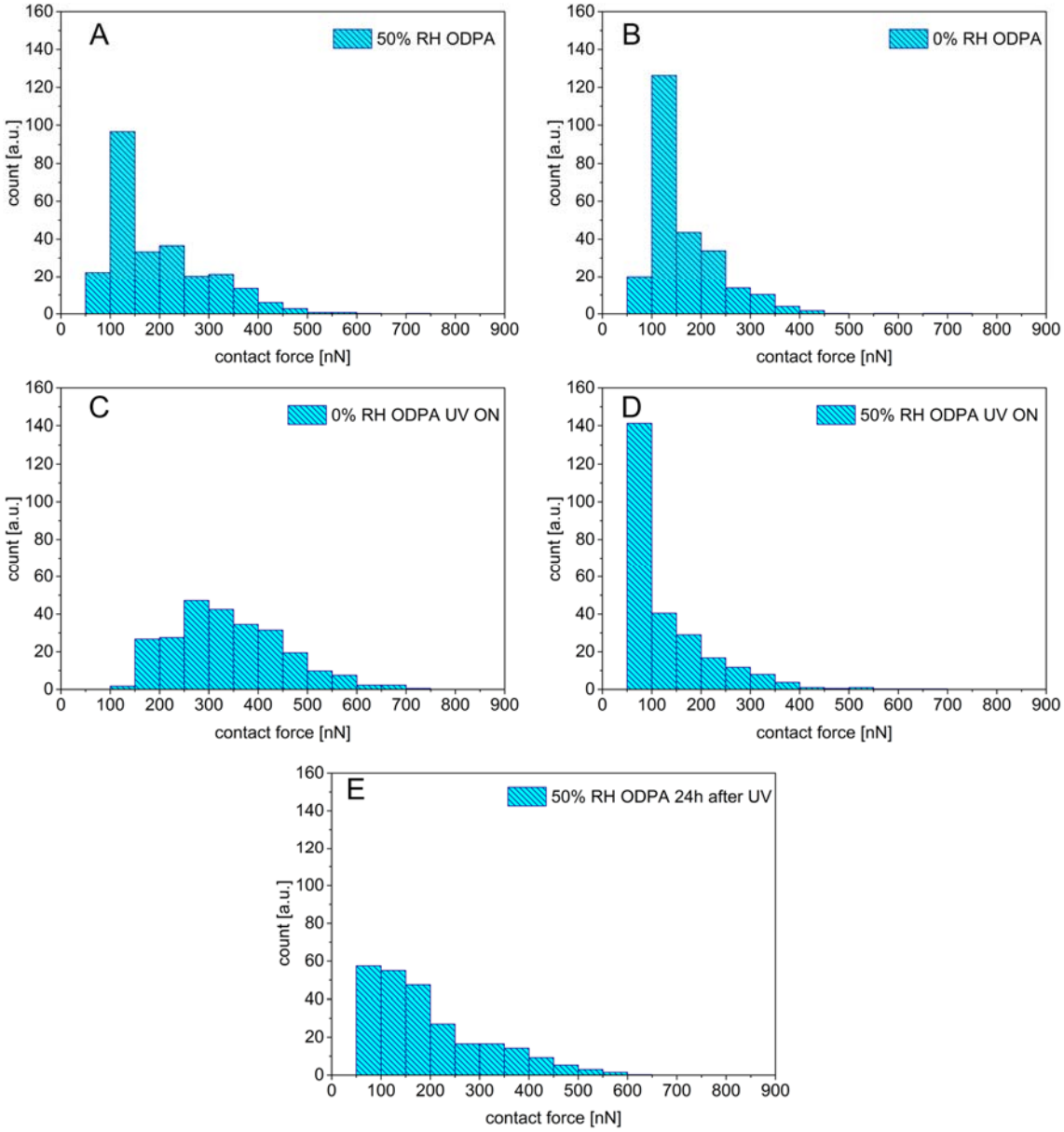


*Figure 104: Force distance evaluation of experiments performed on an ODPA modified $TiO_2$ surface using an ODPA modified $TiO_2$ colloid.*

Initial measurements on chemically modified surfaces at 50% relative humidity indicated a much lower contact force which is in good agreement with the very hydrophobic surface preventing the formation of capillaries in the contact zone (Figure 104-A). This assumption is further supported by the fact that upon drying, observed histogram exhibited only minor changes (Figure 104-B).

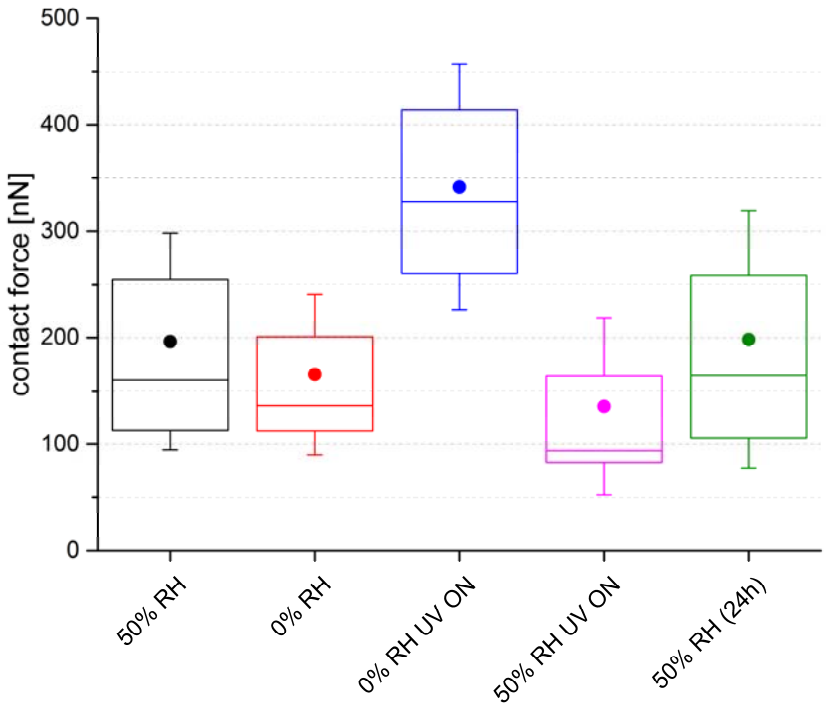


*Figure 105: Boxplot of the histograms presented in Figure 104.*

In order to study the influence of photo-oxidation on the contact force, the sample was subsequently illuminated with UV-light similar to previous experiments. In order to reach quasi stable conditions, the sample was irradiated for 1.5 h at dry conditions before measurement. It was found that the mean contact force shifted towards higher values despite the absence of water (Figure 105 blue box). However, measured forces were still much lower than those observed on the untreated surface indicating a partial restoration of the polar surface (Figure 103). Most interestingly, contact force decreased immediately upon the dosing of humidity to the system (Figure 105 magenta box). Moreover, only minor further changes to the histogram were found after leaving the sample for relaxation at 50% relative humidity for 24 h (Figure 105 green box). This behavior could be explained by means of a partial delamination of the ODPA molecules. Previous studies by Thissen et al. [136] indicated that ODPA was not stable towards water on alumina surfaces. A similar process is assumed to happen in this case. During initial conditions the SAM was dense and therefore hydrophobic enough to fully prevent the formation of capillaries effectively preventing the destabilization of the ODPA layer. Furthermore, this finding is in agreement with previous results reported by Maxisch et al. which found that water molecules, despite being able to easily penetrate an ODPA layer on alumina, did not degrade the SAMs when exposed to high water activities in the gas phase [127]. However, photo-oxidation induced defects facilitated the initial formation

of small capillaries in the contact zone which consequently started to destabilize the ODPA layer. In contrast however to the study of Thissen et al. where a sample immersed in an electrolyte was studied [136], desorbed ODPA species were confined within the capillary and could therefore not dissipate from the system. Upon retraction of the colloid, the water previously situated in the capillary spread on both surfaces and evaporated leaving the ODPA molecules on the surface which in turn were forced to re-adsorb. As a result, the ODPA molecules gained a certain degree of mobility due to multiple water induced de- and re-adsorption events effectively partially mitigating the UV-light induced defect formation and restoring a hydrophobic surface as indicated by the low specific contact force derived from histogram D in Figure 104. However, further experiments like a study related to the stability of ODPA on $TiO_2$ surfaces should be performed in order to confirm the presented explanation.

## 5.5. Conclusions

Experiments presented in this chapter focused on the investigation of the interplay between humidity and surface chemistry towards the inter-particle contact force. Therefore, a new in-situ AFM based experimental setup was established facilitating investigations on the UV-light and humidity dependent contact force properties of nano- and micro-particle layers. In addition, highly defined AFM tips featuring geometries necessary to resemble individual particle wall contacts have been prepared using custom designed materials.

It was shown that the addition of humidity led to an initial increase of contact force followed by a consecutive decrease at higher water activities. This behavior was successfully observed in three different contact geometries (tip-wall, nanoparticle-wall, colloid-wall) as well as two relevant materials ($SiO_2$ and $TiO_2$) and is generally attributed to the surface morphology (roughness).

In addition, the influence of UV-light induced hydrophilization of $TiO_2$ surfaces on the contact force was probed and a small shift towards higher forces accompanied by a strong decrease of the measured forces distribution was observed. This finding is explained by means of two competitive processes:

1. The UV-light induced hydrophilization leads to an increase of capillary pressure (increased contact force).
2. The thermal desorption of water due to the dissipation of heat stemming from the ongoing irradiation leads to an overall lower number of capillaries in the contact zone.

Apparently, the latter effect was mostly dominating in the systems presented in this chapter. These results directly support the QCM investigation on the UV-light activation of titanium oxide particles presented in section 4.5.2.1 which indicated a similar behavior.

The presented results illustrate that the AFM based analysis of nanoparticle contacts facilitates a very detailed characterization of the particle contact forces as a function of various environmental parameters like water activity and UV-light exposure. In addition, the accessibility of quantitative contact force data renders this approach a unique and a very valuable source for parameters necessary for the simulation of these nanoscale contacts.

# 6. Overall Conclusions

The focus of this thesis was to elucidate two main questions in focus:

1. What is the role of water adsorbate layers in nanoparticle ensembles and how does the complex water structure impact the inter-particle forces as a function of humidity?

2. What influence does the surface chemistry of nanoparticles have on the inter-particle forces and can these interactions be altered via chemical modification?

In order to conduct a fundamental study towards answering these questions, two well-defined model particle systems ($SiO_2$ and $TiO_2$) were used. From an experimental perspective, two new setups played a key role within the scope of this thesis:

1. A novel combined in-situ QCM-D / FT-IR experiment allowed for a very detailed simultaneous study of the water structure (monitored by means of FT-IR), the water uptake by means of mass change (QCM, frequency shift) as well as the investigation of changes of mechanical properties of the particle layer (QCM, dissipation).

2. AFM based force spectroscopy in combination with a new cell which allowed for experiments as a function of humidity as well as UV-light irradiation. This novel setup enabled investigations of the interplay between surface chemistry and humidity towards inter-particle contact force in a quantitative manner.

Combining the results of these two complex methodologies on mentioned highly defined model particle system, it was possible to get an insight on various nanoscale processes under environmental conditions at a fundamental level.

AFM force spectroscopy measurements (chapter 5.4.1 and 5.4.2) with single particle contact geometries indicated a gradual increase of contact force until a maximum was reached around 60% to 80% relative humidity. For higher humidity values the contact force started to decrease again. This effect is commonly attributed to the surface roughness. Briefly, at lower humidity values only few capillaries form at asperities on the surface. Upon the increase of water activity, the number of small capillaries grows resulting in a higher contact force. Once the capillary radius given by Kelvins equation surpasses the length scale of the surface roughness all smaller capillaries coalescence into one large meniscus which the obeys the analytical solution predicting a decrease of contact force for higher relative humidity values. However, this rather simple approach neglects the significant structural changes of the water layers that were identified in the presented study. FT-IR data measured during combined QCM-D / FT-IR experiments (chapter 4.4) revealed substantial changes of the water structure as a function of relative humidity in the particle systems under investigation. It was found that the adsorbate water species exhibited a dominant "ice" like structure between the low and intermediate relative humidity regime (0% to 40% RH) These results could be correlated with dissipation data from the QCM which indicated a change of contact stiffness between the particle and the underlying substrate upon the transition from predominant "ice" like to "liquid" like species at higher relative humidity values (60% RH to 95% RH). Consequently, a slightly altered model is proposed (Figure 106) for the water adsorption and capillary bridge formation taking the structural changes of the water molecules into account. In essence, during a gradual increase of relative humidity two processes occur:

1. Increase of number of small capillaries until they coalescence into one large meniscus.
2. Transition of water structure from "ice" like to "liquid" like structure.

As a result, the increase of contact force during the transition from the low to the intermediate relative humidity regime should not only be attributed to the increasing number of smaller capillaries but also to the dominant "ice" like structure of the water molecules as depicted in Figure 106-left and center. Although the "liquid" like species begins to play a major role in the intermediate state, corresponding FT-IR data still suggests a major role of the "ice" like component.

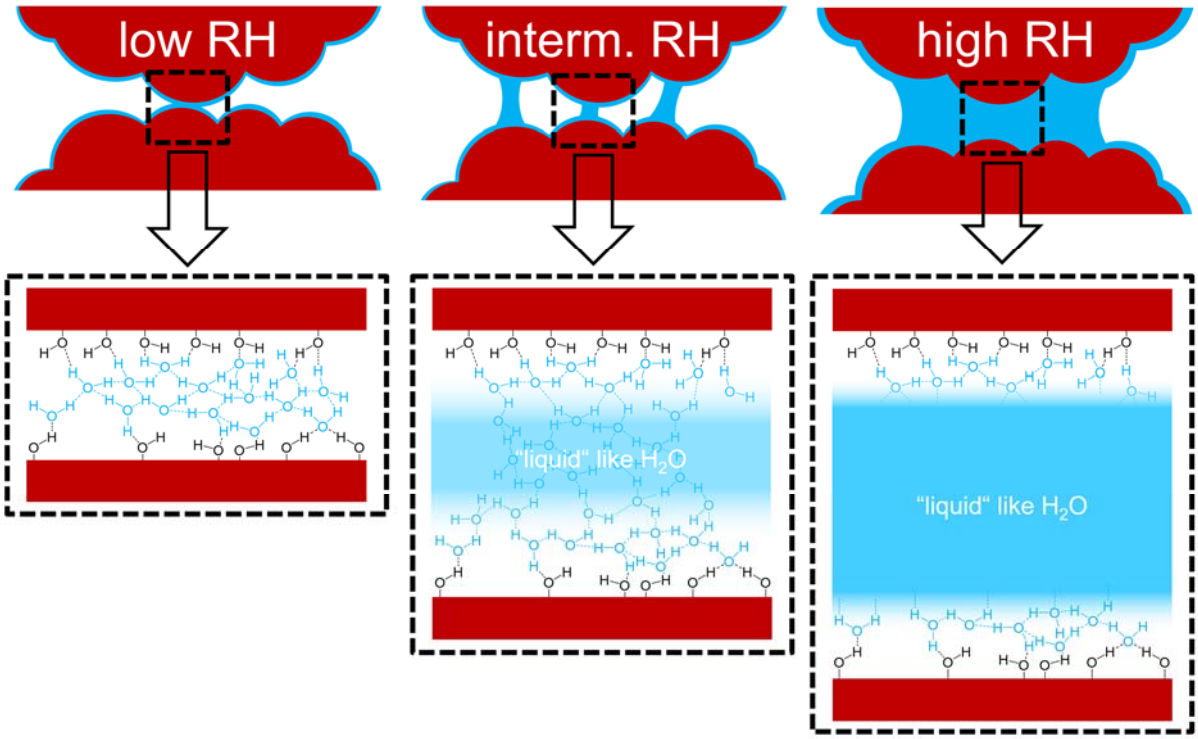


*Figure 106: Schematic of the water structure in the contact zone at low(left) and high(right) relative humidity.*

Furthermore, proposed model also explains the decrease of contact force at high relative humidity (Figure 106-right) based on the structural changes of the water molecules. Since the dominant "liquid" like water molecules are much more dynamic the resulting network exerts a much lower force between the two particles in contact. In consequence the overall attracting force decreases when compared to the contact force at intermediate relative humidity. These results are further supported by the quantitative analysis of the QCM data which indicated a faster growth rate of the capillary volume at the identical humidity levels where the transition of water structure was observed. Hence this finding is in good agreement with the proposed merging of the smaller capillaries forming one large capillary instead.

Additional AFM and QCM based in-situ experiments performed on $TiO_2$ particles modified by UV-light irradiation (chapter 4.5.2) indicated a noticeable change in water uptake. These results were attributed to the change of surface chemistry induced by the irradiation with UV-light. Corresponding in-situ QCM experiments revealed a much higher water uptake after UV-light treatment. In the context of the proposed model presented in Figure 106, the UV-light promoted photo-oxidation resulted in the formation of new surface bound OH-groups severing as additional adsorption sites for water molecules. Further AFM based experiments (chapter 5.4.3 and 5.4.4) indicating the favorable formation of larger capillaries which is in good agreement with the previous results. Moreover, both complementary

methods indicated the presence of two competing processes: On the one hand, the hydrophilization due to the formation of additional surface bound OH-groups led to an increase of water uptake. On the other hand, the continuous dissipation of heat resulted in a thermally induced desorption of water which was often found to dominate the system.

In addition to the experiments on particle surfaces modified by means of UV-light irradiation, classical chemical modification by means of chemical vapor deposition as well as solution self-assembly had been employed. Results presented in chapter 4.5.1 indicated that as opposed to the observed drastic water contact angle difference, changes on the nanoscopic scale were found to be almost negligible. In particular, the combined QCM-D / FT-IR experiments revealed that the water adsorption properties of hydrophobic organosilane modified $SiO_2$ particles were largely unaltered. Further investigations on appropriate model system revealed that his effect stemmed from the special structure of these molecular layers. In contrast to that, the AFM results on an ODPA modified sphere wall contact (chapter 5.4.4) indicated a strong decrease of contact force.

On first thought these two results stand in contradiction to the each other. However, it has to be noted that as by design, the two experiments probe different areas of the nanoparticle contacts. In the case of the QCM-D experiments the particles had been modified after deposition via chemical vapor deposition. Hence, as discussed in the corresponding section 4.6, the actual contact zone was mostly uncoated. Moreover, the arc-like structure of the organosilane films allowed for the penetration and accumulation of water on the particle surfaces despite the macroscopically observed high water contact angle. In the case of the AFM based approach, the actual probed surface was smooth and the surfactant molecules much smaller compared to the organosilane oligomers. Consequently, steric hindrance based effects were diminished during the modification phase. Moreover, the single particle located on the cantilever was fully exposed to the solution carrying the surfactant species. As a result, both surfaces were fully covered with a dense ODPA monolayer leading to significant decrease of contact force due to the inhibition of capillary formation.

In essence, the drastically different results emphasize that the interplay between contact forces and adsorbate species is very complex. Besides the chemical nature of adsorbates (functional groups, length, polarity), the actual structure of the films was found to play a key role towards changes in particle behavior on a macroscopic scale.

# 7. Outlook

Methods and results presented in this study represent a foundation for further experiments to achieve a fundamental understanding of the processes involving chemically altered nanoparticle ensembles at environmental conditions. Although atmospheric water undoubtedly plays the most important role when it comes to small ambient molecules, other molecules might feature interesting properties too. Small organic molecules like ethanol, for instance, are also quite common but feature entirely different chemical and physical properties. Without a doubt, repetition of certain key experiments using different solvent systems would give valuable information with regard to adsorption and contact force behavior. Moreover, as discussed in the conclusions section of chapter 5, the UV-light based experiments on ODPA modified particle systems need more complementary measurements in order to fully explain the effects found. In this context, a study of the stability of ODPA on $TiO_2$ surfaces during exposure to water on appropriate model substrates should be performed.

Aside of other experimental approaches, development of a theoretical model for the evaluation of the AFM as well as the highly complex QCM results would provide a better understanding of the experimental findings. Particularly, the latter appears to be very promising as the QCM by nature would probe millions of contacts at once resulting in highly reliable values for contact stiffness. Hence, these results could be used for the experimental validation of the numerous simulations published by other groups. Efforts towards the development of such a model will be in focus of future work.

In addition to the planned work towards the development of model based method for the quantitative evaluation of the contact stiffness based on the QCM results, further simulation of the water structure at the $TiO_2$ interface would be of great help as the evaluation of the “ice”

like and “water” like species has still room for improvement. In this context, a more fundamental approach on a much more defined surface such as a single crystal could be employed to perform complimentary investigations.

To conclude, presented thesis gave a brief glimpse on some of the effects stemming from the very complex interplay of humidity and surface chemistry between nanoparticles in contact. However, as these systems do not solely depend on these two parameters, a comprehensive understanding of all effects and processes involved is far beyond the scope of this thesis alone leaving much space for further interesting studies.

# 8. Appendix

## 8.1. List of abbreviations

| | |
|---|---|
| AES | auger-electron spectroscopy |
| AFM | atomic force microscope |
| at% | atomic concentration |
| ATR | attenuated total reflectance-FT-IR |
| BET | Stephen Brunauer, Paul Hugh Emmett, Edward Teller (method) |
| BG | bandgap |
| CB | conductance band |
| cn | coordination number |
| CVD | chemical vapor deposition |
| DDA | dodecyl-amine |
| DLVO-theory | Derjaguin, Landau, Verwey, Overbeek theory |
| DPM-IRRAS | discrete polarization modulated-(IRRAS) |
| DRIFT | diffuse reflectance infrared Fourier transform (spectroscopy) |
| EDX | energy dispersive X-ray (spectroscopy) |
| FE-SEM | field emitter scanning electron microscope |
| FIB | focused ion beam |
| FT-IR | Fourier transform infrared (spectroscopy) |
| hcp | hexagonal closest packing |
| HMDSO | hexmethylene-disiloxan |
| IRRAS | infrared reflection absorption spectroscopy |
| MFC | mass flow controller |
| NP | nanoparticle |
| ODPA | octadecane-phosphonic acid |
| ODT | octadecane-thiol |
| PE-CVD | plasma enhanced chemical vapor deposition |
| PID | proportional–integral–derivative controller |
| PM-IRRAS | polarization modulated IRRAS |
| PTFE | poly-tetra-fluor-ethylene |
| QCM | quartz crystal microbalance |
| RH | relative humidity |
| SD | standard deviation |
| STM | scanning tunneling microscope |
| TTIP | titanium (IV) isopropoxide |
| UV-light | ultraviolet light |
| VB | valence band |
| vdW | van der Waals (force) |
| WCA | (static) water contact angle |
| XPS | X-ray photoelectron spectroscopy |

## 8.2. List of symbols

A area
$A_H$ Hamaker constant
D distance
E energy
F force
$f_0$ base frequency
h Planck's constant $6.63 \cdot 10^{-34}$ J·s
$k_B$ Boltzmann constant $1.38 \cdot 10^{-23}$ $J \cdot K^{-1}$
n quantum number
p (partial) pressure
$p_0$ saturating pressure
Q charge
r radius
R gas constant $8.31 \cdot J \cdot K^{-1} \cdot mol^{-1}$
T temperature
U electrical potential
V volume
W work
α polarizability
γ surface tension
Γ bandwidth
Δf frequency shift
ε dielectric permittivity
$\varepsilon_0$ vacuum permittivity $8.85 \cdot 10^{-12}$ $A \cdot s \cdot V^{-1} \cdot m^{-1}$
θ contact angle
λ surface increase factor
μ dipole moment
ν frequency
ρ density
Φ work function

## 8.3. Supervised student papers

Some of the results presented within this thesis were acquired within the scope of the supervision of the following student papers:

1. Dennis Meinderink:
   Combined in-situ QCM-D / FT-IR studies of the water adsorption on $SiO_2$ nanoparticles modified via CVD route.

2. Yan Han:
   In-situ PM-IRRAS studies of the water adsorption on CVD modified $SiO_x$ layers.

## 8.4. Declaration of originality

I hereby declare that this thesis represents my original work and that I have used no other sources except as noted by citations. All data, tables, figures and text citations which have been reproduced from any other source have been explicitly acknowledged as such.

Paderborn, April 18, 2016

Boray Torun

## 8.5. List of figures

## 8.6. List of tables

## 8.7. References

[1] Feynman R. P., Leighton R. B., Sands M. L. *The Feynman lectures on physics*; Basic Books, a member of the Perseus Books Group: New York, 1963.

[2] Sattler K. D. *Handbook of Nanophysics: Nanoparticles and Quantum Dots*; CRC Press: Hoboken, 2010.

[3] Zeng, S., Yu, X., Law, W.-C., Zhang, Y., Hu, R., Dinh, X.-Q., Ho, H.-P., Yong, K.-T. Size dependence of Au NP-enhanced surface plasmon resonance based on differential phase measurement. *Sensors and Actuators B: Chemical* **2013**, *176*, 1128–1133.

[4] Dreaden, E. C., Alkilany, A. M., Huang, X., Murphy, C. J., El-Sayed, M. A. The golden age: gold nanoparticles for biomedicine. *Chemical Society reviews* **2012**, *41*, 2740–2779.

[5] Huang, X., Jain, P. K., El-Sayed, I. H., El-Sayed, M. A. Gold nanoparticles: interesting optical properties and recent applications in cancer diagnostics and therapy **2007**.

[6] Huang, X., El-Sayed, M. A. Gold nanoparticles: Optical properties and implementations in cancer diagnosis and photothermal therapy. *Journal of Advanced Research* **2010**, *1*, 13–28.

[7] West, J. L., Halas, N. J. Engineered nanomaterials for biophotonics applications: improving sensing, imaging, and therapeutics. *Annual Review of Biomedical Engineering* **2003**, *5*, 285–292.

[8] Skrabalak, S. E., Au, L., Li, X., Xia, Y. Facile synthesis of Ag nanocubes and Au nanocages. *Nature protocols* **2007**, *2*, 2182–2190.

[9] Provenzale, J. M., Silva, G. A. Uses of nanoparticles for central nervous system imaging and therapy. *AJNR. American journal of neuroradiology* **2009**, *30*, 1293–1301.

[10] Kim, J. S., Kuk, E., Yu, K. N., Kim, J.-H., Park, S. J., Lee, H. J., Kim, S. H., Park, Y. K., Park, Y. H., Hwang, C.-Y., Kim, Y.-K., Lee, Y.-S., Jeong, D. H., Cho, M.-H. Antimicrobial effects of silver nanoparticles. *Nanomedicine nanotechnology, biology, and medicine* **2007**, *3*, 95–101.

[11] Kong, H., Jang, J. Antibacterial properties of novel poly (methyl methacrylate) nanofiber containing silver nanoparticles. *Langmuir* **2008**, *24*, 2051–2056.

[12] Sondi, I., Salopek-Sondi, B. Silver nanoparticles as antimicrobial agent: a case study on< i> E. coli</i> as a model for Gram-negative bacteria. *J. Colloid Interface Sci.* **2004**, *275*, 177–182.

[13] Panáček, A., Kolář, M., Večeřová, R., Prucek, R., Soukupová, J., Kryštof, V., Hamal, P., Zbořil, R., Kvítek, L. Antifungal activity of silver nanoparticles against Candida spp. *Biomaterials* **2009**, *30*, 6333–6340.

[14] Galdiero, S., Falanga, A., Vitiello, M., Cantisani, M., Marra, V., Galdiero, M. Silver nanoparticles as potential antiviral agents. *Molecules* **2011**, *16*, 8894–8918.

[15] Dubas, S. T., Kumlangdudsana, P., Potiyaraj, P. Layer-by-layer deposition of antimicrobial silver nanoparticles on textile fibers. *Colloids and Surfaces A: Physicochemical and Engineering Aspects* **2006**, *289*, 105–109.

[16] Furno, F., Morley, K. S., Wong, B., Sharp, B. L., Arnold, P. L., Howdle, S. M., Bayston, R., Brown, P. D., Winship, P. D., Reid, H. J. Silver nanoparticles and polymeric medical devices: a new approach to prevention of infection? *Journal of Antimicrobial Chemotherapy* **2004**, *54*, 1019–1024.

[17] He, J.-A., Mosurkal, R., Samuelson, L. A., Li, L., Kumar, J. Dye-sensitized solar cell fabricated by electrostatic layer-by-layer assembly of amphoteric TiO2 nanoparticles. *Langmuir* **2003**, *19*, 2169–2174.

[18] Tan, B., Wu, Y. Dye-sensitized solar cells based on anatase TiO2 nanoparticle/nanowire composites. *The journal of physical chemistry. B* **2006**, *110*, 15932–15938.

[19] Bach, U., Lupo, D., Comte, P., Moser, J. E., Weissörtel, F., Salbeck, J., Spreitzer, H., Grätzel, M. Solid-state dye-sensitized mesoporous TiO2 solar cells with high photon-to-electron conversion efficiencies. *Nature* **1998**, *395*, 583–585.

[20] Park, N.-G., van de Lagemaat, J., Frank, A. J. Comparison of dye-sensitized rutile-and anatase-based TiO2 solar cells. *The Journal of Physical Chemistry B* **2000**, *104*, 8989–8994.

[21] Daniel, M.-C., Astruc, D. Gold nanoparticles: assembly, supramolecular chemistry, quantum-size-related properties, and applications toward biology, catalysis, and nanotechnology. *Chemical reviews* **2004**, *104*, 293–346.

[22] Astruc, D., Lu, F., Aranzaes, J. R. Nanoparticles as recyclable catalysts: the frontier between homogeneous and heterogeneous catalysis. *Angewandte Chemie International Edition* **2005**, *44*, 7852–7872.

[23] Sonström, P., Bäumer, M. Supported colloidal nanoparticles in heterogeneous gas phase catalysis: on the way to tailored catalysts. *Physical chemistry chemical physics PCCP* **2011**, *13*, 19270–19284.

[24] Mädler, L., Kammler, H. K., Mueller, R., Pratsinis, S. E. Controlled synthesis of nanostructured particles by flame spray pyrolysis. *Journal of Aerosol Science* **2002**, *33*, 369–389.

[25] Mädler, L., Stark, W. J., Pratsinis, S. E. Flame-made ceria nanoparticles. *Journal of Materials Research* **2002**, *17*, 1356–1362.

[26] Mueller, R., Mädler, L., Pratsinis, S. E. Nanoparticle synthesis at high production rates by flame spray pyrolysis. *Chemical Engineering Science* **2003**, *58*, 1969–1976.

[27] Bickmore, C. R., Waldner, K. F., Baranwal, R., Hinklin, T., Treadwell, D. R., Laine, R. M. Ultrafine titania by flame spray pyrolysis of a titanatrane complex. *Journal of the European Ceramic Society* **1998**, *18*, 287–297.

[28] Stöber, W., Fink, A., Bohn, E. Controlled growth of monodisperse silica spheres in the micron size range. *Journal of colloid and interface science* **1968**, *26*, 62–69.

[29] Tanaka, S., Nogami, D., Tsuda, N., Miyake, Y. Synthesis of highly-monodisperse spherical titania particles with diameters in the submicron range. *Journal of colloid and interface science* **2009**, *334*, 188–194.

[30] Körmer, R., Schmid, H.-J., Peukert, W. Aerosol synthesis of silicon nanoparticles with narrow size distribution—Part 2: Theoretical analysis of the formation mechanism. *Journal of Aerosol Science* **2010**, *41*, 1008–1019.

[31] Körmer, R., Jank, M., Ryssel, H., Schmid, H.-J., Peukert, W. Aerosol synthesis of silicon nanoparticles with narrow size distribution—Part 1: Experimental investigations. *Journal of Aerosol Science* **2010**, *41*, 998–1007.

[32] Yang, J., Ling, T., Wu, W.-T., Liu, H., Gao, M.-R., Ling, C., Li, L., Du, X.-W. A top–down strategy towards monodisperse colloidal lead sulphide quantum dots. *Nat Commun* **2013**, *4*, 1695.

[33] Wang, Y., Xia, Y. Bottom-up and top-down approaches to the synthesis of monodispersed spherical colloids of low melting-point metals. *Nano Letters* **2004**, *4*, 2047–2050.

[34] Lee, J., Lee, Y., Youn, J. K., Na, H. B., Yu, T., Kim, H., Lee, S., Koo, Y., Kwak, J. H., Park, H. G. Simple Synthesis of Functionalized Superparamagnetic Magnetite/Silica Core/Shell Nanoparticles and their Application as Magnetically Separable High-Performance Biocatalysts. *Small* **2008**, *4*, 143–152.

[35] Burns, A., Ow, H., Wiesner, U. Fluorescent core–shell silica nanoparticles: towards "Lab on a Particle" architectures for nanobiotechnology. *Chemical Society reviews* **2006**, *35*, 1028–1042.

[36] Sun, Y., Xia, Y. Shape-controlled synthesis of gold and silver nanoparticles. *Science (New York, N.Y.)* **2002**, *298*, 2176–2179.

[37] Ahmadi, T. S., Wang, Z. L., Green, T. C., Henglein, A., El-Sayed, M. A. Shape-controlled synthesis of colloidal platinum nanoparticles. *SCIENCE-NEW YORK THEN WASHINGTON-* **1996**, 1924–1925.

[38] Tang, Z., Kotov, N. A., Giersig, M. Spontaneous organization of single CdTe nanoparticles into luminescent nanowires. *Science* **2002**, *297*, 237–240.

[39] Burda, C., Lou, Y., Chen, X., Samia, A. C. S., Stout, J., Gole, J. L. Enhanced nitrogen doping in TiO2 nanoparticles. *Nano Letters* **2003**, *3*, 1049–1051.

[40] Zhuravlev, L. T. The surface chemistry of amorphous silica. Zhuravlev model. *Colloids and Surfaces A: Physicochemical and Engineering Aspects* **2000**, *173*, 1–38.

[41] Tang, C., Zhu, J., Li, Z., Zhu, R., Zhou, Q., Wei, J., He, H., Tao, Q. Surface chemistry and reactivity of SiO2 polymorphs: A comparative study on α-quartz and α-cristobalite. *Applied Surface Science* **2015**, *355*, 1161–1167.

[42] Hoffmann, P., Knözinger, E. Novel aspects of mid and far IR Fourier spectroscopy applied to surface and adsorption studies on SiO2. *Surface Science* **1987**, *188*, 181–198.

[43] Asay, D. B., Kim, S. H. Evolution of the adsorbed water layer structure on silicon oxide at room temperature. *J. Phys. Chem. B* **2005**, *109*, 16760–16763.

[44] Leed, E. A., Pantano, C. G. Computer modeling of water adsorption on silica and silicate glass fracture surfaces. *Journal of Non-Crystalline Solids* **2003**, *325*, 48–60.

[45] Parida, S. K., Dash, S., Patel, S., Mishra, B. K. Adsorption of organic molecules on silica surface. *Advances in Colloid and Interface Science* **2006**, *121*, 77–110.

[46] Sulpizi, M., Gaigeot, M.-P., Sprik, M. The Silica-Water Interface: How the Silanols Determine the Surface Acidity and Modulate the Water Properties. *Journal of Chemical Theory and Computation* **2012**, *8*, 1037–1047.

[47] Diebold, U. The surface science of titanium dioxide. *Surface Science Reports* **2003**, *48*, 53–229.

[48] Kunze, C., Giner, I., Torun, B., Grundmeier, G. Influence of the surface chemistry on TiO 2–TiO 2 nanocontact forces as measured by an UHV–AFM. *Chemical Physics Letters* **2014**, *597*, 134–138.

[49] Amore Bonapasta, A., Filippone, F., Mattioli, G., Alippi, P. Oxygen vacancies and OH species in rutile and anatase TiO2 polymorphs. *Catalysis Today* **2009**, *144*, 177–182.

[50] Minato, T., Sainoo, Y., Kim, Y., Kato, H. S., Aika, K.-i., Kawai, M., Zhao, J., Petek, H., Huang, T., He, W., Wang, B., Wang, Z., Zhao, Y., Yang, J., Hou, J. G. The electronic structure of oxygen atom vacancy and hydroxyl impurity defects on titanium dioxide (110) surface. *The Journal of chemical physics* **2009**, *130*, 124502.

[51] Zhang, Z., Bondarchuk, O., Kay, B. D., White, J. M., Dohnalek, Z. Imaging water dissociation on TiO2(110): Evidence for inequivalent geminate OH groups. *The journal of physical chemistry. B* **2006**, *110*, 21840–21845.

[52] Thiel, P. A., Madey, T. E. The interaction of water with solid surfaces: fundamental aspects. *Surface Science Reports* **1987**, *7*, 211–385.

[53] Henderson, M. The interaction of water with solid surfaces: Fundamental aspects revisited. *Surface Science Reports* **2002**, *46*, 1–308.

[54] Epling, W. S., Peden, C. H., Henderson, M. A., Diebold, U. Evidence for oxygen adatoms on TiO2(110) resulting from O2 dissociation at vacancy sites. *Surface Science* **1998**, *412-413*, 333–343.

[55] Kurtz, R. L., Stock-Bauer, R., Msdey, T. E., Román, E., Segovia, J. de. Synchrotron radiation studies of H2O adsorption on TiO2(110). *Surface Science* **1989**, *218*, 178–200.

[56] Henderson, M. A. Structural Sensitivity in the Dissociation of Water on TiO 2 Single-Crystal Surfaces. *Langmuir* **1996**, *12*, 5093–5098.

[57] Fujishima, A., Honda, K. Photolysis-decomposition of water at the surface of an irradiated semiconductor. *Nature* **1972**, *238*, 37–38.

[58] Diebold, U. Structure and properties of TiO2 surfaces: a brief review. *Applied physics A* **2003**, *76*, 681–687.

[59] Hashimoto, K., Irie, H., Fujishima, A. TiO2 photocatalysis: a historical overview and future prospects. *Japanese journal of applied physics* **2005**, *44*, 8269.

[60] Kumar, S. G., Devi, L. G. Review on modified TiO2 photocatalysis under UV/visible light: selected results and related mechanisms on interfacial charge carrier transfer dynamics. *The journal of physical chemistry. A* **2011**, *115*, 13211–13241.

[61] Linsebigler, A. L., Lu, G., Yates Jr, J. T. Photocatalysis on TiO2 surfaces: principles, mechanisms, and selected results. *Chemical reviews* **1995**, *95*, 735–758.

[62] Luttrell, T., Halpegamage, S., Tao, J., Kramer, A., Sutter, E., Batzill, M. Why is anatase a better photocatalyst than rutile?--Model studies on epitaxial TiO2 films. *Scientific reports* **2014**, *4*, 4043.

[63] Ni, M., Leung, M. K. H., Leung, D. Y. C., Sumathy, K. A review and recent developments in photocatalytic water-splitting using TiO2 for hydrogen production. *Renewable and Sustainable Energy Reviews* **2007**, *11*, 401–425.

[64] Scanlon, D. O., Dunnill, C. W., Buckeridge, J., Shevlin, S. A., Logsdail, A. J., Woodley, S. M., Catlow, C. R. A., Powell, M. J., Palgrave, R. G., Parkin, I. P., Watson, G. W., Keal, T. W., Sherwood, P., Walsh, A., Sokol, A. A. Band alignment of rutile and anatase $TiO_2$. *Nature materials* **2013**, *12*, 798–801.

[65] Miyauchi, M., Nakajima, A., Fujishima, A., Hashimoto, K., Watanabe, T. Photoinduced Surface Reactions on TiO 2 and SrTiO 3 Films: Photocatalytic Oxidation and Photoinduced Hydrophilicity. *Chem. Mater.* **2000**, *12*, 3–5.

[66] Wang, R., Hashimoto, K., Fujishima, A., Chikuni, M., Kojima, E., Kitamura, A., Shimohigoshi, M., Watanabe, T. Light-induced amphiphilic surfaces. *Nature* **1997**, *388*, 431–432.

[67] Wang, R., Sakai, N., Fujishima, A., Watanabe, T., Hashimoto, K. Studies of Surface Wettability Conversion on TiO 2 Single-Crystal Surfaces. *J. Phys. Chem. B* **1999**, *103*, 2188–2194.

[68] Wang, R., Hashimoto, K., Fujishima, A., Chikuni, M., Kojima, E., Kitamura, A., Shimohigoshi, M., Watanabe, T. Photogeneration of highly amphiphilic TiO 2 surfaces. *Advanced Materials* **1998**, *10*, 135–138.

[69] Kunze, C., Torun, B., Giner, I., Grundmeier, G. Surface chemistry and nonadecanoic acid adsorbate layers on TiO 2 (100) surfaces prepared at ambient conditions. *Surface Science* **2012**, *606*, 1527–1533.

[70] Israelachvili J. N. *Intermolecular and surface forces: revised third edition*; Academic press, 2011.

[71] Butt, H.-J., Makowski, M., Kappl, M., Ptak, A. On the Adhesion Between Individual Particles. *Kona* **2011**, *29*, 2011.

[72] Farshchi-Tabrizi, M., Kappl, M., Cheng, Y., Gutmann, J., Butt, H.-J. On the Adhesion between Fine Particles and Nanocontacts: An Atomic Force Microscope Study. *Langmuir* **2006**, *22*, 2171–2184.

[73] Butt H.-J., Graf K., Kappl M. *Physics and chemistry of interfaces*; John Wiley & Sons, 2006.

[74] Médout-Marère, V. A simple experimental way of measuring the Hamaker constant A 11 of divided solids by immersion calorimetry in apolar liquids. *Journal of colloid and interface science* **2000**, *228*, 434–437.

[75] Bergström, L. Hamaker constants of inorganic materials. *Advances in Colloid and Interface Science* **1997**, *70*, 125–169.

[76] Young, T. An essay on the cohesion of fluids. *Philosophical Transactions of the Royal Society of London* **1805**, 65–87.

[77] Laplace P. S. *Traité de mécanique céleste*; Courcier, 1805.

[78] Thomson, W. 4. On the Equilibrium of Vapour at a Curved Surface of Liquid. *Proceedings of the Royal Society of Edinburgh* **1872**, *7*, 63–68.

[79] Butt H.-J., Kappl M. *Surface and interfacial forces*; John Wiley & Sons, 2009.

[80] Dörmann, M., Schmid, H.-J. Simulation of capillary bridges between nanoscale particles. *Langmuir the ACS journal of surfaces and colloids* **2014**, *30*, 1055–1062.

[81] McMullan, D. Scanning electron microscopy 1928-1965. *Scanning* **1995**, *17*, 175–185.

[82] Ward, B. W., Notte, J. A., Economou, N. P. Helium ion microscope: A new tool for nanoscale microscopy and metrology. *J. Vac. Sci. Technol. B* **2006**, *24*, 2871.

[83] Alov, N. V. Fifty years of x-ray photoelectron spectroscopy. *Journal of Analytical Chemistry* **2005**, *60*, 297–300.

[84] Hertz, H. Ueber einen Einfluss des ultravioletten Lichtes auf die electrische Entladung. *Annalen der Physik* **1887**, *267*, 983–1000.

[85] Einstein, A. Über einem die Erzeugung und Verwandlung des Lichtes betreffenden heuristischen Gesichtspunkt. *Annalen der Physik* **1905**, *4*.

[86] Wapner, K., Stratmann, M., Grundmeier, G. In situ infrared spectroscopic and scanning Kelvin probe measurements of water and ion transport at polymer/metal interfaces. *Electrochim. Acta* **2006**, *51*, 3303–3315.

[87] Raacke, J., Giza, M., Grundmeier, G. Combination of FTIR reflection absorption spectroscopy and work function measurement for in-situ studies of plasma modification of polymer and metal surfaces. *Surface and Coatings Technology* **2005**, *200*, 280–283.

[88] Giner, I., Maxisch, M., Kunze, C., Grundmeier, G. Combined in situ PM-IRRAS/QCM studies of water adsorption on plasma modified aluminum oxide/aluminum substrates. *Appl. Surf. Sci.* **2013**, *283*, 145–153.

[89] Vlasak, R., Klueppel, I., Grundmeier, G. Combined EIS and FTIR-ATR study of water uptake and diffusion in polymer films on semiconducting electrodes. *Electrochim. Acta* **2007**, *52*, 8075–8080.

[90] Liu, C. N., Ozkaya, B., Steves, S., Awakowicz, P., Grundmeier, G. Combined in situ FTIR-spectroscopic and electrochemical analysis of nanopores in ultra-thin SiOx-like plasma polymer barrier films. *J. Phys. D-Appl. Phys.* **2013**, *46*.

[91] Chumaevskii, N. A., Rodnikova, M. N. Some peculiarities of liquid water structure. *J. Mol. Liq.* **2003**, *106*, 167–177.

[92] Du, Q., Freysz, E., Shen, Y. R. SURFACE VIBRATIONAL SPECTROSCOPIC STUDIES OF HYDROGEN-BONDING AND HYDROPHOBICITY. *Science* **1994**, *264*, 826–828.

[93] Sauerbrey G. Z. *Use of quartz crystal vibrator for weighting thin films on a microbalance. Physics 155, 206–222 (1959); Bottom, VE, Introduction to Quartz Crystal Unit Design*; Van Nostrand Reinhold Co, New York, 1982.

[94] Curie, J., Curie, P. Piezoelectric and allied phenomena in Rochelle salt. *Comput Rend Acad Sci Paris* **1880**, *91*, 294–297.

[95] Du, B. Y., König, A. M., Johannsmann, D. On the role of capillary instabilities in the sandcastle effect. *New J. Phys.* **2008**, *10*.

[96] D'Amour, J. N., Stalgren, J. J. R., Kanazawa, K. K., Frank, C. W., Rodahl, M., Johannsmann, D. Capillary aging of the contacts between glass spheres and a quartz resonator surface. *Phys. Rev. Lett.* **2006**, *96*.

[97] Dybwad, G. L. A sensitive new method for the determination of adhesive bonding between a particle and a substrate. *Journal of applied physics* **1985**, *58*, 2789.

[98] Pomorska, A., Yliniemi, K., Wilson, B. P., Shchukin, D., Johannsmann, D., Grundmeier, G. QCM study of the adsorption of polyelectrolyte covered mesoporous TiO2 nanocontainers on SAM modified Au surfaces. *J. Colloid Interface Sci.* **2011**, *362*, 180–187.

[99] Pomorska, A., Shchukin, D., Hammond, R., Cooper, M. A., Grundmeier, G., Johannsmann, D. Positive Frequency Shifts Observed Upon Adsorbing Micron-Sized Solid Objects to a Quartz Crystal Microbalance from the Liquid Phase. *Anal. Chem.* **2010**, *82*, 2237–2242.

[100] Binnig, G., Rohrer, H., Gerber, C., Weibel, E. Surface studies by scanning tunneling microscopy. *Physical review letters* **1982**, *49*, 57.

[101] Giessibl, F. J., Hembacher, S., Bielefeldt, H., Mannhart, J. Subatomic features on the silicon (111)-(7× 7) surface observed by atomic force microscopy. *Science* **2000**, *289*, 422–425.

[102] Binnig, G., Quate, C. F., Gerber, C. Atomic force microscope. *Physical review letters* **1986**, *56*, 930.

[103] Boray Torun. *Masterthesis: In situ AFM studies of organophosphonic acid monolayer formation and stability on $Al_2O_3$(0001) surfaces*, 2010.

[104] Torun, B., Ozkaya, B., Grundmeier, G. Atomic Force Microscopy (AFM)-based nanografting for the study of self-assembled monolayer formation of organophosphonic acids on Al2O3 single-crystal surfaces. *Langmuir* **2012**, *28*, 6919–6927.

[105] Lammel, P., Torun, B., Kleber, C., Grundmeier, G. In-situ AFM study of the electrodeposition of copper on plasma modified carbon fibre-reinforced polymer surfaces. *Surface and Coatings Technology* **2013**, *221*, 22–28.

[106] Ozkaya, B., Ozcan, O., Thissen, P., Grundmeier, G. Single Molecule Desorption Studies on Immobilized Nanoclay Particle Surfaces. *Langmuir* **2010**, *26*, 8155–8160.

[107] Salameh, S., Scholz, R., Seo, J. W., Mädler, L. Contact behavior of size fractionated TiO 2 nanoparticle agglomerates and aggregates. *Powder Technology* **2014**, *256*, 345–351.

[108] Aprile, C., Maretti, L., Alvaro, M., Scaiano, J. C., Garcia, H. Long-lived (minutes) photoinduced charge separation in a structured periodic mesoporous titania containing 2,4,6-triphenylpyrylium as guest. *Dalton transactions (Cambridge, England 2003)* **2008**, 5465–5470.

[109] McNamee, C. E., Yamamoto, S., Butt, H.-J., Higashitani, K. A straightforward way to form close-packed TiO2 particle monolayers at an air/water interface. *Langmuir* **2010**, *27*, 887–894.

[110] Grundmeier, G., Stratmann, M. Plasma polymerization–a new and promising way for the corrosion protection of steel. *Materials and Corrosion* **1998**, *49*, 150–160.

[111] Gebhard, M., Mitschker, F., Wiesing, M., Giner, I., Torun, B., los Arcos, T. de, Awakowicz, P., Grundmeier, G., Devi, A. An efficient PE-ALD process for $TiO_2$ thin films employing a new Ti-precursor. *J. Mater. Chem. C* **2016**, *4*, 1057–1065.

[112] Torun, B., Kunze, C., Zhang, C., Kühne, T. D., Grundmeier, G. Study of water adsorption and capillary bridge formation for $SiO_2$ nanoparticle layers by means of a combined in situ FT-IR reflection spectroscopy and QCM-D set-up. *Physical chemistry chemical physics PCCP* **2014**, *16*, 7377–7384.

[113] Johannsmann, D. Piezoelectric Stiffening. In *The Quartz Crystal Microbalance in Soft Matter Research*; Springer International Publishing, 2015, pp. 125–142.

[114] Creatore, M., Palumbo, F., d'Agostino, R., Fayet, P. RF plasma deposition of SiO2-like films: plasma phase diagnostics and gas barrier film properties optimisation. *Surf. Coat. Technol.* **2001**, *142*, 163–168.

[115] Kobayashi, M., Skarba, M., Galletto, P., Cakara, D., Borkovec, M. Effects of heat treatment on the aggregation and charging of Stöber-type silica. *J. Colloid Interface Sci.* **2005**, *292*, 139–147.

[116] Bogush, G. H., Tracy, M. A., Zukoski Iv, C. F. Preparation of monodisperse silica particles: Control of size and mass fraction. *Journal of Non-Crystalline Solids* **1988**, *104*, 95–106.

[117] Asay, D. B., Boer, M. P. de, Kim, S. H. Equilibrium Vapor Adsorption and Capillary Force: Exact Laplace–Young Equation Solution and Circular Approximation Approaches. *Journal of Adhesion Science and Technology* **2010**, *24*, 2363–2382.

[118] Sulpizi, M., Gaigeot, M.-P., Sprik, M. The Silica–Water Interface: How the Silanols Determine the Surface Acidity and Modulate the Water Properties. *Journal of Chemical Theory and Computation* **2012**, *8*, 1037–1047.

[119] Kühne, T. D., Krack, M., Parrinello, M. Static and Dynamical Properties of Liquid Water from First Principles by a Novel Car–Parrinello-like Approach. *Journal of Chemical Theory and Computation* **2009**, *5*, 235–241.

[120] Kühne, T. D., Pascal, T. A., Kaxiras, E., Jung, Y. New Insights into the Structure of the Vapor/Water Interface from Large-Scale First-Principles Simulations. *The Journal of Physical Chemistry Letters* **2010**, *2*, 105–113.

[121] Fan, Y., Chen, X., Yang, L., Cremer, P. S., Gao, Y. Q. On the Structure of Water at the Aqueous/Air Interface. *The Journal of Physical Chemistry B* **2009**, *113*, 11672–11679.

[122] Zhang, C., Khaliullin, R. Z., Bovi, D., Guidoni, L., Kühne, T. D. Vibrational Signature of Water Molecules in Asymmetric Hydrogen Bonding Environments. *The Journal of Physical Chemistry Letters* **2013**, *4*, 3245–3250.

[123] Ratcliffe, C. I., Irish, D. E. Vibrational spectral studies of solutions at elevated temperatures and pressures. 5. Raman studies of liquid water up to 300. degree. C. *The Journal of Physical Chemistry* **1982**, *86*, 4897–4905.

[124] Kühne, T. D., Khaliullin, R. Z. Electronic signature of the instantaneous asymmetry in the first coordination shell of liquid water. *Nature communications* **2013**, *4*, 1450.

[125] Khaliullin, R. Z., Kühne, T. D. Microscopic properties of liquid water from combined ab initio molecular dynamics and energy decomposition studies. *Physical Chemistry Chemical Physics* **2013**, *15*, 15746–15766.

[126] Naik, V. V., Crobu, M., Venkataraman, N. V., Spencer, N. D. Multiple Transmission-Reflection IR Spectroscopy Shows that Surface Hydroxyls Play Only a Minor Role in Alkylsilane Monolayer Formation on Silica. *The Journal of Physical Chemistry Letters* **2013**, *4*, 2745–2751.

[127] Maxisch, M., Thissen, P., Giza, M., Grundmeier, G. Interface chemistry and molecular interactions of phosphonic acid self-assembled monolayers on oxyhydroxide-covered aluminum in humid environments. *Langmuir* **2011**, *27*, 6042–6048.

[128] Huttl, G., Klemm, V., Popp, R., Simon, F., Muller, E. Tailored colloidal AFM probes and their TEM investigation. *Surface and interface analysis* **2002**, *33*, 50–53.

[129] Ata, A., Rabinovich, Y. I., Singh, R. K. Role of surface roughness in capillary adhesion. *Journal of Adhesion Science and Technology* **2002**, *16*, 337–346.

[130] Bérard, V., Lesniewska, E., Andrès, C., Pertuy, D., Laroche, C., Pourcelot, Y. Dry powder inhaler: Influence of humidity on topology and adhesion studied by AFM. *International Journal of Pharmaceutics* **2002**, *232*, 213–224.

[131] Fuji, M., Machida, K., Takei, T., Watanabe, T., Chikazawa, M. Effect of Wettability on Adhesion Force between Silica Particles Evaluated by Atomic Force Microscopy Measurement as a Function of Relative Humidity. *Langmuir* **1999**, *15*, 4584–4589.

[132] Jones, R., Pollock, H., Geldart, D., Verlinden, A. Inter-particle forces in cohesive powders studied by AFM: Effects of relative humidity, particle size and wall adhesion. *Powder Technology* **2003**, *132*, 196–210.

[133] Jones, R., Pollock, H. M., Cleaver, J. A. S., Hodges, C. S. Adhesion Forces between Glass and Silicon Surfaces in Air Studied by AFM: Effects of Relative Humidity, Particle Size, Roughness, and Surface Treatment. *Langmuir* **2002**, *18*, 8045–8055.

[134] Thundat, T., Zheng, X.-Y., Chen, G. Y., Warmack, R. J. Role of relative humidity in atomic force microscopy imaging. *Surface Science* **1993**, *294*, L939-L943.

[135] Xiao, X., Qian, L. Investigation of humidity-dependent capillary force. *Langmuir* **2000**, *16*, 8153–8158.

[136] Thissen, P., Valtiner, M., Grundmeier, G. Stability of phosphonic acid self-assembled monolayers on amorphous and single-crystalline aluminum oxide surfaces in aqueous solution. *Langmuir* **2009**, *26*, 156–164.

## 8.8. List of publications

1. Study of water adsorption and capillary bridge formation for $SiO_2$ nanoparticle layers by means of a combined in situ FT-IR reflection spectroscopy and QCM-D set-up.
   **B. Torun**, C. Kunze, C. Zhang, T. D. Kühne, G. Grundmeier, *PCCP*, **2014**, *16*, 7377-7384

2. Atomic Force Microscopy (AFM)-based nanografting for the study of self-assembled monolayer formation of organophosphonic acids on $Al_2O_3$ single-crystal surfaces.
   **B. Torun**, B. Özkaya, G. Grundmeier, *Langmuir*, **2012**, *28*, 6919-6927

3. In-situ PM-IRRAS investigations of stability of organofunctional thin film – ZnO interfaces at high water activities.
   **B. Torun**, I. Giner, G. Grundmeier, Ö. Özcan, *Suf. Interface Anal.*, **2016**, (currently under review)

4. Adsorption and Adhesion Studies of PdSn-Nanoparticles on Protonated Amine- and Carboxylic Acid Terminated Surfaces.
   B. Mosebach, F. M. Bayer, C-C Fels, M. Voigt, B. Özkaya, A. Pomorska, **B. Torun**, A. Keller, G. Grundmeier, *Surf. Interface Anal.*, **2016**, DOI: 10.1002/sia.6016

5. An efficient PE-ALD process for $TiO_2$ thin films employing a new Ti-precursor.
   M. Gebhard, F. Mitschker, M. Wiesing, I. Giner, **B. Torun**, T. del los Arcos, P. Awakowicz, G. Grundmeier, A. Devi, *J. Mater. Chem. C*, **2016**, *4*, 1057-1065

6. Influence of the surface chemistry on $TiO_2$-$TiO_2$ nanocontact forces as measured by an UHV-AFM.
   C. Kunze, I. Giner, **B. Torun**, G. Grundmeier, *Chem. Phys. Letters*, **2014**, *597*, 134-138

7. In-situ AFM study of the electrodeposition of copper on plasma modified carbon fiber-reinforced polymer surfaces.
   P. Lammel, **B. Torun**, C. Kleber, G. Grundmeier, *Surface and Coatings Technology,* **2013**, *221*, 22–28.

8. Surface chemistry and nonadecanoic acid adsorbate layers on $TiO_2$ (100) surfaces prepared at ambient conditions.
   C. Kunze, **B. Torun**, I. Giner, G. Grundmeier, *Surface Science*, **2012**, *606*, 1527-1533

9. PM-IRRAS studies of the adsorption and stability of organophosphonate monolayers on passivated NiTi surfaces.
   M. Maxisch, C. Ebbert, **B. Torun**, G. Grundmeier, *Applied Surface Science*, **2011**, *257,* 2011–2018

## 8.9. Selected conference contributions

| | |
|---|---|
| 2015, Granada, Spain | 16th European Conference on Application of Surface and Interface Analysis (talk) |
| 2014, Baltimore, USA | 61th American Vacuum Society International Symposium (talk) |
| 2014, Hamburg, Germany | 113. Bunsentagung (poster) |
| 2013, Cagliari, Sardinia | 15th European Conference on Application of Surface and Interface Analysis (talk) |
| 2012, Tampa, USA | 59th American Vacuum Society International Symposium (talk) |
| 2012, Friedrichshafen, Germany | 9th European Adhesion Conference (poster) |
| 2012, Friedrichshafen, Germany | 7th International Conference for Conveying and Handling of Particulate Solids (talk) |
| 2011, Berlin, Germany | 110. Bunsentagung (poster) |